CONTROL STRATEGIES FOR PIEZOELECTRICALLY ACTUATED FAST MECHANICAL DISCONNECT SWITCHES FOR HYBRID CIRCUIT BREAKERS

A Dissertation
Presented to
The Academic Faculty

By

Chunmeng Xu

In Partial Fulfillment
of the Requirements for the Degree
Doctor of Philosophy in the
School of Electrical and Computer Engineering

Georgia Institute of Technology

August 2021

CONTROL STRATEGIES FOR PIEZOELECTRICALLY ACTUATED FAST MECHANICAL DISCONNECT SWITCHES FOR HYBRID CIRCUIT BREAKERS

Approved by:

Dr. Lukas Graber, Advisor
School of Electrical and Computer Engineering
Georgia Institute of Technology

Dr. Maryam Saeedifard
School of Electrical and Computer Engineering
Georgia Institute of Technology

Dr. Santiago Carlos Grijalva
School of Electrical and Computer Engineering
Georgia Institute of Technology

Dr. Deepakraj M Divan
School of Electrical and Computer Engineering
Georgia Institute of Technology

Dr. Michael "Mischa" Steurer
Center for Advanced Power Systems
Florida State University

Date Approved: May 5, 2021

To my parents, Baoshan Xu & Wanjun Hu,

for all their support and love.

ACKNOWLEDGMENTS

There are uncountable times in the past five years that I felt like I have met the best advisor to my knowledge, Prof. Lukas Graber. I have learned the best way of research from him - studying things that make me curious. Prof. Graber has an impressive passion for getting more knowledge on new topics and trying new things to see how it works. From cryogenic switchgear to thermosyphon bushing, I have been so lucky to be along with him on the journey of explorations throughout these years. Meanwhile, he is also a kind and supportive supervisor, as he has supported all the significant decisions of my Ph.D. study ranging from the research topic selections to the outreach experience recommendations. I will keep practicing the things I learned in his lab, and hopefully, I could become an accomplished researcher like him in my future.

I would like to give my sincere thanks to Dr. Maryam Saeedifard, Dr. Santiago Grijalva, Dr. Deepak Divan, and Dr. Michael "Mischa" Steurer for serving on my dissertation committee. I'm very fortunate to participate in multiple collaboration projects and co-author numerous publications with my committee members. Their precious suggestions on the research and valuable comments on the thesis have brought me new perspectives on the interdisciplinary research we have collaborated on.

I would also like to faithfully thank my collaborators in the Center for Advanced Power Systems and Florida State University: Matt Bosworth, Dr. Yanjun Shi, Dr. Qichen Yang, Dr. Lu Wang, Yuchen He, Rachit Argawal and others. Although our physical locations are separated by hundreds of miles, the online meetings during the pandemic have made me feel like we are truly colleagues sitting close in the same office and working together in the same lab space.

It was delightful to work with many exceptional colleagues in the Plasma and Dielectrics Laboratory. I would like to thank Dr. Chanyeop Park and Dr. Tushar Damle for their guidance and collaborations as senior Ph.D. students. I'm very grateful for the

friendship of Jia Wei as peers throughout the years of my Ph.D. study. Also, I want to send my gratitude to Alfonso Cruz, Jeong Ho Choi, Ning Guo, Amanda West, Dr. Zhiyang Jin and Dr. Maryam Tousi for the help and support of working together. It has been a happy time spent in Georgia Tech with my power group fellows and friends, and I want to thank Dr. Chen Jiang, Dr. Sufei Li, Dr. Shen Zhang, Dr. Cheng Gong, Dr. Boqi Xie, Dr. Jiahao Xie, Dr. Yuan Kong, Dr. Chiyang Zhong. Dr. Xiangyu Han, Dr. Jingfan Sun, Kaiyu Liu, Mengxue Hou, Gengyi Luo, Shiyuan Jin, Justin Zhang, Qianxue Xia, Zheng An, Xiwei Zheng, Decheng Yan Morteza Rezaee, Abdulaziz M. Qwbaiban, Mohammad Miranbeigi, and Liran Zheng for their support and friendship.

Most of all, I owe my gratitude to my parents for their tremendous love and support for my Ph.D. study. Although I haven't met them face-to-face for two years due to the pandemic, their love and encouragement have always been with me throughout the past five years of study. Therefore, I dedicate this dissertation to my parents, Baoshan Xu and Wanjun Hu, for their endless love and support.

TABLE OF CONTENTS

LIST OF TABLES

LIST OF FIGURES

SUMMARY

Piezoelectrically-actuated fast mechanical switches provide a low-loss conduction path in hybrid circuit breakers for medium-voltage, direct-current system protection. With the desired actuation performance being pushed towards the driving limit of the piezoelectric actuator, excessive vibration starts to dominate the underdamped travel curves of contact movements, which will lead to insulation failures and delayed operations in the fast mechanical switch. To improve underdamped responses into critically damped actuations, several switching motion control strategies have been proposed with active damping filters such as notch, lead and lag compensators in the closed-loop system. The switching motion controllers are built upon a vibrational dynamics model of a prestressed piezoelectric stack actuator with experimentally identified parameters. The controller tuning principles are derived to achieve optimized step responses with a minimized rising time down to 250 μs, a reduced undershoot around 10%, and a closed-loop control bandwidth up to 1760 Hz. The closed-loop simulation is performed to verify the performance of proposed switching motion controllers on both low-frequency external disturbance elimination and high-frequency internal vibration attenuation. According to the hardware implementation tests, the proposed control strategies have optimized the switching motions of a heavily loaded piezoelectric actuator with 60% reduction in undershoot and 45% reduction in settling time. At the same time, the sub-millisecond switching time has been preserved in the actively damped travel curves of this piezoelectric actuator. With optimized switching operations of the piezoelectric actuator, the overall fast mechanical switch can better serve the advanced hybrid circuit breakers to achieve reduced fault current and fault clearance time during circuit interruptions. Consequently, the overall medium-voltage direct-current systems can get better protected by the piezoelectrically-actuated fast mechanical switch.

CHAPTER 1
INTRODUCTION

1.1 Problem Statement

Hybrid circuit breakers (HCBs) have become a promising candidate for protecting high-voltage and medium-voltage direct-current power systems [1]. Introduced as a critical component to reduce the on-state conduction losses of HCBs, the fast mechanical switches (FMS, also known as ultrafast disconnector or UFD) limit the switching speed of HCBs [2]. To achieve faster switching operations, a new type of piezoelectrically-actuated fast mechanical switches (PA-FMS) has been proposed and tested in previous studies [3]. However, the existing control method of the PA-FMS prototype has not fully explored the capability of its internal piezoelectric actuator (PA), considering the PA-FMS travel curves are currently affected with excessive vibrations that have prolonged the PA-FMS switching time to exceed one millisecond.

The demand for vibration-damped FMS travel curves emerges after the HCBs start to adopt a new control strategy named sequential tripping [4], progressive switching [5], or surge arrester insertions while FMS contacts are moving [6]. This new HCB control can reduce the peak fault current and energy dissipation during circuit interruptions, but its prerequisite is a predefined, linearly-changing FMS travel curve without subsequent vibrations [4]. Otherwise, a vibrating travel curve may lead to an insulation failure in FMS by shortening the gap distance between contacts under high isolation voltage [3]. Unfortunately, the commonly-used Thomson coil actuators cannot provide such linear and vibration-free travel curves in their FMS according to existing publications [7]. Therefore, it will be the major advantage of PA-FMS over Thomson coil-actuated FMS to provide the desired critically-damped travel curves for accommodating advanced HCBs.

To minimize switching time and avoid potential insulation failures of a PA-FMS, this dissertation proposes several switching motion control strategies for a multilayer stack PA working in a supercritical-fluids-insulated (SCF-insulated) PA-FMS to achieve critically-damped travel curves. Different from the control targets in this research, existing studies on PAs have focused on improving one specific feature like fast response [8] and large displacement [9], or combining two control targets in their actuations like high speed with large displacement [10], or high speed with heavy load [11], or heavy load with large displacement [12]. However, there has not been a comprehensive study focusing on three control goals simultaneously in a prestressed stack PA of switchgear application. The three goals include a high control bandwidth approaching 2 kHz, a large displacement over 10 μm, and a heavy load over 5 times of the actuator's self-weight.

Different from trajectory-tracking applications that are affected with hysteresis nonlinearity in PAs [13], the dominant challenge of actuations with a heavy payload in switching-motion applications is the vibration nonlinearity, which will lead to poor positioning accuracy [14], low moving efficiency [12], slow positioning speed [11] and elongated settling time [15]. Similarly, an underdamped travel curve in PA-FMS will significantly delay the switching operations of overall HCB, which is the major difficulty in this study.

Achieving critically-damped travel curves in PA-FMS needs a systematic tuning approach to balance the rising time, settling time, and overshoot/undershoot in step responses of digital controllers. Unfortunately, existing studies on PA vibration problems fail to include such detailed tuning guidance for achieving optimal vibration-damped performance. And their step responses were either overdamped with several milliseconds of rising time or still underdamped with significant overshoot [14, 16]. Therefore, the systematic tuning procedures for achieving critical damping in PA travel curves will be generalized as a part of the proposed switching motion controllers in this study. The vibration attenuation performance of tuned controllers will be verified by both closed-loop simulations and hardware implementation tests. As the new damping filter candidates like lead and lag filters

are proposed in this study, the benefits of using a lag filter over a notch filter in parameter mismatched actuations are also discovered and confirmed by both simulations and tests.

1.2 Research Objectives

The objective of the proposed research is to develop the switching motion control strategies for piezoelectrically-actuated fast mechanical switches to generate fast and steady contact movements to satisfy the requirements of hybrid circuit breakers. The objectives of this research are listed below.

1. Identify the characteristics of contact travel curves in piezoelectrically-actuated fast mechanical switches;
2. Summarize the objectives of switching motion control in piezoelectric actuators to accommodate the operational requirements of the fast mechanical switch and the hybrid circuit breaker;
3. Derive the comprehensive dynamic model of the piezoelectric actuator under the switching motion control;
4. Construct switching motion controllers and active damping filters with systematic tuning principles to achieve critically-damped responses;
5. Validate the proposed control strategies through closed-loop simulation and hardware implementation tests;
6. Explore the improvements in the driving hardware to accelerate the piezoelectric actuation further.

1.3 Outline of Chapters

Chapter 2 reviews the background and existing studies on hybrid circuit breakers, fast mechanical switches, and piezoelectric actuators. The modeling and control for piezoelectric

actuators in literature are also reviewed focusing on the comprehensive dynamic model of piezoelectric actuators.

Chapter 3 evaluates the open-loop travel curves of a parallel prestressed actuator carrying a heavy payload to reach a long travel distance under ultrafast actuations in a PA-FMS. Vibration in open-loop travel curves is modeled after their origins are identified. A vibrational dynamic model describing the piezoelectric actuator system is established.

Chapter 4 constructs the switching motion controllers with vibration-damping filters based on the vibrational dynamic model of the piezoelectric actuator. A general review of different vibration damping methods in piezoelectric actuations is first given. The tuning guidance for closed-loop controllers with notch filter or lead/lag filters is derived with analyses on bode plots, pole-zero maps, and step responses. Finally, the parameter sensitivity simulations of tuned controllers are performed to compare different filters used in proposed switching motion controllers.

Chapter 5 performs the closed-loop simulation with embedded codes of switching motion controllers and electrical equivalent circuits of the piezoelectric actuator. The hardware coding and event flow in the firmware-coded controller are also described in detail.

Chapter 6 focuses on the experimental verification of switching motion controllers with a closed-loop hardware system. After configuring the microcontroller settings and signal processing peripherals, comprehensive tests on low-frequency and high-frequency vibration attenuation performance are conducted with different strategies and different driving conditions.

Chapter 7 presents three promising ideas that worth further investigation in the future PA-FMS control study: accelerated switching branch, input shaping method, and self-sensing technique. Proof-of-concept simulations or preliminary test results are included for references.

Chapter 8 summarizes the intellectual contributions in this thesis.

CHAPTER 2
BACKGROUND AND LITERATURE REVIEW

This chapter reviews the current research progress on hybrid circuit breakers (HCBs) and fast mechanical switches (FMS). Two major types of FMS, the Thomson coil-actuated FMS and the piezoelectrically-actuated FMS (PA-FMS) are compared on their controllability. The fundamental working principle, modeling, and control of piezoelectric actuators are also surveyed in detail.

2.1 Hybrid Circuit Breakers

Direct-current (DC) power systems are widely accepted for high-voltage bulk power transmissions and low-voltage commercial or industrial applications, while the markets for medium-voltage direct-current (MVDC, usually 1 kV – 100 kV) systems are still in their early phases of development [17, 3]. Current implementations of MVDC systems are mainly for electrified transportation, such as railways and ships. With higher penetration of distributed energy resources (DERs), more MVDC microgrids will be built for DER integration, energy storage, and electric vehicle charging stations. Other applications of MVDC systems also include data centers, industrial facilities, and high energy physics installations [17, 18].

Given the wide spectrum of potential MVDC system applications, the absence of reliable MVDC switchgear technology is considered as a bottleneck that hinders the rapid growth of MVDC markets [17, 19]. Different from alternating-current (AC) CBs, which utilize natural zero-crossings in current waveforms to break the circuit, DCCBs need to create artificial zero-crossings by commutating the current from the normal conduction path to the energy absorption path where a great number of surge arresters are installed (Figure 2.1) [20, 3]. These current commutation processes demonstrate the technical challenges

of DCCBs, and their critical parameters including the interruption speed will influence not only the ratings of DCCBs but also the designs and structures of the overall MVDC system [17].

Because the current commutation operations are mainly performed by power electronic devices, some of the DCCBs are built purely with solid-state devices, and this version of DCCBs is known as solid-state CBs (SSCBs) [21, 22]. SSCBs are arcless switchgear with particularly short switching time t_{sw} ranging from milliseconds to nanoseconds [21]. The switching time t_{sw} is a critical parameter that determines how much fault current to be interrupted and how much fault energy to be dissipated by the DCCB [2]. For example, assuming a bolted fault happens in a well-regulated MVDC system with a negligible voltage drop at the fault location, the system voltage is V_{DC} and the system inductance is L_s. Then an estimate on the peak fault current with a linear rate of rise and the maximum fault energy to be dissipated from system inductance are:

$$I_{peak} = \frac{\partial I_F}{\partial t} t_{sw} + I_0 = \frac{V_{DC}}{L_s} t_{sw} + I_0 \tag{2.1}$$

$$E_{fault} = \frac{1}{2} L_s I_{peak}^2 \tag{2.2}$$

In a DC system with a 12 kV source V_{DC} and an equivalent source inductance L_s of 300 μH, the rate of rise of fault current could reach as high as 40 A/μs. Neglecting the nominal system current ($I_0 = 0$), a current interruption achieved after 100 μs ($t_{sw} = 100\mu s$) will expect a fault current peak I_{peak} of 4 kA and a maximum fault energy E_{fault} of 2.4 kJ. Comparatively, a delayed interruption at 1 ms has to manage 40 kA of I_{peak} and 240 kJ of E_{fault}. Therefore, if the interruption time gets elongated from 0.1 ms to 1 ms, the overall MVDC system has to deal with 10 times of peak fault current. The DCCB itself needs 100 times of energy dissipation capability in its energy absorption branch with metal-oxide varistors (MOVs). MOVs are nonlinear resistive components that are commonly used for

surge protections [23]. Consequently, the switching time t_{sw} of DCCBs in MVDC systems is preferably to be as small as possible to minimize fault current and energy dissipation. The SSCBs are thus naturally suitable for interrupting MVDC circuits with their superior switching speed.

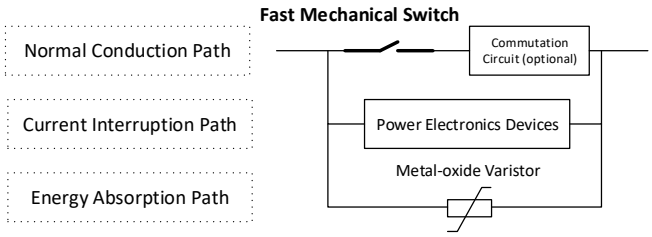

Figure 2.1: A typical configuration of hybrid circuit breakers (HCBs) [2].

However, SSCBs have considerately significant on-state conduction losses in their power electronic devices that limit the DCCB efficiency and cause thermal problems [21]. A practical approach to minimize the on-state loss of DCCB is introducing a mechanical switch into the normal conduction path of DCCB that bypasses power electronic devices, and the overall DCCB now becomes an HCB (Figure 2.1). A further boost in HCB efficiency can be achieved by moving the commutation circuit (also constructed with semiconductor devices) from the normal conduction path to the current interruption path [24]. Different from semiconductor devices with mΩ-level conduction resistances [21], mechanical switches have metal contacts that can efficiently conduct current with $\mu\Omega$ level of on-state resistance [3]. In this way, the Ohmic losses of a mechanical switch are significantly lower than a semiconductor switch with a similar current rating.

The mechanical switch in an HCB's normal conduction path could bring advantages like reduced on-state losses, but it also brings disadvantages like extended switching time. The switching time of an SSCB is usually smaller than 0.1 ms and sometimes down to several nanoseconds [21], considering the electron flows within semiconductors have virtually no mechanical inertia. Comparatively, the switching time of a typical HCB is well above 0.1 ms and often up to several milliseconds [17, 2], because their internal mechan-

ical switches have significant mechanical inertia while actuating metal contacts, and the HCBs must wait until the metal contacts are fully separated and then interrupt the circuit in traditional control approach. As discussed above, an HCB with 1 ms switching time needs to deal with 10 times of peak current and 100 times of peak energy compared to an SSCB with 0.1 ms switching time. Therefore, any reduction in the switching time of an HCB, especially in its mechanical switch, is a very favorable improvement to achieve better interruption performance.

2.2 Fast Mechanical Switches

Two types of mechanical switches can be found in HCBs: the interrupter type with arc-quenching capability and the disconnector type without arc-quenching capability [25]. Generally speaking, a disconnector can switch faster than an interrupter because the arc quenching time is saved from total switching time. When a normal vacuum interrupter designed for medium-voltage AC systems needs at least half a cycle (equivalently 8-10 ms) to interrupt load currents [26], the disconnectors developed for DC interruptions can switch within 1 ms [2]. The disconnector type of mechanical switches for HCBs are thus usually referred as ultra-fast disconnectors (UFDs) or fast mechanical switches (FMS).

2.2.1 Thomson coil-actuated Fast Mechanical Switches

Thomson coil actuators belong to a type of electromagnetic actuators that utilize electromagnetic repulsion forces to output large actuation force and long stroke distance [27]. Compared to other actuation mechanisms used for traditional AC switchgear like hydraulic, pneumatic or spring-loaded actuators, the electromagnetic actuators are more suitable for ultrafast interruptions within 1 ms [2]. The Thomson coil actuators have been broadly investigated in various FMS for different HCB topologies over the past 20 years [2], and an example of the Thomson-coil-actuated FMS is shown in Figure 2.2.

Given the large output force and stroke distance, the controllability of Thomson coil

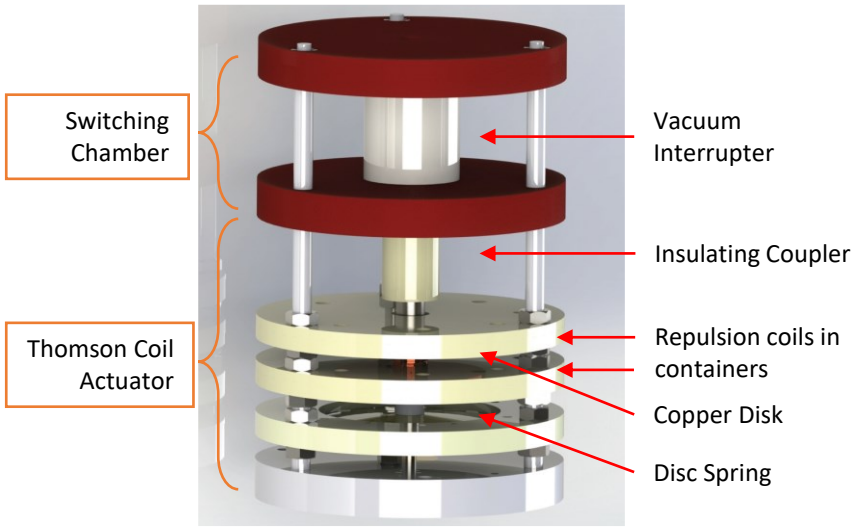

Figure 2.2: A Thomson coil-actuated fast mechanical switch with separate switching chamber and actuator [28].

actuators in FMS is quite limited, especially with regards to their travel curves. The travel curve primarily refers to the displacement of an actuator with time. If the actuator is connected to the moving contacts of FMS with mechanically stiff linkage, the travel curve outputs of the actuator are equivalent to the travel curves of moving contacts in the FMS [3]. And these travel curves of moving contacts determine the contact gap distance and the time-domain voltage withstand capability of the FMS to be used in sequential tripping of overall HCB [29], the advanced HCB control that is also called as progressive switching [5] or surge arrester insertions while contacts are moving [6]. Therefore, the control of FMS travel curves becomes increasingly important with the emerging sequential tripping and other advanced control strategies of HCBs. Implementation of sequential tripping techniques needs the travel curves of contacts to be steadily increasing with no oscillation at the end, and such travel curves should be repeatable and predefined before operations [6, 29].

Figure 2.3 shows a simplified control system of a Thomson coil actuator with only a single-turn primary coil, and a single-turn secondary coil that carries the load of moving disc and moving contacts. The circuit on the left shows the electromagnetic energy transfer

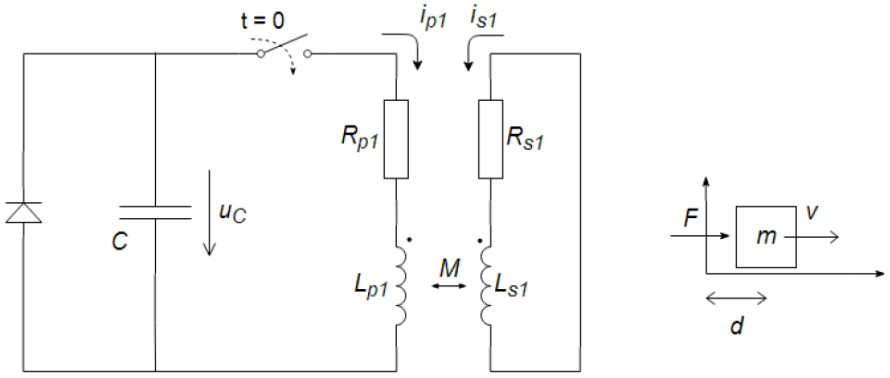

Figure 2.3: A simplified control system of a Thomson coil actuator with a single-turn primary coil and a single-turn secondary coil carrying the moving parts [30].

in the electrical domain: the discharge current from the pre-charged capacitor C becomes the input current flowing through the primary coil i_{p1}, interconnected by the mutual inductance M, a secondary current i_{s1} is induced to flow through a short-circuited secondary coil that represents the closed eddy current path within the moving disc. Thus, the generated electromagnetic repulsion force in this simplified Thomson coil actuator is [30]:

$$F_{em} = i_{p1} i_{s1} \frac{\partial M}{\partial d} = m \frac{\partial^2 d}{\partial t^2} \tag{2.3}$$

The calculation of electromagnetic repulsion force F_{em} can get very complicated due to the term $\frac{\partial M}{\partial d}$ in equation 2.3, because the mutual inductance between coils M changes with coil separation distance d and the M could only be computed numerically [27]. Once the F_{em} is known, the displacements d of moving parts in a Thomson coil actuator can be calculated to get the estimated travel curves.

A complete set of state equations with five state variables describing the simplified Thomson coil actuator (Figure 2.3) is shown in Table 2.1. It can be easily found that a single transfer function cannot be derived from Table 2.1 with capacitor voltage u_c as the input and displacement d as the output, because the state equations have partial derivatives of time t and displacement d at the same time. Without an explicit transfer function from input u_c to output d, most of the linear control strategies may not apply to this Thomson

Table 2.1: Control system of Thomson coil actuators with state variables [30].

State Variables	**State Equations**
u_c - capacitor voltage	$\frac{\partial u_c}{\partial t} = -i_{p1}/C$
i_{p1} - primary coil current	$\frac{\partial i_{p1}}{\partial t} = [L_{s1}(u_c - R_1 i_{p1} - \upsilon i_{s1}\frac{\partial M}{\partial d}) - M(-R_2 i_{s1} - \upsilon i_{p1}\frac{\partial M}{\partial d})]/[L_{p1}L_{s1} - M^2]$
i_{s1} - secondary coil/moving disk current	$\frac{\partial i_{s1}}{\partial t} = [-M(u_c - R_1 i_{p1} - \upsilon i_{s1}\frac{\partial M}{\partial d}) + L_{p1}(-R_2 i_{s1} - \upsilon i_{p1}\frac{\partial M}{\partial d})]/[L_{p1}L_{s1} - M^2]$
υ - coil separation speed	$\frac{\partial \upsilon}{\partial t} = i_{p1} i_{s1}\frac{\partial M}{\partial d} - f_{gravity} - f_{friction} - f_{contact}$
d - distance between coils/contact travel	$\frac{\partial d}{\partial t} = \upsilon$

coil actuator. Thus the control of travel curves in Thomson coil actuators is typically implemented experimentally with the assistance of finite-element, multi-domain simulations [7, 27, 31, 32]. And the linearity of controlled travel curves from experimentally-damped Thomson coil actuators is relatively low compared to the ideal travel curve. For example, as shown in Figure 2.4 cited from [7], the actively damped travel curves from the Thomson coil-actuated FMS (Figure 2.2) by a closing coil still had severe +/- 25% oscillations. The actuation may even fail after a slight 15 V change in its u_c input to the Thomson coil actuator.

Besides the limitations on controllability, the energy conversion efficiency of Thomson coil actuators is also very low. Only 5% of input electric energy has been converted to the kinetic energy of moving contacts, and this is already a fair performance [33]. Moreover, the Thomson coil actuator is not integrated within the switching chamber as shown in Figure 2.2. The additional mechanical linkage has increased the complexity of switching motion control and the total volume of Thomson coil-actuated FMS. Both disadvantages of low driving efficiency and low power density could severely impede the adoption of Thomson coil-actuated FMS in electrified transportation applications, such as electrified

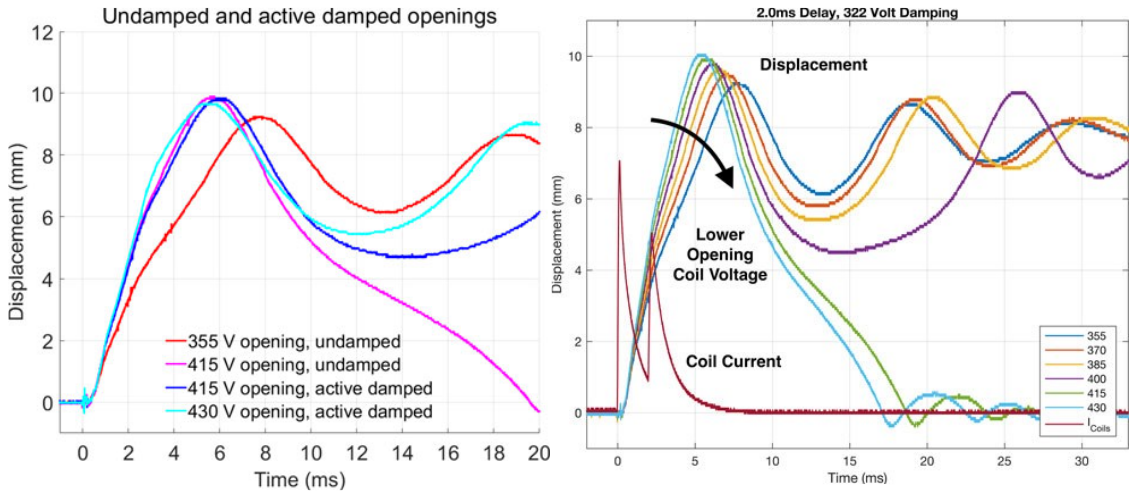

Figure 2.4: Reported travel curves with a damping coil from the Thomson coil-actuated FMS (whose mechanical structure is shown in Figure 2.2) [7].

ships and aircraft, in which the efficiency and power density requirements are very high.

2.2.2 Piezoelectrically-Actuated Fast Mechanical Switches

For the purpose of mitigating the problems in the Thomson coil-actuated FMS, a PA-FMS has been proposed initially for electrified shipboard application [34]. As shown in the section view of Figure 2.5, an amplified piezoelectric actuator APA1000XL from Cedrat Technologies® is housed inside the switching paddle with the polyether ether ketone (PEEK) insulator as the mechanical support [35]. The deformation of APA1000XL actuator is directly transferred to the movements of moving contacts without redundant mechanical linkage, so the ultrafast PA actuations can be preserved and the overall PA-FMS structure is very compact.

The operation principles of APA1000XL actuator in the PA-FMS prototype is straightforward. According to the system view of Figure 2.5, a piezoelectric driver is used to output 0 - 150 V voltage for driving the actuator to reach a maximum displacement of 1 mm. This piezoelectric driver can be a high-voltage DC power supply for compactness or a high-bandwidth power amplifier for ultrafast switching performance, and both drivers are commercial products with testified reliability [3]. Moreover, the actuation efficiency

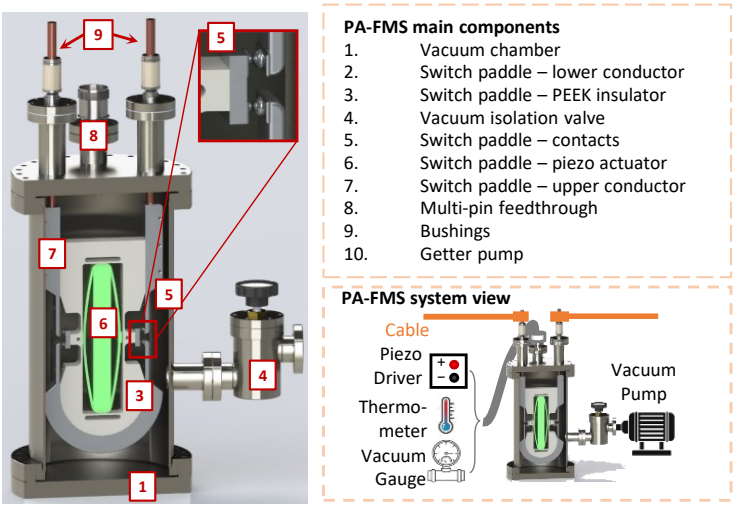

Figure 2.5: Section view and system view of a PA-FMS prototype with amplified piezoelectric actuator APA1000XL being integrated within the switching chamber [3].

Table 2.2: Comparison of Thomson coil-actuated FMS with PA-FMS [2, 3].

Actuation Characteristics		**Thomson Coil Actuated FMS**		**Piezoelectrically Actuated FMS**
Application		HVDC; MVDC		Specialized for MVDC
Voltage rating	+	Beyond 100 kV	−	Up to 15 kV
Response time	−	Varying	+	Up to 0.5 ms
Driving energy	−	Kilojoule-level	+	Joule-level
Controllability	−	Nonlinear system; ON/OFF control	+	Quasi-linear system; PID control
Basic structure	−	• Driving circuit • Coils & disks • Damping & latch • Vacuum interrupter	+	• Piezo driver • Actuator-integrated switch

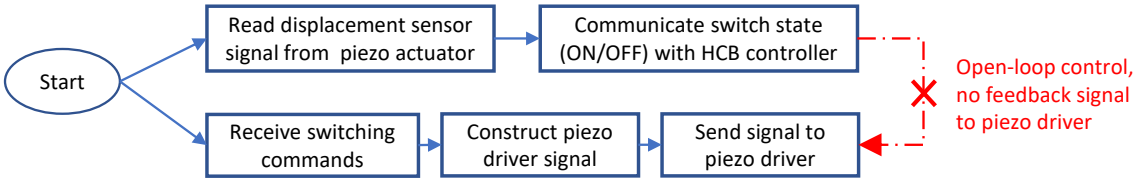

Figure 2.6: Function blocks of the open-loop controller in the former PA-FMS prototype.

of APA1000XL actuator is very high because only a few joules of driving energy suffices for the actuation of APA1000XL [35]. Comparing to the Thomson coil actuation solution presented in the previous subsection, this PA-FMS has a lower response time, a lower actuation energy consumption and a more integrated structure as summarized in Table 2.2.

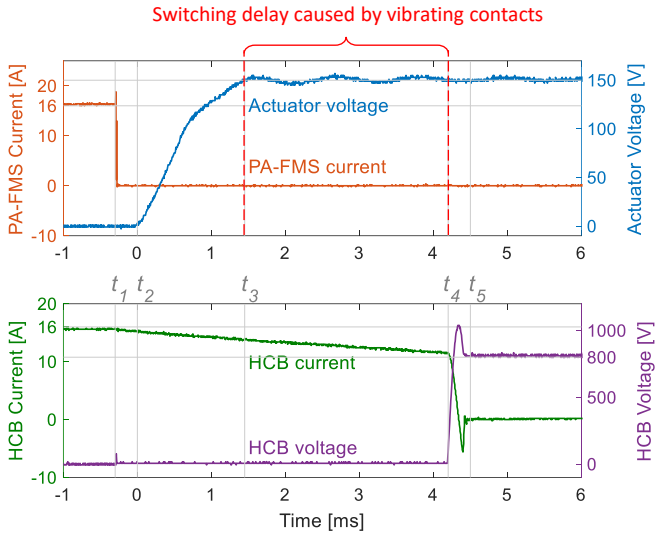

Figure 2.7: Experimental waveforms of the PA-FMS prototype in HCB integration tests.

Although the previous vacuum-insulated PA-FMS prototype has demonstrated distinguished performance including an actuator opening time of 1 ms, a breakdown voltage of over 20 kV, and a continuous current rating of 500 A with the help of thermosyphon bushings [36], the control of this PA-FMS prototype is the most basic open-loop strategy without no feedback from the sensing to the driving as shown in Figure 2.6. The direct consequence of this primitive control is the contact vibration that once led to failed current interruptions in HCB integration tests, so a conservative safety margin around 3 ms was inserted before interrupting the current. Even in a successful opening as shown in Figure 2.7, this contact vibration problem has prolonged the total switching time of HCB from 1.4 ms to 4.8 ms [3].

The actuation targets are harder to achieve in a supercritical-fluids-insulated (SCF-insulated) PA-FMS prototype that is currently developing (Figure 2.8) due to many reasons. First of all, the targeted PA-FMS opening time is merely 0.25 ms, which is approaching the

theoretical minimum switching time $t_{sw,min} = 100\mu s$ of the selected Cedrat PPA120XL actuator (see details with equation 2.10) [4, 37]. Secondly, the moving contacts, conductor and insulator parts of PA-FMS constitute a total payload of about 500 g for the PPA120XL actuator to carry, which is 1.3 times of the actuator's self weight [38]. Moreover, the PPA120XL actuator is expected to reach its full-range displacement whenever separating moving contacts in PA-FMS, so that the driving capability of PPA120XL will be fully exhausted to output as much displacement as possible [38]. Not to mention the supercritical fluids are novel insulating materials whose compatibility with PAs are under investigations [39, 40].

Collectively, the SCF-insulated PA-FMS prototype is targeting a fast response, a high payload and a large displacement simultaneously in the same actuation. It is very challenging to accomplish these goals simultaneously because of the tradeoffs among mechanical load, response time (or control bandwidth) and displacement range in PAs [41]. The PA control problem gets even more complex when a vibration-free travel curve in PA-FMS is needed. Therefore, the major difficulty of this study is to achieve three actuation targets simultaneously meanwhile attenuating the vibration in PA travel curves. There are certainly more expectations on the PA performance like a high acceleration at the beginning of contact travel to facilitate arc quenching, a high blocked force output from the PA to reduce the PA-FMS conduction losses, and the high reliability and life expectancy of the PA within SCF environment.

Another type of PA-FMS proposed in literature: it is not a disconnector type FMS, but more of an interruptor type that is prone to arcing between contacts [42, 43]. This contactor-like PA-FMS utilizes the contact voltage across the molten metal bridge between separating contacts (while significantly large load or fault current is still flowing through) to commutate current from the FMS branch to the power electronic branch in an HCB [44]. The boundary values of this contact voltage are carefully determined as the boiling voltage (0.8 V for copper and 2.1 V for tungsten [45]), and the turning-on voltage of power elec-

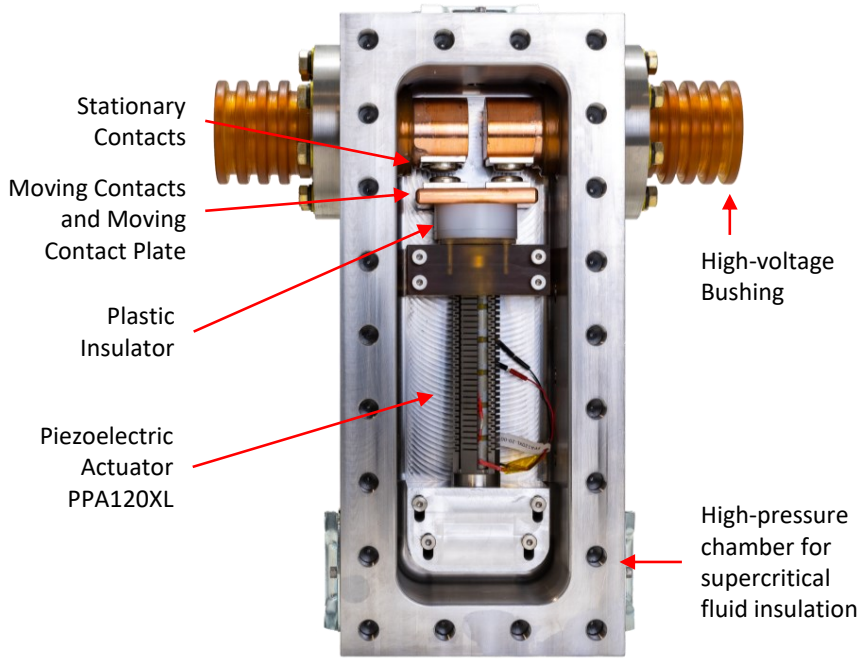

Figure 2.8: Supercritical-fluids-insulated PA-FMS prototype (under development) with parallel piezoelectric actuator PPA120XL being integrated within the high-pressure chamber.

tronics branch should be smaller than this boiling voltage to achieve arc-less commutation (no arcing between contacts). Therefore, there is no need for a separate load commutation switch in an HCB using contactor-like PA-FMS, because the counter voltage that forces current to commutate is generated through the contactor-like PA-FMS. This working principle is different from the disconnector-type PA-FMS as discussed above, because the disconnector-type PA-FMS provides no commutation assistance and a separate current communtation device must be used [3]. However, the development of this contactor-type PA-FMS has not mentioned the controller design of piezoelectric actuator for better actuation performance.

2.3 Piezoelectric Actuators

In pursuit of the representative control system and state equations of piezoelectric actuators, such as Figure 2.3 and Table 2.1 for Thomson coil actuators, the fundamental knowledge

of piezoelectric actuators is first reviewed in this section.

2.3.1 Piezoelectricity in Ceramics

Piezoceramic materials, such as barium titanate and lead zirconate titanate (PZT), exhibit a strong piezoelectric coupling effect that can generate a macroscopic change of electric polarization under applied mechanical load, or yields mechanical deformations under applied electric fields [46]. The former phenomenon is defined as the direct piezoelectric effect being utilized in piezoelectric sensors, and the latter phenomenon is defined as the inverse piezoelectric effect being used in piezoelectric actuators [46]. Both effects induce changes of electric polarization with limited free electric charges; thus, the piezoceramic materials are electrical insulators that exhibit more capacitive features under applied voltage [46].

The widely-accepted constitutive equations describing linear piezoelectricity were provided in the IEEE standard 176-1987 as [47]:

$$D_m = \varepsilon_{mn}^{T} E_n + d_{mkl} T_{kl} \tag{2.4}$$

$$S_{ij} = d_{ijn} E_n + s_{ijkl}^{E} T_{kl} \tag{2.5}$$

The descriptions and units of notations used in equation 2.4 and equation 2.5 are given in Table 2.3. The vectors for the electrical field $\vec{D}, \vec{E}$ contain three components along normal axes x, y, z. And the vectors for the mechanical field $\vec{T}, \vec{S}$ contain six components, with three of them for normal/tensional components and three for shear/rotational components. Considering the symmetries within piezoelectric materials [46, 48], the expanded

Table 2.3: Expressions in constitutive equations of linear piezoelectricity [46].

Notation	Description	Unit
D_m	Electric flux density; vector	C*m^{-2}
E_n	Electric field intensity	V*m^{-1}
S_ij	Mechanical strain; tensor rank 2	-
T_kl	Mechanical stress; tensor rank 2	N*m^{-2}
ε^T_{mn}	Electric permittivity; tensor rank 2	F*m^{-1}
d_{mkl}, d_{ijn}	Piezoelectric strain constants; tensor rank 3	C*N^{-1}; m V^{-1}
s^E_{ijkl}	Elastic compliance constants; tensor rank 4	m^2*N^{-1}

equations describing linear piezoelectricity become:

$$\begin{bmatrix} D_1 \\ D_2 \\ D_3 \end{bmatrix} = \begin{bmatrix} \varepsilon^T_{11} & 0 & 0 \\ 0 & \varepsilon^T_{11} & 0 \\ 0 & 0 & \varepsilon^T_{33} \end{bmatrix} \begin{bmatrix} E_1 \\ E_2 \\ E_3 \end{bmatrix} + \begin{bmatrix} 0 & 0 & 0 \\ 0 & 0 & 0 \\ d_{31} & d_{31} & d_{33} \end{bmatrix} \begin{bmatrix} T_1 \\ T_2 \\ T_3 \end{bmatrix} \tag{2.6}$$

$$\begin{bmatrix} S_1 \\ S_2 \\ S_3 \end{bmatrix} = \begin{bmatrix} 0 & 0 & d_{31} \\ 0 & 0 & d_{31} \\ 0 & 0 & d_{33} \end{bmatrix} \begin{bmatrix} E_1 \\ E_2 \\ E_3 \end{bmatrix} + \begin{bmatrix} s^E_{11} & s^E_{12} & s^E_{13} \\ s^E_{12} & s^E_{11} & s^E_{13} \\ s^E_{13} & s^E_{13} & s^E_{33} \end{bmatrix} \begin{bmatrix} T_1 \\ T_2 \\ T_3 \end{bmatrix} \tag{2.7}$$

When the applied electric field is zero $E_1 = E_2 = E_3 = 0$, the Poisson's ratio of piezoceramic ν can be obtained by referring to following equations (assuming the piezoceramic is isotropic and elastic) [49]:

$$\begin{bmatrix} S_1 \\ S_2 \\ S_3 \end{bmatrix} = \begin{bmatrix} s^E_{11} & s^E_{12} & s^E_{13} \\ s^E_{12} & s^E_{11} & s^E_{13} \\ s^E_{13} & s^E_{13} & s^E_{33} \end{bmatrix} \begin{bmatrix} T_1 \\ T_2 \\ T_3 \end{bmatrix} = \frac{1}{E_Y} \begin{bmatrix} 1 & -\nu & -\nu \\ -\nu & 1 & -\nu \\ -\nu & -\nu & 1 \end{bmatrix} \begin{bmatrix} T_1 \\ T_2 \\ T_3 \end{bmatrix} \tag{2.8}$$

where E_Y is the Young's modulus of the piezoeceramic.

For a multilayer stack PA used in PA-FMS, only a normal electrical field (e.g. E_3 in Figure 2.9) is applied to the piezoceramic and accompanied by mechanical stress in the same direction. Since the multilayer stack actuator works in the longitudinal mode, its constitutive equations can be simplified into the ones in Figure 2.9 after neglecting shear/rotational components.

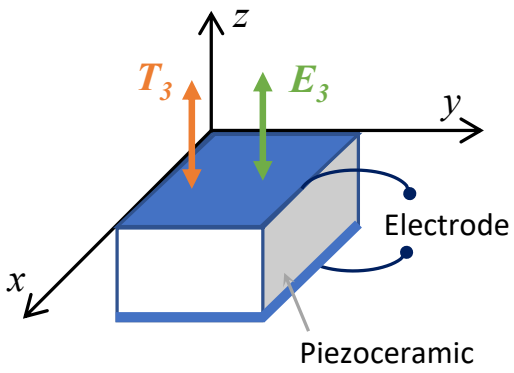

$$E_1 = 0; \qquad E_2 = 0;$$

$$T_1 = 0; \qquad T_2 = 0;$$

$$D_3 = \varepsilon_{33}^T E_3 + d_{33} T_3$$

$$S_3 = d_{33} E_3 + s_{33}^T T_3$$

Figure 2.9: Longitudinal mechanical stress and electrical field on a single piece of piezoceramic that is sandwiched by surface electrodes.

The theoretical efficiency of energy conversion within piezoelectric materials can be derived from the constitutive equations of linear piezoelectricity using an electromechanical coupling factor k. For a multilayer stack PA with only longitudinal electric field E and mechanical stress T, the electromechanical coupling factor k_{33} can be calculated following equation 2.9 [46]. Here the subscript "33" means the input excitation is along the z-axis and the output response is along the same z-axis. Calculated with the material properties of piezoceramic possibly used in Cedrat actuators [50], the value of k_{33} can reach up to 60% - 70%, which is equivalent to 60% - 70% in the theoretical electromechanical energy conversion efficiency of piezoelectric actuations. Compared to the merely 5% energy conversion efficiency in Thomson coil actuators [33], the PAs are very efficient that they can work on just several Joules of energy input for actuations [2]. For example, the PPA40L actuator has its capacitance of 8.8 μF, so the electrical energy stored in the piezoceramic of PPA40L actuator is merely 0.1 J under 150 V driving voltage for full-range

displacement ($W = 1/2CV^2$). There are undoubtedly electrical losses and electromechanical conversion losses that require more than 0.1 J electrical energy to be inputted into the PPA40L actuator. Given these losses, the total actuation energy consumed by a PPA40L actuator is far from the kJ-level energy consumption in most Thomson coil actuators [2].

$$k_{33} = \frac{convertedmechanicalenergy}{inputelectricalenergy} = \frac{d_{33}^2}{\varepsilon_{33}^T s_{33}^E} \tag{2.9}$$

2.3.2 Resonance and Vibration

Because of the electromechanical coupling of piezoelectric materials, the fundamental resonance modes become visible in their impedance curves. A sample impedance curve of a piece of longitudinally polarized piezoceramic is shown in Figure 2.10 [46]. In the low-frequency range, the piezoceramic behaves majorly capacitive impedance with a constant phase value of $-\pi$ and linearly decreasing magnitude value. The most dominant mechanical vibration will happen at the resonance frequency, which is then accompanied by the antiresonance behavior to constitute the dominant pair of resonance-antiresonance. There are more resonance-antiresonance pairs coming out at much higher frequency ranges when the piezoelectric response changes from thickness extension mode to radial mode [46]. The thickness extension mode is typically exploited in stack-shape PAs to generate longitudinal displacements. In contract, the radial mode can be found from disc-shape piezoelectric sensors which emit and receive ultrasonic waves radially during normal operations [46].

The dominant resonance frequency of a multilayer stack actuator determines how fast this actuator can be driven. PA manufacturers have suggested the fastest displacement of a PA can occur in 1/3 of its resonant period [51]:

$$t_{p,min} = t_r/3 \tag{2.10}$$

where $t_{p,min}$ is the minimum rising time in switching operations, and t_r is the time period

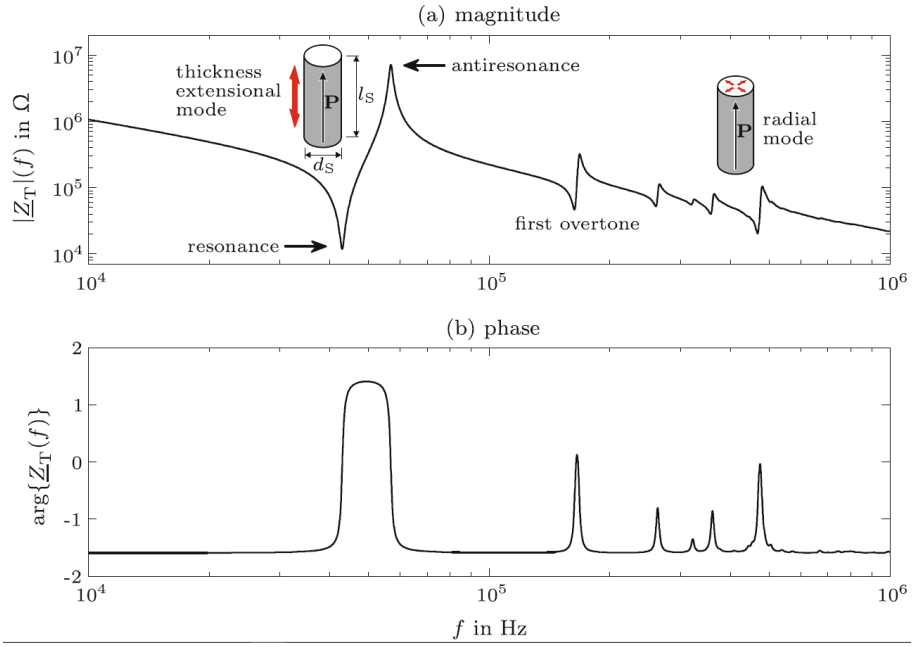

Figure 2.10: Simulated impedance curve of a piece of longitudinally polarized piezoceramic [46].

at actuator's resonant frequency [37]. Detailed estimations of $t_{p,min}$ with different loading conditions on a PPA40L actuator can be found in Figure 3.12 in Chapter 3,

Besides using impedance curves that illustrate the electrical impedance $\tilde{Z} = \tilde{V}/\tilde{I}$, the vibration nonlinearity of PAs can be studied with system transfer function of $G_v(s) = X_{piezo}(s)/V_{in}(s)$ [52, 53]. Although characteristics yield similar Bode plots as in Figure 2.10 and Figure 2.11, the former Bode plot shows a pure electrical characteristic of PA. In contrast, the latter Bode plot shows an electromechanical transfer characteristic of PA. For vibration damping studies, the latter Bode plot with $G_v(s) = X_{piezo}(s)/V_{in}(s)$ is more suitable by considering travel curve x_{piezo} as its output signal. As shown in Figure 2.11, there is also a resonant peak in the Bode plot with a negative gain margin, which means the overall PA is prone to vibrational dynamics once the input signal has high-frequency components as in a step signal or a ramp signal [52].

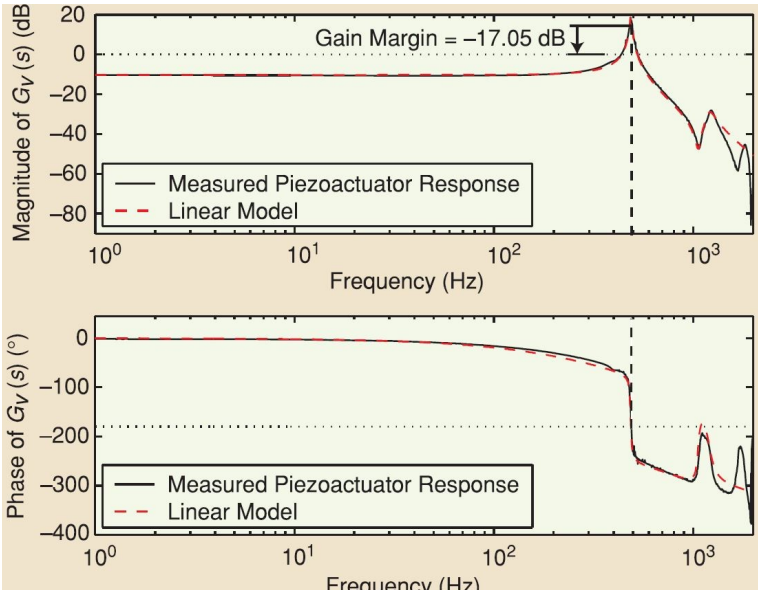

Figure 2.11: Measured and simulated electromechanical frequency response of a PA bothered with vibrational dynamics [52]. The transfer function $G_v(s)$ has actuator displacement x_{piezo} as the output and driving voltage V_{in} as the input.

2.3.3 Parallel Prestressed Stack Actuators

Piezoelectric stack actuators have multiple layers of piezoceramic being stacked up to achieve higher stroke distances in the longitudinal direction. As shown in Figure 2.12(a) [46], the conventional setup of a piezoelectric stack actuator consists of a large number of polarized piezoceramic disks with both positive electrodes and negative electrodes, and the electric polarization **P** exist in every piezoceramic disks pointing from the positive to the negative electrode. As there are numerous wires used to interconnect electrodes in hundreds of disks, the wiring efforts and manufacturing costs of conventional stack actuators are very high [46].

The more advanced co-fired multilayer stack actuators have hundreds of piezoceramic layers (50 - 100 μm thickness) and screen-printed metallic film as electrodes [46, 54]. The piezoelectric stack actuators mentioned in this dissertation, including the Cedrat APA1000XL, PPA120XL and PPA40L actuators, share similar structures such as Figure 2.12(b).

Another shared feature among actuators used in this study is that they are all prestressed

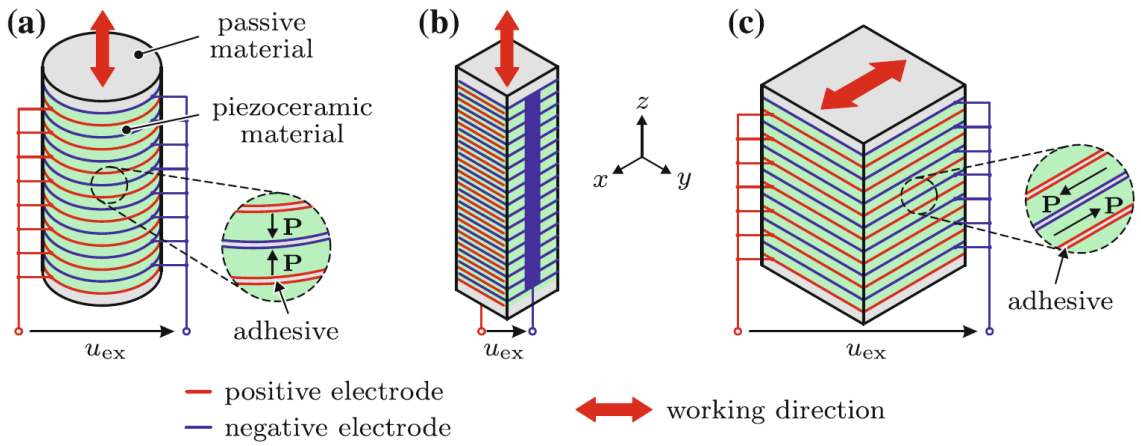

Figure 2.12: Schematic setup of (a) conventional longitudinal stack actuators with high wiring effort, (b) co-fired multilayer stack actuators for large quantity manufacture, and (c) shear output stack actuator **P** indicates the direction of electric polarization [46].

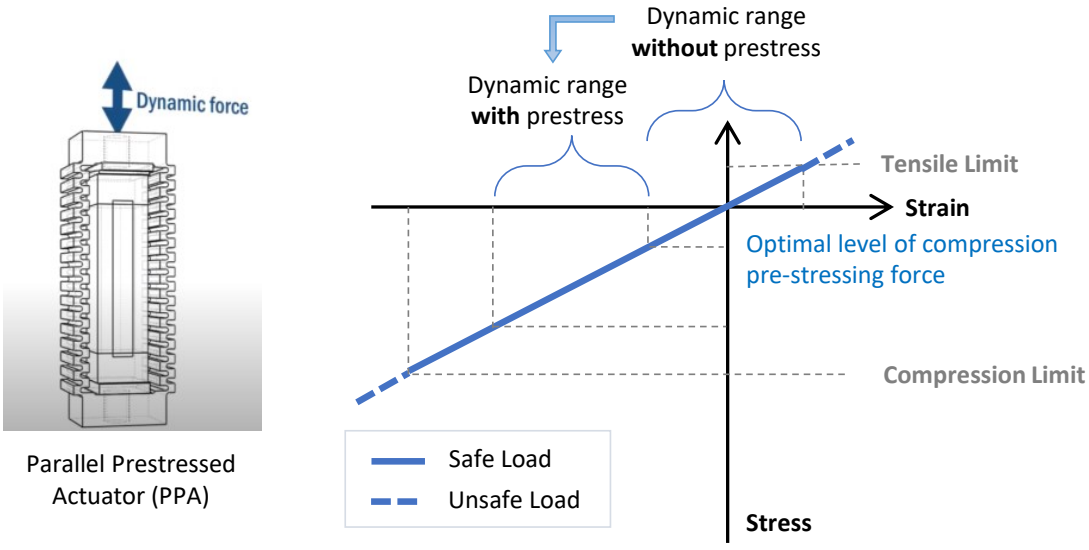

Figure 2.13: Illustration of prestressing benefits in a parallel prestressed actuator (PPA) under dynamic load forces [55].

versions. Mechanical prestressing means applying a static pressure in negative z-axis to the piezoceramic stack at rest to counteract any possible tensile stress during operations. Similar to other ceramic materials, piezoceramic is also fragile to tensile stress under pulling forces, so that the tensile stress limits of PAs are as low as 5 to 10 MPa [4]. After adding a mechanical prestress up to 30 MPa, the dynamic range of strain-stress response could be shifted to a safer region as shown in Figure 2.13 [55]. Based on practical experience with PAs in this study, the non-prestressed versions of actuators are very vulnerable to pulsed tensile stresses during switching operations, which leads to cracking and ultimately breakage. Comparatively, the prestressed actuators are better candidates for switching operations in PA-FMS because of their enlarged dynamic operation range and enhanced tolerance to tensile forces as illustrated in Figure 2.13.

2.3.4 Cedrat PPA40L and PPA120XL Actuators

There are two Parallel Prestressed Actuators (PPAs) being used in this study, and they are both commercial products provided by Cedrat Technologies®. The prestress is generated by an external spring frame made of stainless steel to protect the internal multilayer piezoelectric stacks against tensile forces. The multilayer piezoelectric stacks in PPAs are most likely the AE series resin-coated actuators manufactured by TOKIN®, a KEMET® company.

PPA120XL is the largest module in the PPA series with the highest stroke distance of 130 μm and the largest blocked force of 9300 N. The blocked force is defined as the maximum force generated by the actuator when its stroke output is zero. Comparatively, the PPA40L is a shorter actuator with a stroke distance of 44 μm and a blocked force of 1500 N. It is also constructed with smaller L-series piezoceramic stacks than XL-series piezoceramic stacks in PPA120XL. PPA120XL is the actuator to be installed in the SCF-insulated PA-FMS prototype. During the controller strategy development phase, a PPA40L actuator is used as the control object in tests to avoid potential damage to the valuable

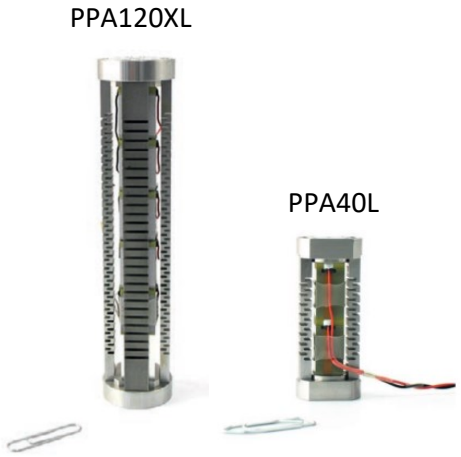

Figure 2.14: Cedrat® PPA120XL actuator and PPA40L actuator as the control objects in this dissertation [38, 56].

Table 2.4: Datasheet information of PPA120XL actuator and PPA40L actuator [38, 56].

Parameter	**PPA120XL**	**PPA40L**
Nominal stroke [μm]	130	44
Displacement resolution [nm]	7.3	2.5
Blocked force [N]	9300	4700
Stiffness [N/μm]	71	110
Resonance frequency [Hz]	3300	8300
Voltage range [V]	$-20 \leftrightarrow 150$	$-20 \leftrightarrow 150$
Capacitance [μF]	51	8.8
Dimension [mm]	140 (H) * 30 (W) * 30 (L)	57 (H) * 18 (W) * 24 (L)
Mass [g]	380	92

PPA120XL actuator. Other physical differences between these two PPAs are shown in Figure 2.14, and their datasheet information is provided in Table 2.4.

2.3.5 Reliability and Compatibility

Due to the low tensile strength of piezoceramic and repetitive deformations during operations, cracks commonly exist in aged PAs and finally lead to failures. A lot of parameters including humidity, temperature and oscillation contribute to the crack growth inside the piezoceramic [57]. High humidity is the most severe environmental condition for PAs because it can easily lower the lifetime by some orders of magnitude, such as the lifetime in 80%RH was shorter by 2 to 3 decades than that at 10%RH [58]. In a silver-palladium electrode actuator in the high-humidity environment [58], the dissolved Ag ions could move from the anode through cracks and voids inside the piezoceramic, and then reconverted into metallic silver on the surface of cathodes and grain boundaries as in Figure 2.15. Such silver dendrites noticeably decrease the resistance between the anode and the cathode, which lead to partial discharge, local heating, and electrical breakdown.

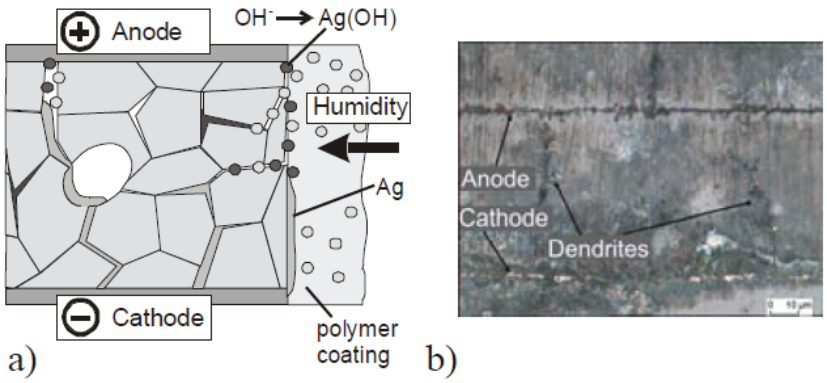

Figure 2.15: Humidity-driven degradation processes in silver-palladium electrode actuator under DC stress [58].

The compatibility between PA and supercritical carbon dioxide ($scCO_2$) has been studied in [59] to ensure the normal operations of the immersed PA inside $scCO_2$ environment. Figure 2.16 illustrated the phase transitions from gas/liquid two-phase state to supercritical

one-phase state in the CO_2. The driving voltage and leakage current through the mini PA had been online-monitored during the CO_2 immersion. It was confirmed experimentally that reliable operations of a multilayer piezoelectric actuator had been performed in both supercritical and liquid carbon dioxide environment after short-time immersion [59].

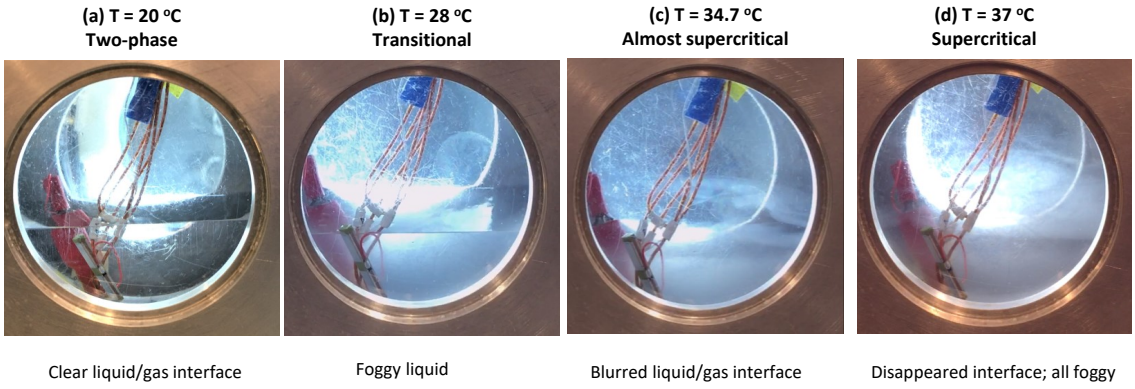

Figure 2.16: Photos of phase transitions of CO_2 in the high-pressure optical chamber during PA-in-CO_2 immersion test [58].

2.4 Modeling and Control of Piezoelectric Actuators

2.4.1 Controllability of Piezoelectric Actuators

So far, the modeling and control of piezoelectric stack actuators are focused mostly on nanopositioning stages within precision equipment like atomic force microscopes [14, 60], micromanipulators [61, 62, 63], scanning probe microscopes [64], and ultra-precision machine tools [65, 66]. The primary control target for actuators in nanopositioning stages is the accuracy of positioning while tracking a predefined trajectory [13]. Any nonlinearity in actuator movements will cause positioning mismatch and thus loss of accuracy in the equipment. For example, in an atomic force microscope, the nanometer-level vibration of piezoscanner under 50 Hz high-frequency scanning mode will cause ripples in rendered microscope images as shown in Figure 2.17(a)(b) [14]. Moreover, the piezoscanners in atomic force microscopes are also prone to creep and hysteresis nonlinearities, so the rendered images may deviate significantly from reality as shown in Figure 2.17(c)(d) [52]. To

avoid these problems, there are numerous models and controls being developed for better trajectory-tracking actuations from piezoelectric stack actuators.

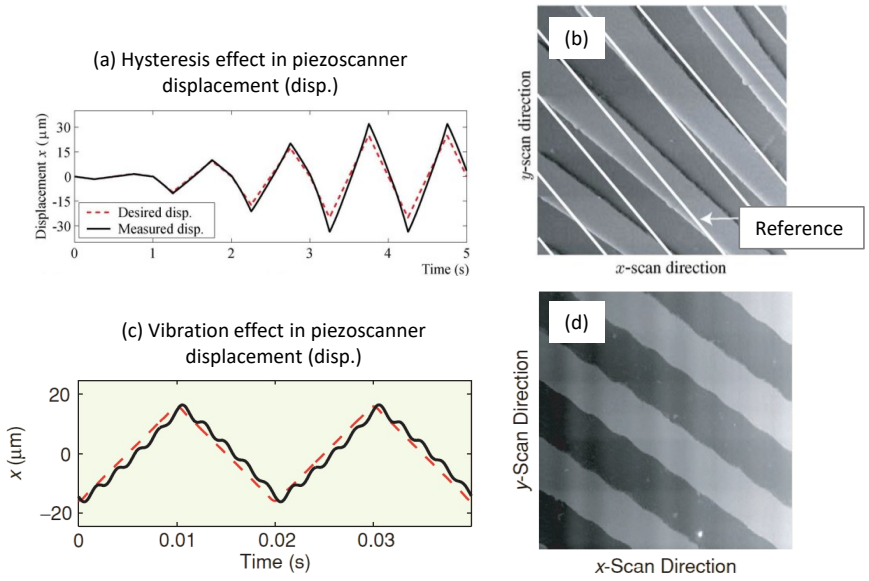

Figure 2.17: Effects on piezoscanner nonlinearities within atomic force microscopes. (a) open-loop displacement affected by hysteresis; (b) scanned image distorted by hysteresis and creep effects; (c) high-frequency scanning displacement affected by vibration; (d) scanned image distorted by vibration nonlinearity [14, 52].

The application of piezoelectric stack actuators in PA-FMS requires different performance parameters from those in nanopositioning stages. Actuations in PA-FMS do not need to be precise and accurate in nanometers. Instead, these actuations should displace a heavy payload to a large displacement within a short period of switching time. In microscopy applications, the achievable fastest scanning period is at least 10 times of the dominant resonant period [14, 67]. Whereas in the SCF-insulated PA-FMS, the targeted switching time of PPA120XL actuator is approaching 1/3 of the dominant resonant period. And the travel curves should be free of excessive vibration with controlled overshoot and undershoot.

These control objectives of PPA120XL actuator seem difficult even when compared with other control strategies optimized for step responses in Table 2.5. Furutani *et al.*

Table 2.5: Comparison on switching motion performance between the reported and the proposed control strategies [69].

Strategy	Furutani *et al.*	Li *et al.*	Gu *et al.*	**Proposed**
Control Purpose	Trajectory tracking	Trajectory tracking	Trajectory tracking	Switching motion
Rise/Fall Time t_r [ms]	0.03	0.37	6	≤ 0.25
Overshoot/Undershoot	89%	35%	1.5%	$\leq 10\%$
Max Displacement x [μm]	3	7	7.5	40;100*
Load Mass m [g]	16	430	250	500

*Max displacement goal for PPA40L actuator is 40 μm; for PPA120XL actuator is 100 μm

proposed a displacement control on a small piezoelectric actuator with 16 g of weight and 16 μm of max deformation, so a step response of 3 μm was achieved with merely 0.03 ms of rising time but a large 89% overshoot [68]; Li *et al.* studied the step responses of a piezoelectric stack actuator with a heavy host system, and proposed a principle-based model to achieve damped actuations. Yet, the total displacement was kept at a low level of 7 μm [69]. The piezoelectric positioning stage used by Gu *et al.* also reached up to 7.5 μm of displacement with negligible subsequent vibration in travel curves, but the rising time was as high as 6 ms in that trajectory-tracking control strategy [16].

Compared to all the controls listed above, the set of objectives for PPA120XL actuator seems not easily achievable with common trajectory-tracking controls. There are studies about using piezoelectric stack actuators as high-speed switching devices in liquid injection systems before PA-FMS applications, while the discussions on the modeling and control side is very limited [70, 71]. So the existing solutions may not be effective even with a lowered requirement on the displacement of PPA40L actuator, a substitute of PPA120XL actuator during the development phase. As a result, a new set of control strategies optimized for switching motions must be proposed and constructed for the SCF-insulated PA-FMS.

2.4.2 Comprehensive Dynamic Model and Nonlinearity Compensation

The aforementioned linear constitutive equations (Equation 2.4, 2.5) can describe the piezoelectricity from the theoretical perspective, but they cannot be directly applied in control systems for three practical reasons. Firstly, the linear constitutive equations do not describe creep, hysteresis and vibration nonlinearities that have bothered practical piezoelectric actuations. In contrast, many advanced control algorithms have targeted to remove these nonlinearities from piezoelectric actuations [61]. Secondly, the linear constitutive equations were developed from piezoceramic materials working under high-frequency, small-signal loading conditions dominated by weak-field measurements using the resonance-antiresonance method (Figure 2.10) [47, 46]. Nowadays, after piezoceramic materials being manufactured into sensors and actuators, piezoelectric devices commonly work under large-signal mechanical stresses or electrical fields to produce large displacement and force signals. Thus, the conventional small-signal assumptions become inapplicable for modern piezoelectric devices [72]. Thirdly, another assumption in derivations of linear constitutive equations is a purely energy-conservative field. However, in reality, the piezoelectric actuators dissipate a significant amount of energy under large-signal loading conditions [61].

To overcome the limitations of constitutive equations, Goldfarb and Celanovic proposed a comprehensive model based on static and dynamic behaviors of piezoelectric stack actuators with lumped electrical and mechanical parameters in 1997 (Figure 2.18(a)(b) [61]). This model included the Maxwell representation of hysteresis and dynamic aspects like second-order components in mechanical domain [73]. Over the years, the representation of hysteresis has evolved from physics-based models to phenomenological models constructed with differential equations or hysteresis operators [13]. Phenomenological hysteresis models can be driven without knowledge of physical system characteristics [74], and some operator-based phenomenological models like the Prandtl-Ishlinskii model have analytical inverses that makes hysteresis compensations feasible in controllers [75].Compared to the improvements on hysteresis representations, the improvements on other elements of

the Goldfarb and Celanovic model (Figure 2.18) is less frequent. There has been a change about including the actuator driver into the electrical circuit by adding the amplifier gain plus an internal resistance [16, 76]. In this dissertation, a modified version of Goldfarb and Celanovic model with an additional damping resistor in the electrical domain is used.

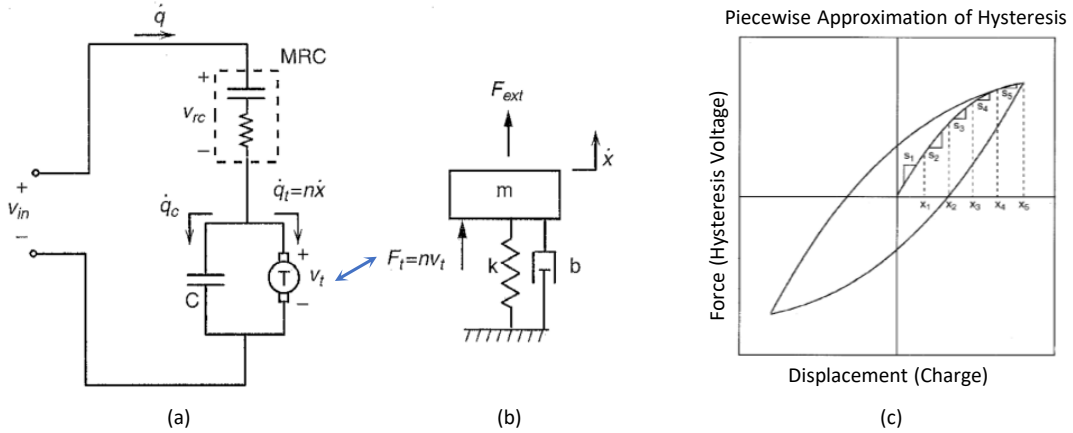

Figure 2.18: Comprehensive dynamic model of a piezoelectric stack actuator with interconnections between (a) electrical domain and (b) mechanical domain with transformation ratio n. The Maxwell resistive capacitance (MRC) is a nonlinear element for (c) piecewise approximation of hysteresis. [61]

Table 2.6: State equations of piezoelectric stack actuator in Goldfarb and Celanovic model with state variables [61].

State Variables	**State Equations**
V_{in} - Driving voltage	$V_{in} = V_t + V_{rc}$
V_t - Transformation voltage	$V_t = F_t/n$
q - Charge in piezoceramic	$V_{rc} = mrc(q)$
x - Displacement/contact travel	$mx'' + bx' + kx = F_t + F_{ext}$

The state equations from Goldfarb and Celanovic model (Figure 2.18) is given in Table 2.6 [61]. Compared to the partial differential equations in the control system of Thom-

son coil actuators of Table 2.1, the state equations of PA control system are mostly linear equations without derivations. The first three equations about V_{in}, V_t and V_{rc} describe voltage relationships in the electrical domain. As shown in Figure 2.18(c), the $mrc()$ is a piecewise-linearized representation of electrical hysteresis. And the $V_t = F_t/n$ relates an electric voltage V_t with a mechanical force F_t through an electromechanical transformation ratio n. The forth equation describes a classic mass-spring-damper system representation of PA in the mechanical domain [61, 77, 78].

2.5 Chapter Summary

This chapter reviews the existing literature on hybrid circuit breakers, fast mechanical switches and piezoelectric actuators. According to this literature review, the PA-FMS can perform more delicate switching operations than Thomson coil-actuated FMS. However, the formerly built PA-FMS prototype was controlled only in an open-loop manner and failed to demonstrate the advantages of piezoelectric actuators. The selected Cedrat PPA actuators for the proposed SCF-insulated PA-FMS prototype have nm-range displacement resolution and down to 100 μs switching time, yet they are limited by displacement non-linearities including hysteresis and vibration. A comprehensive dynamic model of PAs can be utilized for switching motion controller constructions.

CHAPTER 3

OPEN-LOOP PERFORMANCE AND MODEL CONSTRUCTION

In this chapter, the experimental process of obtaining the open-loop travel curves and identifying the piezoelectric actuator model parameters are presented. The vibration in experimentally obtained open-loop travel curves is recognized with their origins being determined.

3.1 Open-loop Driving System

One major advantage of PAs over Thomson coil actuators is the simplicity of their driving system, and Figure 3.1 shows the basic structure of an open-loop controlled driving system for PAs. There are only three components in the power loop of driving system in Figure 3.1: a function generator as the signal source, a power amplifier as the piezo driver, and the actuator to be driven. A fourth component can be the sensors that collect data from the actuator, such as a displacement sensor for measuring PA travel curves.

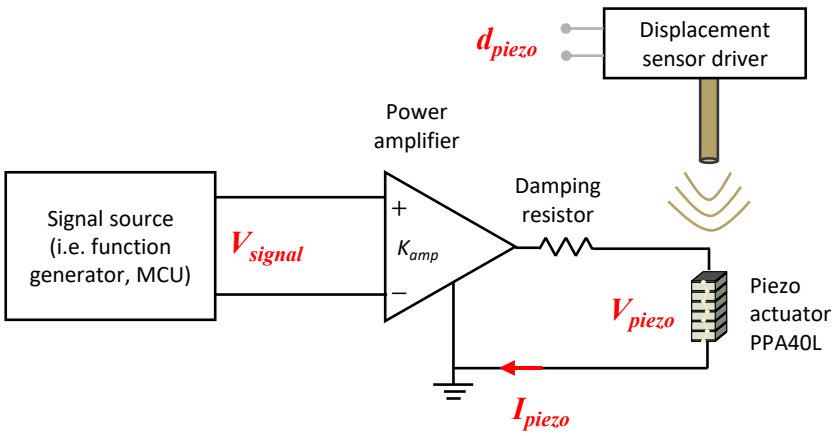

Figure 3.1: Open-loop driving system of PA.

The first component in Figure 3.1, a function generator, provides the input signal V_{signal}

to the piezo driver. The V_{signal} is usually a single pulse with predefined lead time t_{lead} and tail time t_{tail}. Intuitively, changing the t_{lead} and t_{tail} in V_{signal} can modify the waveshape of driving voltage at the output of piezo driver, and the travel curves of PA can be modified accordingly. More information about the second component in Figure 3.1, a piezo driver, will be given in the next subsection. The third component in Figure 3.1, a PPA40L actuator, will be analyzed throughout this thesis. And the fourth component in Figure 3.1, a displacement sensor, will also be discussed in following subsections with great details. For all the PA tests presented in this chapter, the displacement sensor readings are not fed back into the function generators and the control loop stays open.

3.1.1 Piezo Driver

There are generally two ways of driving PAs: voltage-driven or charge-driven [79, 80]. Using a voltage amplifier to drive PAs is an easy, standard and widely adopted driving method. The operating range and bandwidth of PAs are maintained, yet the voltage-driven PA outputs are impacted by the hysteresis nonlinearity [80]. Without including any hysteresis compensator like Prandtl-Ishlinskii operators, the hysteresis nonlinearity is found to be much reduced in PAs driven by charge amplifiers, which means the PA displacements change almost linearly with the amount of charge stored in their piezoceramic [64, 78, 79, 80, 81]. In reality, the charge-driven method has not been widely adopted due to the limitations in charge amplifiers. Even though a charge amplifier shares similar working principles with a voltage amplifier, the uncontrolled nature of output voltage in charge amplifiers quickly saturate to power rail voltage and distort output signals [82]. Compared to the extensive choices of voltage amplifiers in the market, there is hardly any off-the-shelf charge-amplifier at the kilowatts level. For implementing a charge control with a current-output amplifier, an expensive MHz-range current probe like Tektronix-TCPA300 [83] is needed to compute real-time charge values in the PA.

A hybrid solution that combines the benefits of charge-driven operations with a voltage-

output power amplifier is named the capacitor insertion method [79, 80], which means a fixed-capacitance capacitor is connected in series with the PA. As a "charge sensor" by nature, the voltage over this additional capacitor indicates the charge flow through the PA according to $V_c = C * q$. And the hysteresis and creep nonlinearities almost disappear in actuator displacement [84, 78, 79, 80]. As a negative effect, the inserted capacitor reduces the voltage drop over the PA, and limits the bandwidth of response by increasing the time constant of the overall system [84]. And the capacitance of this inserted capacitor must be precisely determined anytime to ensure the accuracy of driving signals. For switching operations in PA-FMS, the bandwidth of response must be preserved to achieve fast enough actuations. Meanwhile, the PPA40L or PPA120XL actuator needs a peak voltage of 150 V for full-range displacements. Therefore, given that the capacitor insertion method is a promising solution for better control accuracy in PAs, it is not adopted in this study.

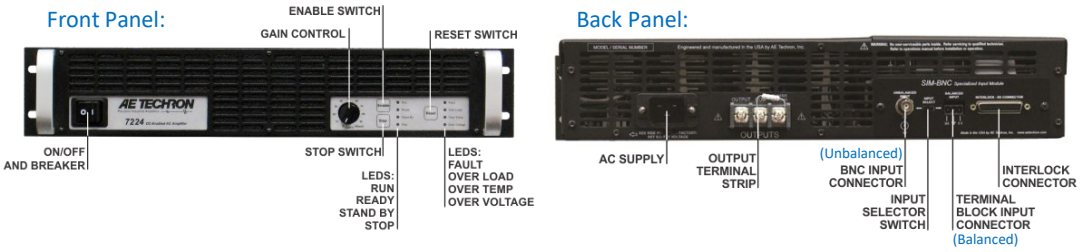

Figure 3.2: Piezo driver: AE Techron® 7224 power amplifier [85].

The selected piezo driver in this study is the model 7224 power amplifier manufactured by AE Techron®(Figure 3.2). It is a linear, four-quadrant amplifier with DC to 300 kHz bandwidth, and it can work in either voltage mode (max amplification ratio K_{amp}: 20 V/V) or current mode (max transconductance ratio: 5 A/V). The factory demo of 7224 model provides a first-quadrant peak source current of 40 A and a third-quadrant peak sink current around 25 A at 150 V voltage output (see details in Chapter 7). This piezo driver can output a 6 kW of peak power output, given that its rated continuous power output is only 900 W. The combination of 300 kHz bandwidth and 6 kW power output in this power amplifier

significantly surpasses other commercial piezo drivers in the market, although this 7224 model has not been optimized for PA driving purposes. Besides all these advantages, the limitations of using this power amplifier to drive the larger actuator, PPA120XL, in the proposed SCF-insulated PA-FMS will be discussed in Chapter 7.

The equations used to estimate the average power output from piezo driver and the average current following through PA during actuations are given below. Here the actuator is simplified into a pure capacitance C_{piezo} (Table 2.4) to be charged and discharged with a switching time t_{sw}:

$$P_{driver,avg} = \frac{1}{2} C_{piezo} V_{piezo}^2 / t_{sw} \tag{3.1}$$

$$I_{driver,avg} = \frac{1}{2} \frac{C_{piezo} V_{piezo}^2}{t_{sw} V_{piezo}} \tag{3.2}$$

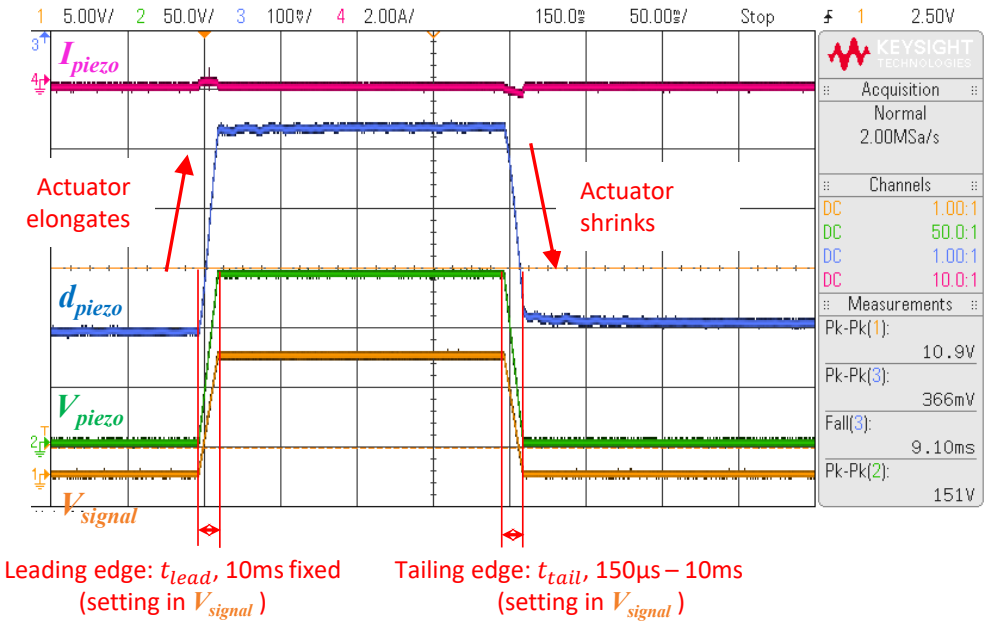

Figure 3.3: Experimental waveform of open-loop PPA40L actuation when a 415 g load m_{load} was carried by the PA. The function generator output V_{signal} had a lead time t_{lead} of 10 ms and a tail time t_{tail} of 10 ms.

During open-loop tests, the input signal of piezo driver came from a function generator Tektronix® AFG3022B through the unbalanced BNC input connector on the rear panel of power amplifier in Figure 3.2. As shown in Figure 3.3, the high bandwidth of piezo driver allowed its output voltage V_{in} following its input V_{signal}, so that the t_{lead} was also the lead time in piezo driver output V_{in} from 0 V to 150 V, and the t_{tail} was also the tail time in piezo driver output V_{in} from 150 V to 0 V. In order to avoid excessive accelerations in piezoceramic during the actuator elongation process, the leading edge was kept constant at 10 ms during open-loop tests. The tail time was selected between 150 μs and 10 ms to evaluate PA travel curves under fast and slow actuations comprehensively.

This dissertation focuses on the tail edges of driving signals to study PA-FMS switching-off process through experiments. Referring to Figure 2.8, the moving contacts were separated from stationary contacts when the actuator shrunk under a falling driving voltage V_{piezo}. To the opposite, a rising edge in V_{piezo} made the actuator elongated and pushed the moving contacts upwards to reconnect with the stationary contacts. In this way, the current conduction circuit through the PA-FMS was reclosed.

3.1.2 Displacement Sensor

The travel curve of PPA40L actuator d_{piezo} shown in Figure 3.3 was obtained with an eddy current displacement sensor system (ECL101-U5-SAM-3.0) manufactured by Lion Precision®. Eddy current sensor is a kind of non-contact displacement sensor that uses an alternating magnetic field to sense distance from the sensor probe to the target [86]. The sensing starts with an alternating current flowing through the sensing coil within sensor probe (Figure 3.4(a)) which triggers an alternating magnetic field in space (Figure 3.4(b)). On the side of conductive target (i.e., copper targets), an eddy current is induced in the opposite direction of the original field from the sensing coil, which then changes the mutual impedance collected by the sensing coil. As the amount of impedance change depends on the distance between sensor probe and target, the position of the target relative to the probe

is thus obtained [86].

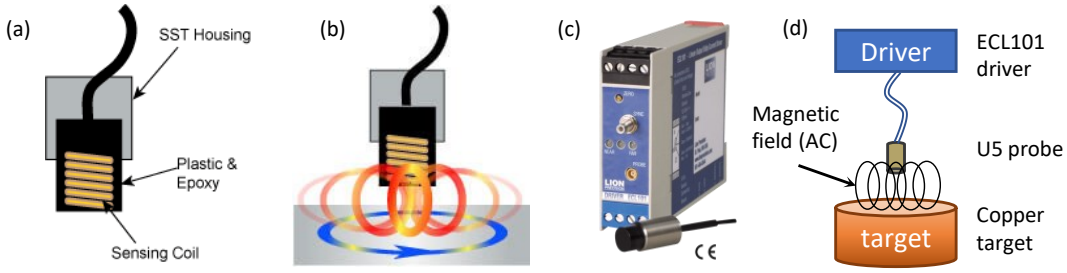

Figure 3.4: Eddy current displacement sensor used in tests. (a) Probe construction, (b) working principle, (c) ECL driver with eddy current sensor probe, (d) experimental setup [86].

The open-loop tests use an ECL101 sensor driver along with a U5 probe provided by Lion Precision®. The U5 probe has a sensing range of 1 mm and needs a minimum target diameter of 15 mm. The ECL101 sensor driver (Figure 3.4(c)) equipped with a U5 probe has a typical resolution of 0.008% (83.54 nm), a linearity of 0.05% (0.5 μm, linearity error 0.18%), and a mid-range thermal drift of +/- 0.04 %FS/°C. The experimental setup of ECL101 sensor driver with probe is shown in Figure 3.4(d), here the target material keeps being copper with at least 0.2 mm thickness. With an average sensitivity of 8 mV/μm, the displacement of the actuator can be calculated from the eddy current sensor output voltage as:

$$d_{piezo}\,[\mu m] = \Delta x\,[\mu m] = \frac{\Delta V_{sensor,out}\,[mV]}{8\,[mV/\mu m]} \tag{3.3}$$

The selection of eddy current sensor as the displacement sensor is a trade-off among resolution, bandwidth, mounting effort and cost. The reasons for not choosing capacitive sensors, which use electric fields to sense distance, mainly come from their low bandwidth and intolerance to target surface contamination - a fingerprint on target may change the readings of capacitive sensors [86]. Other choices of displacement sensors in literature, such as laser Doppler vibrometers (a.k.a. laser interferometers) with nm-level resolution

and MHz-range bandwidth [60, 66, 87], at the same time, the only downside point is their high cost.

The noise level of this eddy current sensor output is directly dependent on the noise level of power supply, and a ripple less than 40 mV peak-to-peak is required in the input voltage of sensor driver. Compared to AC/DC switched-mode power supplies that commonly bring a switching ripply above 40 mV, using a 12 - 20 V battery is a better choice as found experimentally for its almost-zero ripple level. In this study, a 20 V, 3 Ah rechargeable battery has been chosen to supply the 2 W power for the displacement sensor operation.

3.2 Experimental Setup for Open-loop Actuation

The experimental setup for model parameter identification tests is shown in Figure 3.5(a). The output of the function generator (Tektronix® AFG3022B) was fed into the unbalanced BNC input connector of power amplifier (AE Techron® 7224). On the output side of the power amplifier, a thick-film resistor of 1 Ω (MP930 - 1.00 - 1%, 30 W) with a low inductance feature was connected in series with PPA40L actuator as a damping resistor. The PPA40L actuator was connected into the power circuit with the red lead connected to the damping resistor, and the black lead connected to the negative output terminal of power amplifier. Any reverse in voltage polarity will bring severe mechanical damage to piezoceramic. The PPA40L actuator carried a 3 g copper shim as the target for eddy current sensor in Figure 3.5 because the actuator's top surface was not flat. The other reason for using the copper shim was that PA prestressing frame was made of ferrous stainless steel, but the eddy current sensor was calibrated with non-ferrous metal like aluminum and copper. This 3 g copper shim was replaced with a 230 g copper weight or a 415 g copper weight for testing with heavy payload in further PA tests.

On the sensing side, a current probe (Keysight® 1146B, DC to 100 kHz) was hooked around the wire from actuator black-pin to amplifier negative output, that is, the ground wire of power circuit. The waveforms of output voltage of function generator V_{signal}, volt-

age over PPA40L actuator V_{piezo}, voltage output of eddy current sensor $V_{sensor,out}$, and the current sensor output I_{piezo} were fed into the oscilloscope for data collection. The displacement of load/copper shim on the top of actuator was then calculated by Equation 3.3.

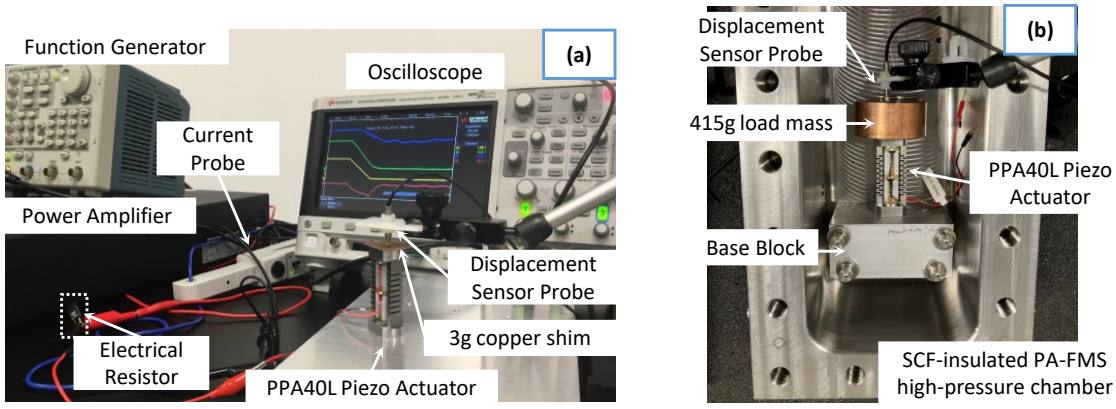

Figure 3.5: Experimental setup of open-loop actuations with PPA40L actuator. (a) is the full-view photo for model parameter identification tests; (b) is the improved setup for open-loop travel curves with minimized externally-introduced oscillations.

Figure 3.5(b) gives a close-up view to the mechanical fixture of PPA40L actuator during open-loop actuation tests. It has been observed experimentally that the PPA40L actuator could transfer impulse movements to its mounting block during actuation. The measured positions at actuator top side were disturbed by the low-frequency oscillations in the base block. In order to minimize this external disturbance, the base block of actuator was bolted onto a high-pressure chamber with over 25 kg in weight as shown in Figure 3.5(b). This high-pressure chamber is the same one to be used for the SCF-insulated PA-FMS prototype (Figure 2.8).

Also, in Figure 3.5(b), the top side of PPA40L actuator was connected with a 415 g copper weight, which was equivalent to the total weight of contacts, contact plate and insulating connectors to be carried by the PPA120XL actuator in the SCF-insulated PA-FMS prototype. Because PPA120XL actuator is an enhanced version of PPA40L actuator, once the developed controller strategy can make the PPA40L actuate the same load mass with PPA120XL under similar switching conditions, it is safe to migrate the developed

control strategy to PPA120XL actuations.

3.3 Open-loop Travel Curves of PPA40L Actuator

The open-loop travel curves measured with components in Figure 3.5(a) and mechanical fixture in Figure 3.5(b) are shown in Figure 3.6. Here a matrix of oscilloscope waveforms are provided to demonstrate how the PPA40L behaved under different tail time in functional generator signals t_{tail} and different load masses m_{load}, with an open-loop voltage-input control. The four curves in scopes corresponded to $I_{piezo}, V_{disp,sensor,out}, V_{piezo}, V_{signal}$ respectively, and the travel curves d_{piezo} of PPA40L actuator were calculated out of measured traces $V_{disp,sensor,out}$ according to equation 3.3.

As shown in Figure 3.6, the most ideal travel curve from PPA40L actuator was obtained with $t_{tail} = 1\ ms$ & $m_{load} = 3$ g, which was the slowest switching motion with the lightest load among 12 combinations. And the most oscillatory travel curve was obtained with $t_{tail} = 150\ \mu$s & $m_{load} = 415$ g, which was the fastest switching motion with the heaviest load mass. Both a smaller t_{tail} and a larger m_{load} increased the vibration, but their influences were reflected differently. On the one hand, when keeping the same m_{load}, a higher t_{tail} boosted the high-frequency oscillations immediately after the falling edge, but the frequency and magnitude of subsequent low-amplitude oscillations stayed unchanged. On the other hand, when keeping the same t_{tail}, a higher m_{load} expanded the time period of subsequent low-amplitude oscillations, but the changes in high-frequency oscillations were not significant.

The two parts of vibration are clearly labeled in Figure 3.7. The high-frequency, large-magnitude part of vibration immediately following the switching is caused by the PA internal vibration nonlinearity. Discussions on the actuator model in following subsections will give more information on this high-frequency vibration. After the internally-originated vibration gradually faded out, the remaining low-frequency, small-magnitude oscillations were externally-introduced oscillations from non-stable mechanical fixtures.

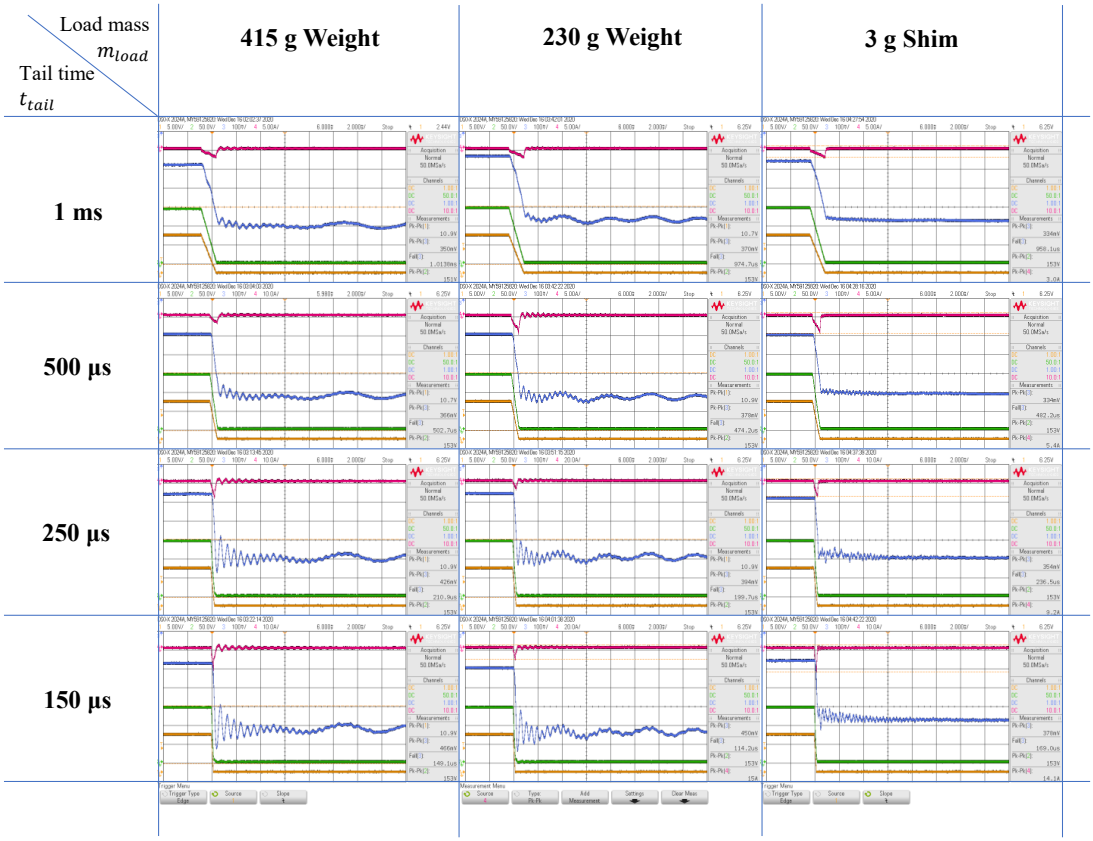

Curve Legend:

- Pink - I_{piezo}, actuator driving current, 5/10/20 A/div
- Blue - $V_{disp,sensor,out}$, displacement sensor output/actuator displacement, 100 mV/div is equivalent to 12.5 µm/div for travel curve d_{piezo}
- Green - V_{piezo}, actuator driving voltage, 50 V/div
- Yellow - V_{signal}, driver input signal, 5 V/div

Figure 3.6: Experimental waveforms of travel curves d_{piezo}, actuator driving voltage V_{piezo} and current I_{piezo} under different tail time t_{tail} in power amplifier input signal V_{signal} and different load mass.

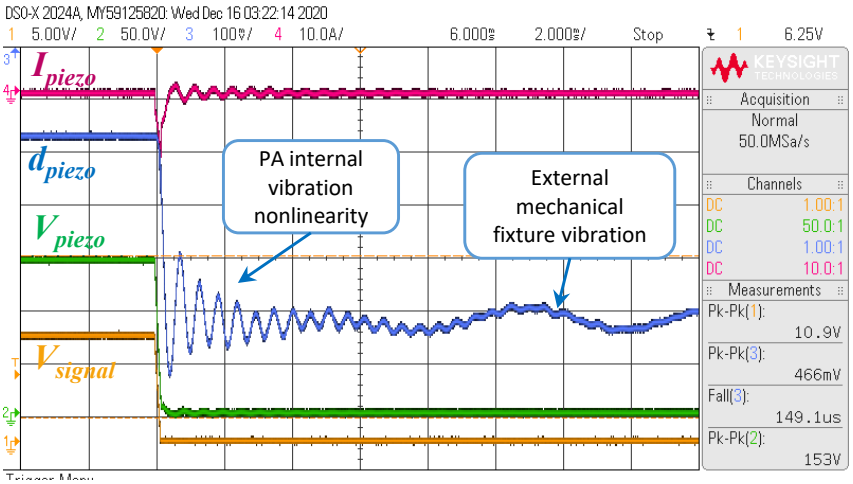

Figure 3.7: Experimentally measured vibration from PPA40L actuator travel curves under $t_{tail} = 150\ \mu$s & $m_{load} = 415$ g conditions.

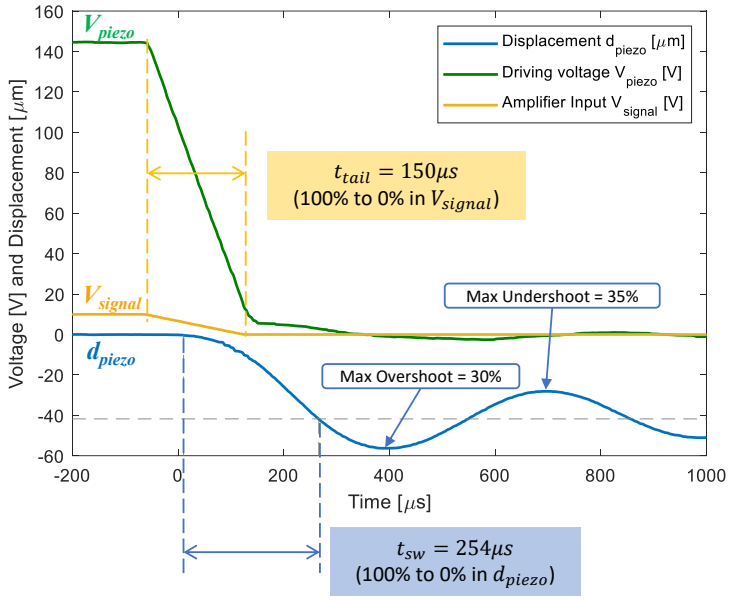

Figure 3.8: Illustrations of definitions on tail time t_{tail} in V_{signal}, switching time t_{sw} in d_{piezo}, overshoot and undershoot in open-loop travel curves.

Because changing different mechanical fixtures in test setup changed low-frequency, small-magnitude vibration during tests, such as from a heat sink in Figure 3.5(a) to the base block and high-pressure chamber in Figure 3.5(b). For consistency of comparisons, all the open-loop actuation data presented in Figure 3.6 were measured in consecutive tests without changing the mechanical fixture. Thus, the variations of externally-introduced vibration were mainly consequences of changed load mass.

The zoom-in view of internally-originated vibration nonlinearity in Figure 3.8 gives details of tail time t_{tail}, switching time t_{sw}, overshoot and undershoot. The tail time t_{tail} referred to the time duration between the averaged high voltage in V_{signal} and the averaged low voltage in V_{signal} as defined above. The t_{tail} was the time characteristic on the input voltage side of PA system, then a time characteristic on the output displacement side of PA system was called as t_{sw}. The switching time t_{sw} was defined as the time duration between the averaged high position (100% travel) to the averaged low position (0% travel) in PA displacement x_{piezo}.

It is noteworthy to point out, the t_{sw} obtained under $t_{tail} = 150$ μs & $m_{load} = 415$ g loading conditions barely touched the 250 μs target, although the t_{tail} in amplifier input signal already reduced down to 150 μs. Any further reduction in t_{tail} below 150 μs had a minimal effect on t_{sw}, because the oscillatory shape of vibration had dominated switching travel curves in these heavy load scenarios. Moreover, the internally-originated vibration brought over 30% overshoot and undershoot in this travel curve. In PA-FMS applications, a 35% undershoot in actuator travel curve means a 35% reduction in contact separation distance, which brings an approximate 35% reduction in the insulation voltage of PA-FMS and the PA-FMS was thus more susceptible to erroneous electrical breakdown. Due to the above reasons, a small overshoot and undershoot range of $<$10% has been promised in Table 2.5 to avoid insulation failures in PA-FMS. In short, the internally-originated vibration must be properly damped to achieve a shorter switching time with reduced overshoot and undershoot in PA travel curves.

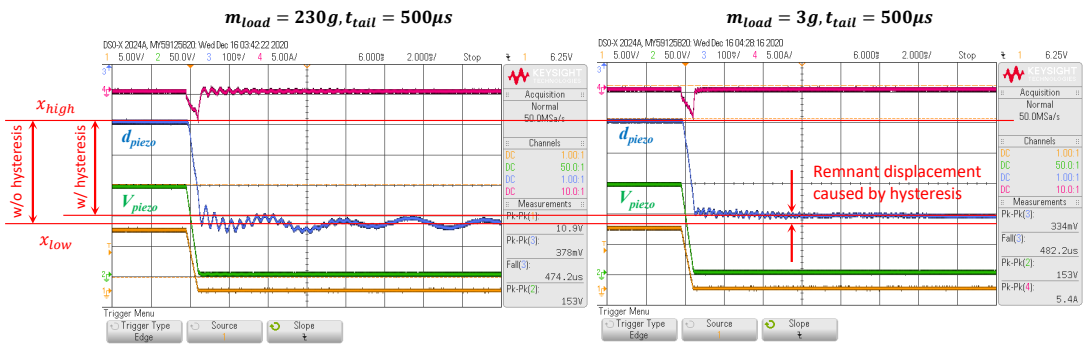

Figure 3.9: Experimental waveforms showing the hysteresis in switching motion travel curves was reduced by the subsequent vibrational movements in the PA.

Figure 3.9 illustrates how the hysteresis effect became less pronounced in switching operations with a high volume of vibration, which was another interesting point observed from experimental open-loop travel curves. The total actuator travel in $t_{tail} = 500$ μs & $m_{load} = 230$ g case on the left was slightly higher than the travel in $t_{tail} = 500$ μs & $m_{load} = 3$ g case on the right, although both cases shared exactly the same driving voltage V_{piezo}. The hysteresis nonlinearity caused this reduced displacement under the same driving voltage, and this effect became obvious mainly under $m_{load} = 3$ g scenarios when the travel curves were free of vibration around zero voltage. In a sense, the existence of vibration helped reduce the hysteresis in travel curves. Considering the electromechanical coupling nature of PAs, the bipolar mechanical movements of piezoceramic during vibration might induce additional charges due to the direct piezoelectric effect. These induced charges counteracted the remnant charges that could have caused hysteresis in PAs travel curves. In $m_{load} = 3$ g setup where the forced vibration from heavy load mass was missing, the piezoceramic had no additional charges to counteract the remnant charges and the hysteresis nonlinearity became more obvious.

3.4 Model Parameter Identification

In this subsection, a comprehensive dynamic model is constructed with time-invariant model parameters. The assumptions of time-invariant model parameters are based on the following aspects. Firstly, the PA operates within the datasheet-defined voltage range of -20 V to 150 V (2.4), and the datasheet-given specifications are good references for PA model parameters. Secondly, the degradation of PA performance over time is neglected in this study exploring the limit of piezoelectric actuation in the PA-FMS scenario. Thirdly, the manufacturer data of piezoceramic material of PPA40L actuator and PPA120XL actuator is unavailable to the public, which makes the estimations of nonlinear model parameters very difficult.

3.4.1 Electromechanical Model

Figure 3.10 shows the comprehensive dynamic model to be used for PA controller designs. This model has the electrical domain as the system input (V_{in}) and the mechanical domain as the system output (x), according to the energy conversion flow in PAs. The time-domain state equations corresponding to this revised model are also given in Figure 3.10. The parameters used in state equations will be determined in the next subsection.

3.4.2 PPA40L Actuator Model Parameter Identification

Electrical Parameters

From the electrical domain, the driving voltage of actuator V_{in} is an externally-controllable parameter. From the experimental perspective, V_{in} is the output voltage from the power amplifier being the piezo driver. The piezo driver sources or sinks the input current I_{in} that flows through a damping resistor R_{damp} and the actuator, and this I_{in} was measured as I_{piezo} curves in open-loop scope waveforms in Figure 3.6. This electrical damping resistor can damp the harmful nanoseconds-duration voltage spikes by increasing the electrical time

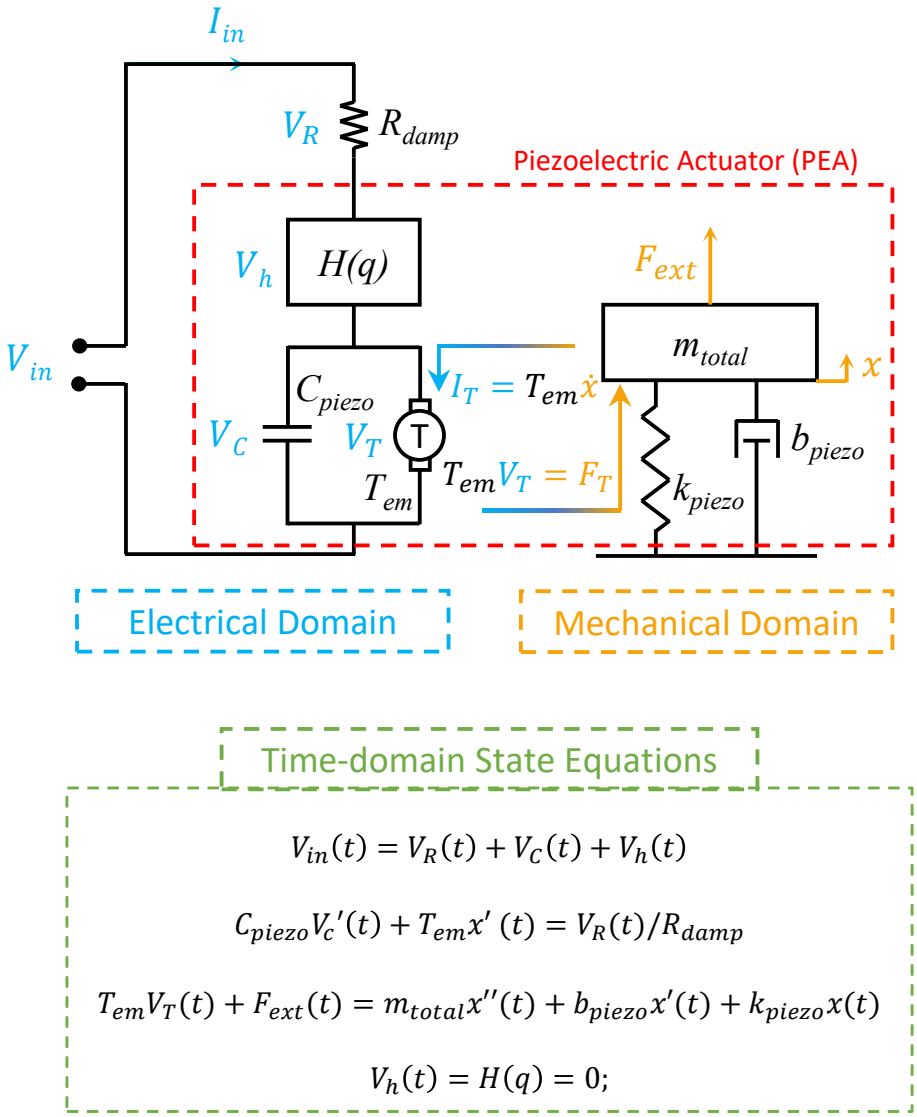

Figure 3.10: Proposed electromechanical model for both PPA40L and PPA120XL actuators. The time-domain state equations of PA systems are also provided.

constant of $R_{damp} - C_{piezo}$ circuit, so that the actuator is protected from crack-inducing acceleration and deceleration during switching processes.

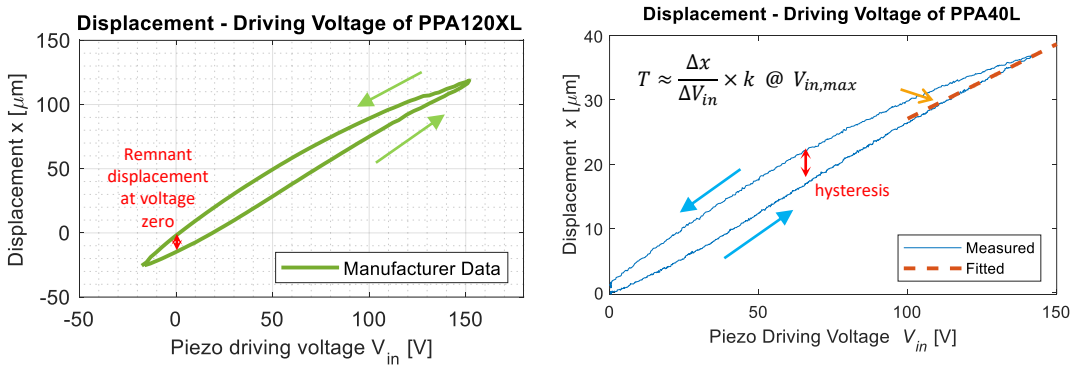

Figure 3.11: Measured hysteresis in PPA120XL and PPA40L actuators.

The lumped electrical parameters of the PA include a hysteresis component $V_h/H(q)$, an equivalent capacitance of actuator C_{piezo}, and an electromechanical transformation ratio T_{em}. The hysteresis voltage V_h is generally a nonlinear function of stored charge in piezo-ceramic q, but the numerical equations may vary. There have been countless hysteresis models being proposed to describe this memory-based nonlinearity, which can be divided into physics-based models and phenomenological models [13]. As the hysteresis effect makes actual displacement outputs delayed from voltage inputs as shown in Figure 3.11, the counteraction of hysteresis effects is a popular topic in high-precision motion control of nanopositioning stages. To the contrary, for PA-FMS applications, the open-loop travel curves shown in Figure 3.9 indicate that the hysteresis effect could be partially eliminated by the subsequent vibration after switching motions. And vibration studies in PAs usually neglect hysteresis in their discussions [13, 64]. Consequently, the hysteresis compensation is assigned lower importance in switching motion controller design used in PA-FMS application.

The equivalent capacitance of actuator C_{piezo} is usually given in actuator datasheet. It can be more precisely determined from the impedance sweep graph with an LCR meter as shown in Figure 3.12. Comparatively, the capacitance given in PPA40L datasheet is

8.8 μF [56], and the measured capacitance at 20 Hz to 2 kHz with the 419 g load mass is about 9.6 μF as shown in Figure 3.12(d). Thus the 9.6 μF of capacitance will be used in simulations of PPA40L actuator.

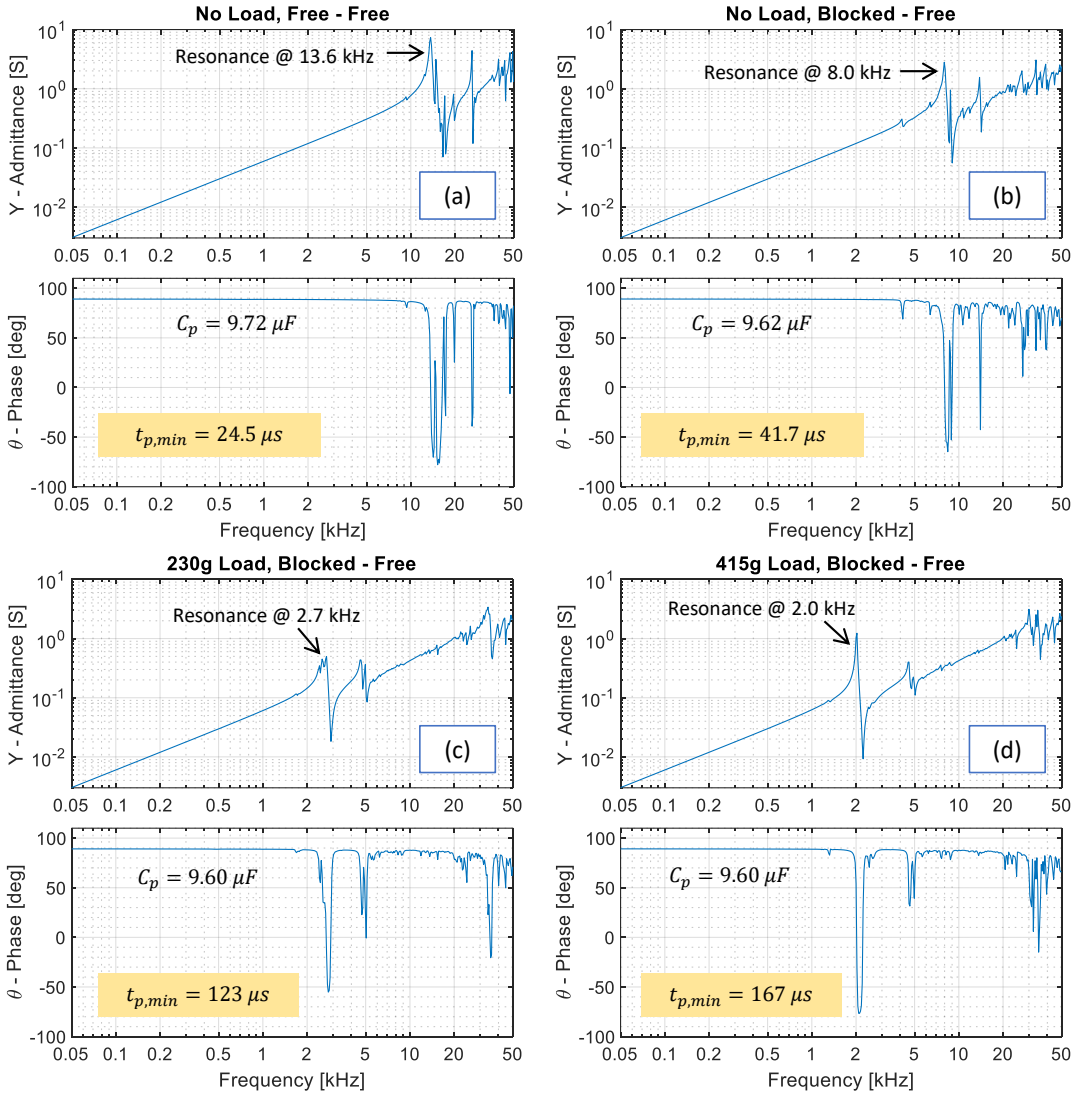

Figure 3.12: Measured impedance sweep of PPA40L actuator in admittance-phase $Y - \theta_Y$ mode with (a) no load, free-free installation, (b) no load, blocked-free installation, (c) 230 g load, blocked-free installation and (d) 415 g load, blocked-free installation.

The measured impedance curves in Figure 3.12 also give the actual resonance frequencies f_{res} under different loading conditions. According to 2.10, the fastest displacement time $t_{p,min}$ under these loading conditions can thus be estimated with f_{res}. With one end

Table 3.1: Expressions of electromechanical transformation constant T_{em} in literature.

Reference	**Equation**	**Parameters**
Goldfarb [61]	$T_{em} = \sqrt{C_{piezo}(C_{pol} - k_{piezo})}$	C_{piezo} - capacitance; c_{pol} - open-lead stiffness; k_{piezo} - stiffness
Juhasz [88]	$T_{em} = \frac{\Delta x_n}{\Delta V_{p,n}} k_{piezo}$	x_n - displacement at max driving voltage; $V_{p,n}$ - max driving voltage; k_{piezo} - stiffness
Quant [77]	$T_{em} = \frac{w_p d_{31}}{\varepsilon_0 K_3^T}$; (for bimorph actuators)	w_p - actuator width; d_{31} - piezoelectric strain constant, 31 direction; $\varepsilon_0 = 8.85e-12$ [C/(Vm)]; K_3^T - relative dielectric constant

fixed and the other end loaded with 415 g mass, the minimum displacement time of this PPA40L actuator increases to 167 μs from the 24.5 μs in a no-load, free-free installation. Considering this 167 μs displacement time is so close to our targeted 250 μs time, the PPA40L actuator is thus indeed pushed to its limit of driving capability in this study.

Electromechanical Transformation Ratio T_{em}

The electromechanical transformation ratio T_{em} is the most critical parameter within the model because it represents the inverse piezoelectric effect that links electric input to mechanical output within a PA. As shown in Figure 3.10, a motor-like symbol hosts this T_{em} parameter with a voltage drop V_T and flowing current I_T in the electrical domain of PA model. The transformation voltage V_T is a multiplier of the transformed force F_T in the mechanical domain with a coefficient T_{em}, showing the energy transfer from the electrical domain to the mechanical domain. At the same time, the transformed current I_T is the product of mechanical velocity x' multiplied by the coefficient T_{em}, showing the direct piezoelectric effect from the mechanical domain to the electrical domain in PAs.

Although the T_{em} is an important parameter representing the electromechanical conversions inside PAs, its analytic expression is not explicit and deterministic. So far, there are at

least three ways proposed in literature to obtain T_{em} value with theoretical and experimental parameters, and their respective expressions are shown in Table 3.1. The T_{em} expression given by Goldfarb and Celanovic has a specific parameter, the open-lead stiffness c_{pol}, that could only be determined after dissembling the piezoceramic stack from its stainless steel housing [61, 88], thus this method is not feasible in this study. Juhasz *et al.* proposed a more approachable determination method of T_{em} in [88], assuming the slope of hysteresis voltage $V_h = H(q)$ became zero around the maximum driving voltage range in actuator loading curve (displacement - driving voltage in Figure 3.11). Because the parameters in Jusasz's method can be determined experimentally, this T_{em} expression has been chosen in this study. There is a third T_{em} expression proposed for piezoelectric bimorph actuator by Quant [77], but this method is not chosen here due to the lack of accurate data about piezoceramic material in the PPA40L actuator.

The experimental determination of T_{em} in PPA40L actuator followed the instructions in [88] and [89]. Any remnant hysteresis in PPA40L actuator was first cleaned up by applying unipolar sine signal and linearly decreasing amplitude ($V_{in} = 0.83exp(-0.45t)sin(4t)$). The loading curve shown in Figure 3.11(b) was measured after the application of linearly rising voltage of 0 - 150 V within 10 s. The slope at the end of expansion process in the loading curve, $\Delta x_n/\Delta V_{p,n}$, was thus obtained by curve fitting. With the stiffness of PPA40L provided in its datasheet, the T_{em} was determined around 25.5 N/V.

Mechanical parameters

Assuming linearity in its operation region, the PA behaves like a mass-spring-damper system with time-invariant parameters in its mechanical domain.

The mass m_{total} is the total weight of actuator, copper weight, plus a part of mechanical fixture as it is also shaken by the PA during actuations. The spring constant, also called stiffness or k_{piezo}, is a constant number provided in actuator datasheet. The damper coefficient, b_{piezo}, is not included in PA datasheet so that it has to be determined through

Table 3.2: Identified model parameters of PPA40L actuator.

Electrical Parameter		**Value**	**Mechanical Parameter**		**Value**
Damping resistor	R_{damp}	1 Ω	Total mass	m_{total}	0.2 - 0.8 kg
Capacitance	C_{piezo}	9.6 μF	Stiffness	k_{piezo}	90 N/μm
Transform ratio	T_{em}	27 N/V	Damping ratio	b_{piezo}	550 Ns/m

curve-fitting [77, 89].

In summary, the identified parameters of PPA40L actuator model are shown in Table 3.2. The accuracy of these parameters will be verified shortly after.

3.4.3 Model Verification

The accuracy of the established PPA40L model can be verified with measured open-loop travel curves in Figure 3.6. For the simulations in MATLAB, the state equations given in Figure 3.10 are rewritten in differential equation format as Equation 3.4. Then the simulation-experiment crosscheck is performed by using the measured amplifier output voltage from open-loop tests as the input voltage V_{in} in Equation 3.4, and using the time step of oscilloscope recordings from open-loop tests (usually 0.32 μs) as the time step of differential equation solver in MATLAB.

$$\begin{bmatrix} V_c' \\ y' \\ x' \end{bmatrix} = \begin{bmatrix} -1/R_{damp}C_{piezo} & -T_{em}/C_{piezo} & 0 \\ T_{em}/m_{total} & -b_{piezo}/m_{total} & -k_{piezo}/m_{total} \\ 0 & 1 & 0 \end{bmatrix} \begin{bmatrix} V_c \\ y \\ x \end{bmatrix} + \begin{bmatrix} 1/C_{piezo} \\ 0 \\ 0 \end{bmatrix} V_{in} \tag{3.4}$$

The simulated travel curves of PPA40L actuator with experimental references are shown in Figure 3.13. The established PPA40L actuator has successfully captured the falling edge and majority of frequency and magnitude in subsequent vibration. The experimental travel

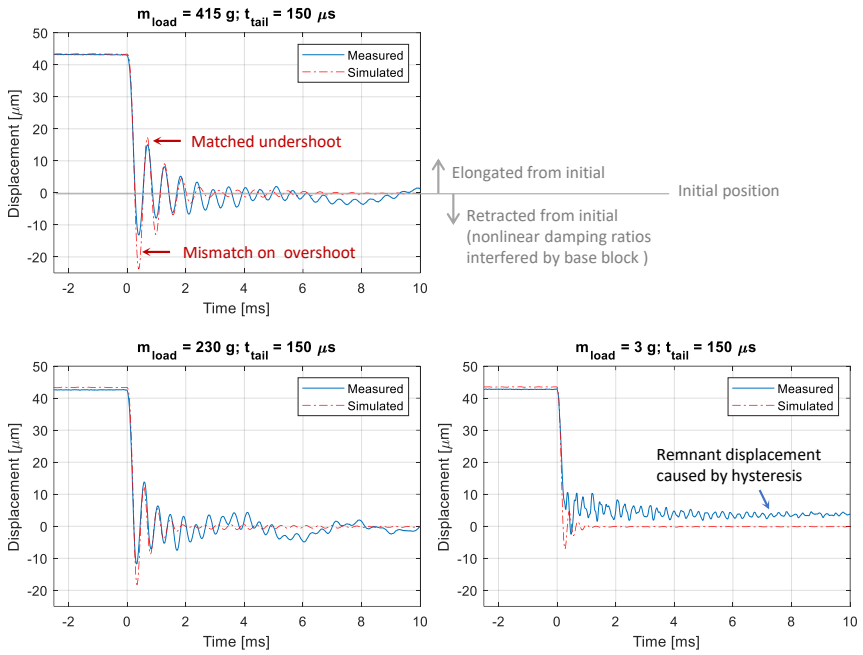

Figure 3.13: Simulated travel curves of PPA40L actuator through electromechanical dynamic model under different load mass and same $t_{tail} = 150\ \mu s$, which are matched with experimental open-loop travel curves.

curves were physically restricted on the overshoot region by the compression constraints in this prestressed PA. As a result, the experimental overshoot was much smaller than the simulated overshoot. The model gives a good estimation in the undershoot region, the region that matters more than the overshoot region with regards to the SCF-insulated PA-FMS prototype.

The part of vibration being represented by the PPA40L model is the high-frequency, large-amplitude vibration immediately following the falling edge of PA movements, so that this part of vibration is named as internally-originated vibration nonlinearity in Figure 3.7. Theoretically, the root cause of this vibration nonlinearity is the second-order, mass-spring-damper system in actuator's mechanical domain as shown in Figure 3.10. When the load mass m_{load} increased from 3 g to 415 g, the amplitude of vibration increased significantly, which followed the expectations in a classical mass-spring-damper system. Therefore, the elimination of this internally-originated vibration can be approached from a theoretical

perspective with established electromechanical model in Figure 3.10.

The low-frequency, small-amplitude part of vibration cannot get reflected in simulations of Figure 3.13. Based on experimental observations, this part of vibration is considered as "externally-introduced" because it could be changed with different mechanical fixtures. As the frequency of the externally-introduced vibration is only hundreds of Hertz, they could be eliminated within a feedback loop using kHz-range sampling frequency in proposed switching motion controllers of PAs.

One more point to notice is that the steady-state error of $t_{tail} = 150$ μs & $m_{load} = 3$ g case in Figure 3.13 comes from hysteresis effect, because the established PA model does not include hysteresis nonlinearity by setting its hysteresis component $V_h = H(q)$ to zero.

3.4.4 Discussions

So far, the identified parameters of the linearized PA model in Table 3.2 are idealized as constants. In reality, the values of these model parameters will change with actuator deformations. For example, the exact capacitance value C_{piezo} varies slightly with actuator length d following $C = \varepsilon A/d$ law. And the variances in capacitance values have been used as the indication signal of capacitance-based self-sensing method [87, 90] to be presented in Chapter 7. Also, the stiffness k_{piezo} may change when the PA deformation changes from elongation to compression. This may explain the experiment-simulation mismatch in the compression region of travel curves in Figure 3.13.

3.5 Chapter Summary

This chapter identifies two types of vibration in open-loop travel curves of PPA40L actuator, and constructs an electromechanical model of PPA40L actuator to be used for controller tuning purposes. The high-frequency, high-amplitude vibration coming right after switching motions was related with the second-order dynamics in the mechanical domain of actuator. And the established PPA40L model with experimentally identified parameters

could replicate the frequency and magnitude of this part of vibration. After the internally-originated vibration died out within several milliseconds, the remnant low-frequency low-amplitude vibration came from non-stable mechanical fixtures in the actuator setup. Considering the different origins and frequency ranges of these two parts of vibration, the proposed switching motion controller in next chapter will include respective strategies to damp the vibration accordingly.

CHAPTER 4
CONTROLLER DESIGN WITH FILTER-BASED ACTIVE VIBRATION DAMPING

In this chapter, several closed-loop switching motion controllers are proposed, tuned and compared for the best vibration damping performance in travel curves of PPA40L actuator. A feedback controller with a proportional-integral controller is configured to eliminate the externally-introduced vibration, and several active damping filters for vibration attenuation are compared to eliminate the internally-originated vibration nonlinearity.

4.1 Vibration Modeling

Vibration damping in piezoelectric actuator studies generally starts with developing a linear vibrational dynamics model out of frequency response on displacement output $X(s)$ and voltage input $V(s)$ in equation 4.1 [13, 14, 52].

$$G_v(s) = \frac{X(s)}{V(s)} = k_0 \frac{\prod(s - 2\pi z_m)}{\prod(s - 2\pi p_n)} \tag{4.1}$$

The calibration process of $G_v(s)$ usually needs a dynamic signal analyzer to obtain the Bode plot (like Figure 2.11). A sinusoidal voltage $V(t)$ with changing frequencies generated by the dynamic signal analyzer will drive the piezoelectric actuator itself without a damping resistor in the loop. Next, the dynamic signal analyzer will receive the actuator position data $x(t)$ from a precision displacement sensor (like a laser interferometer). Without a dynamic signal analyzer, the Bode plot can be constructed manually with $x(t)$ and $V(t)$ data obtained at different sinusoidal frequencies. Unfortunately, the resolution of the eddy current sensor used in the tests limited the precision of obtained $x(t)$ data, so the frequency response of $X(s)/V(s)$ was not obtained. Consequently, the linear vibra-

tional dynamics model of PPA40L actuator $G_{v,PPA}(s)$ used in this study is derived from the PPA40L model shown in Figure 3.10 with identified parameters from Table 3.2:

$$G_{v,PPA}(s) = G(s) = \frac{X_{out}(s)}{V_{in}(s)} = \frac{T}{RCms^3 + (m + RCb)s^2 + (T^2R + b + RCk)s + k} \tag{4.2}$$

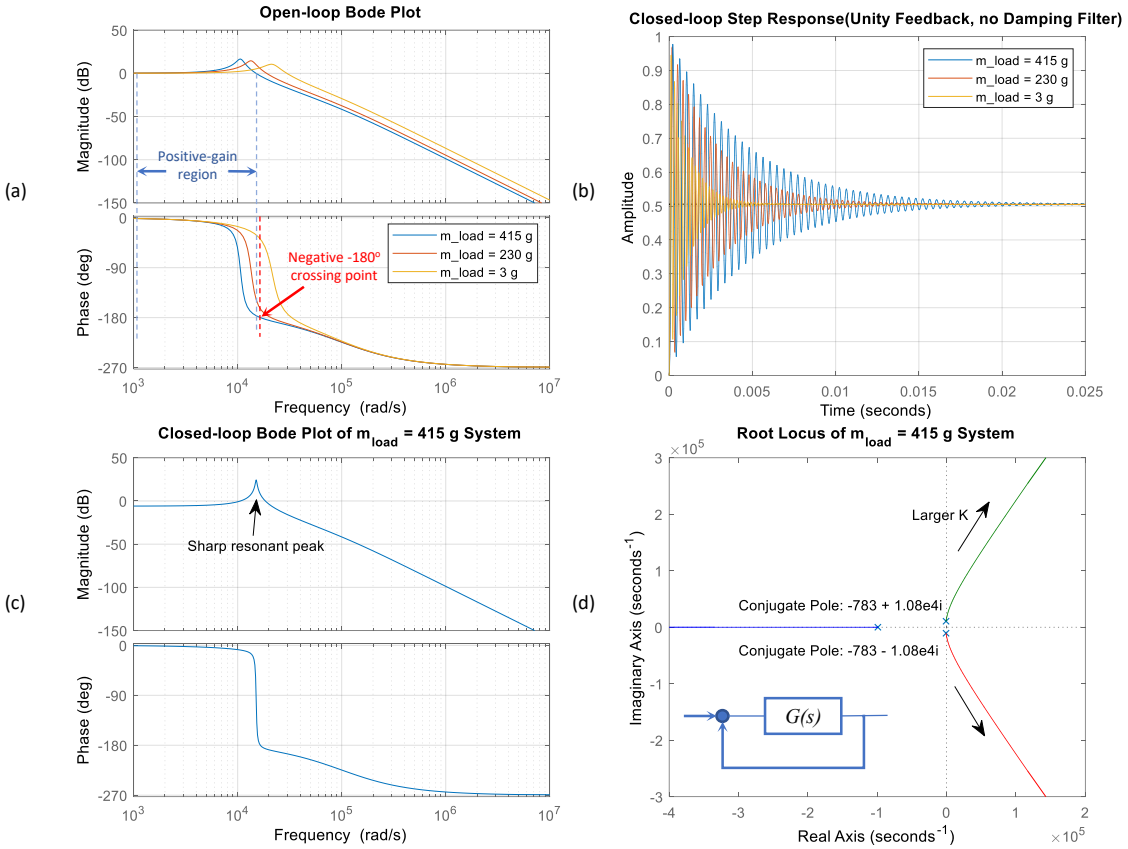

Figure 4.1: (a) Frequency response of open-loop system transfer function $G_{v,PPA40L}(s)$ (abbreviated as $G(s)$ afterwards). And (b) step response, (c) Bode plot, (d) root locus of closed-loop system $G(s)/(1 + G(s))$ with unity feedback but no controller.

The frequency response of open-loop transfer function of PPA40L actuator $G_{v,PPA40L}(s)$, abbreviated as $G(s)$ afterwards, is shown in Figure 4.1(a). The resonant peaks in open-loop magnitude curves are quite obvious, the gain margins are only about 3 dB, and phase margins of stability are merely 3°to 7°as given in Table 4.1. Once the control loop of $G(s)$ gets

Table 4.1: Stability margins and bandwidth of open-loop PPA40L system, without a feedback loop or a damping filter.

Load Mass	**Bandwidth**	**Gain Margin**	**Phase Margin**
m_{load}	BM	$GM@f_{\angle \tilde{G}=180^\circ}$	$PM@f_{\angle \lvert G\rvert=0}$
415 g	2613 Hz	2.97 dB @ 2628 Hz	3.48°@ 2391 Hz
230 g	3298 Hz	3.02 dB @ 3322 Hz	4.50°@ 3018 Hz
3 g	5173 Hz	3.26 dB @ 5254 Hz	7.68°@ 4727 Hz

enclosed with unity feedback, the resonant peak in closed-loop Bode plot of Figure 4.1(c) gets even sharper. The closed-loop step responses are quite poor, as shown in Figure 4.1(b), it will take tens of milliseconds for the internally-originated vibration to settle down, and the converged steady state is only 0.5 with the other 0.5 being the steady-state error. Increasing the feedback proportional gain for accelerating switching speed and lifting up the steady-state value will inevitably destabilize the system, as indicated in root locus of Figure 4.1(d), the poles under higher feedback gain will move to the right half-plane, which will cause the displacement output of actuator to diverge wildly. Therefore, the closed-loop system characteristics must be modified for better switching motion.

There are generally three ways to attenuate vibration in PA actuations: (i) analytical inversion, (ii) input shaping and (iii) damping filter [13]. The first method about inversion-based vibration attenuation is a theoretically complete method that constructs an inverse expression of the vibrational dynamics model. There are four ways of calculating the inversion expression: DC-gain inversion ($G^{-1}(0)$), exact inversion ($G^{-1}(0)$), optimal inversion and periodic inversion [13]. The optimal inversion minimizes an objective function with desired and actual trajectory [67], and the periodic inversion works best for a periodic desired trajectory [64]. However, the intensive calculations of inversion expressions are too complex to be implemented in a real-time controller [91], which is the major problem of using inversion-based compensation in PA-FMS applications. The second method of

input shaping is a general vibration reduction technique built upon knowledge of the natural frequency of the system and the damping ratio [92], so the input signal can be shaped intentionally to a non-linear waveform with components canceling out the external vibrations. For multilayer PAs constructed with individual co-fired stacks like PPA40L actuator and PPA120XL actuator, there is another input shaping method that drives the individual stacks one after another [8], and this input shaping method will be simulated in Chapter 7. Unfortunately, the bandwidth requirement of the piezo driver becomes very high for damping the kHz-level vibration in PA-FMS travel curves using the input shaping method.

Using a notch filter to specifically damp the resonance peak in the $G_v(s)$ is an effective approach that only needs the vibration frequency as the necessary design parameter [13, 14]. The main reason for using damping filters in this study is the minimum computational burdens and system modeling effort. The overall PA controller with a vibration damping filter can thus achieve a very high control update rate, such as 50 kHz or more, to accomplish fast enough controls for a short vibrational process that lasts well below 1 ms.

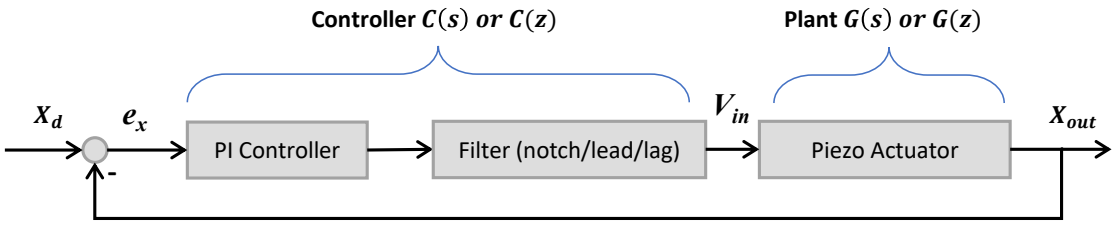

Figure 4.2: Block diagram of closed-loop control system with PI controller, filter and piezoelectric actuator.

A simplified block diagram showing the control system of PPA40L actuator with a proportional-integral (PI) controller, a damping filter, and the control plant of actuation is shown in Figure 4.2. Here a PI controller is chosen for its wide acceptance in industrial applications that helps increase response speed and eliminate steady-state error. The filter used in the control system could be a notch filter as discussed above, it could also be a lead or lag compensator that modifies system performance following the Nyquist stability

criterion. The reasons for including lead-lag compensators into filter selections are given in next subsection.

4.2 Controller Tuning

The proposed switching motion control schemes for PAs will use three kinds of damping filters: notch, lead and lag. Both continuous and discrete transfer functions of these three filters are given in Table A.1, and their tuning principles for optimal vibration-damping performance are constructed in this subsection.

The tuning process of filters is carried out by modifying the open-loop Bode plots of CG, with characteristics of closed-loop step response being the tuning targets. As outlined in Table 2.5, the desired step response should have a rise time around 250 μs, an overshoot/undershoot less than 10%, and a low settling time. Practically speaking, the constraint on overshoot can be slightly loosened in the PPA40L actuator system, because an overshoot in the retraction process (i.e. the piezoceramic stack shrinks to a shorter length than its normal length) actually helps boost the insulation strength of overall PA-FMS.

Technically speaking, the filter tuning in MATLAB is facilitated by the interactive operations in the Control System Designer. The chosen control architecture is given in Figure 4.3, which is the one similar to our closed-loop actuator system after keeping F and H as 1.

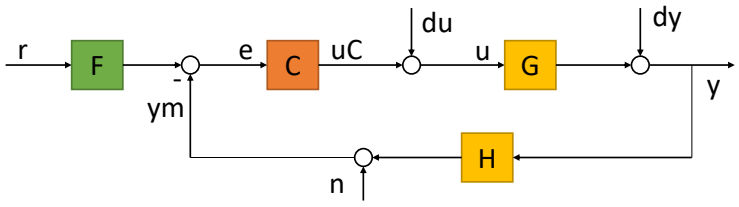

Figure 4.3: Control architecture selected for filter tuning in the Control System Designer of MATLAB. F and H have unity gain in this study.

4.2.1 Strategy 1: PI Controller with a Notch Filter

A digital notch filter $C_{notch}(z)$ used for vibration damping can be expressed as:

$$C_{notch}(z) = K_{notch}\frac{z^2 + a_1 z + a_0}{z^2 + b_1 z + b_0} \tag{4.3}$$

The damping principle of notch filter $C_{notch}(z)$ in the PA switching motion control is illustrated in Figure 4.4. The Bode plot of the open-loop plant $G_d(z)$ has a resonance peak at 1680 Hz in the magnitude plot, which leads to a very tight 3.5° phase margin in the closed-loop system. This dominance of complex conjugate poles has caused excessive oscillations in system step responses before and after closing the unity feedback loop. By putting the stop band of notch filter exactly at the resonant frequency ω_r of $G_d(z)$, the resonant peak is canceled out and a flatter magnitude curve is achieved as shown in Figure 4.4(a).

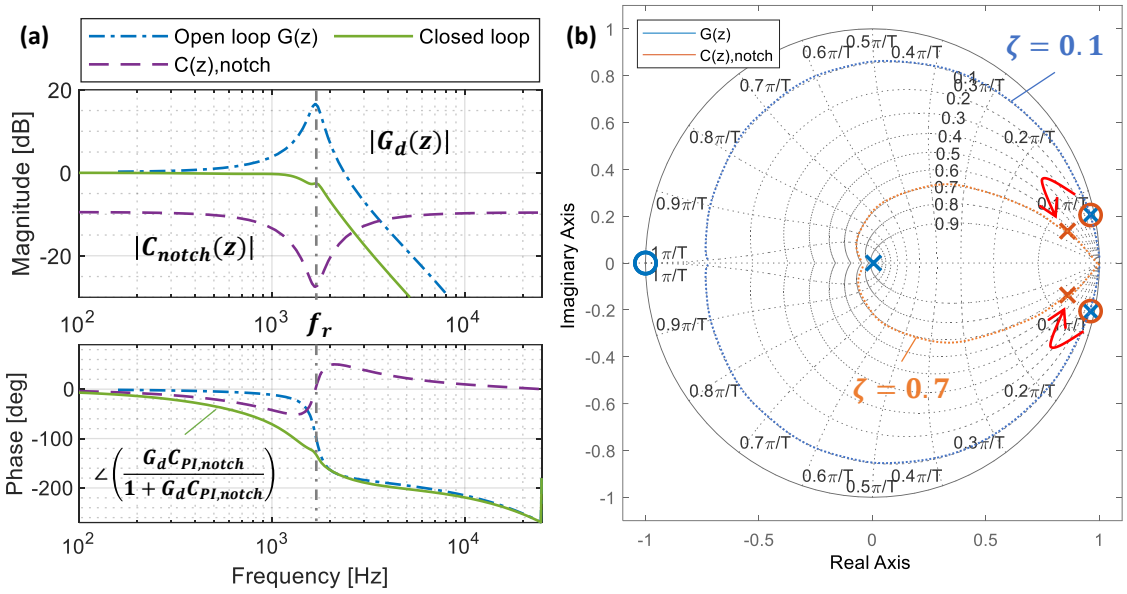

Figure 4.4: (a) Bode plot of the control plant $G_d(z)$, the notch filter $C_{notch}(z)$, and the tuned closed-loop transfer function with PI controller and notch filter; (b) pole-zero map of the control plant $G_d(z)$ and the notch filter $C_{notch}(z)$.

Due to the adjacent -180° crossover frequency to the ω_r region, the notch depth to keep closed-loop stability should meet following relationship about the magnitude of loop

transfer $|C_{notch}(z)G_d(z)|$:

$$20log|C_{notch}(z_r)| + 20log|G_d(z_r)| \leq 0\ [dB] \tag{4.4}$$

The transformation from z-domain to ω-domain is calculated by Tustin approximation:

$$z_r = \frac{1 + j(\omega_r T/2)}{1 - j(\omega_r T/2)} \tag{4.5}$$

The other important parameter of notch filters, the notch width Δ_{notch}, can be estimated by the distance between resonance frequency ω_r and 0dB-crossover ω_{0dB} as in Equation 4.5 to minimize the above-0dB region in the closed-loop magnitude curve.

$$\Delta_{notch} \approx log|\frac{\omega_r + (\omega_{0dB} - \omega_r)}{\omega_r - (\omega_{0dB} - \omega_r)}| \tag{4.6}$$

Besides using notch depth and notch width, the notch filter could also be tuned with damping ratios of poles and zeros in MATLAB. Following the pole-zero cancellation rule, the two zeros of notch filter should overlap the two complex conjugate poles $p_{1,2}$ of $G_d(z)$ that are expressed as:

$$p_{1,2} = e^{-\zeta_r \omega_r T} \angle \pm \omega_r T \tag{4.7}$$

so that the damping ratio of notch zeros is selected as $\zeta_z = \zeta_r$ for pole-zero cancellations.

After canceling out the underdamped poles $p_{1,2}$ of $G_d(z)$, the notch filter introduces two new poles with a higher damping ratio ζ_p that can generate better closed-loop step responses. Different from a second-order system that achieves critical damping at ζ_p = 1, it may not be best solution with ζ_p = 1 for the third-order vibrational dynamic model $G_d(z)$, as it will generate large overshoots in closed-loop step responses from tuning observations. But ζ_p still has its higher bound at ζ_p = 1. The lower bound of ζ_p value depends on the

targeted maximum closed-loop bandwidth according to [11]:

$$\omega_{BW,max} \leq 2\omega_r\zeta_p \tag{4.8}$$

For a targeted maximum closed-loop bandwidth on 2 kHz, the minimum ζ_p of notch filter is 0.6 under f_r=1680 Hz. After balancing the an undershoot below 5% with a rising time below 250 μs, the ζ_p is chosen as 0.65 as shown in Figure 4.4(b).

According to Figure 4.4(a), the tuned closed-loop system with a PI controller and a notch filter has a control bandwidth of 1760 Hz. Considering the original ζ_p in $G_d(z)$ is 0.1, using the notch filter with a ζ_p of 0.65 can boost the theoretical maximum closed-loop control bandwidth by 650% according to Equation 4.8.

4.2.2 Strategy 2 and 3: PI Controller with a Lead Filter or a Lag Filter

From the perspective of loop shaping designs, the notch filter is just one solution specialized in the oscillation attenuation [93]. There are other choices like lead and lag compensators that can improve system responses by adding phase margins around the crossover frequency [93]. Considering a higher phase margin normally corresponds to a more damped step response with reduced oscillations, the lead filter $C_{lead}(z)$ and the lag filter $C_{lag}(z)$ are thus introduced into switching motion controllers in this paper.

A digital form shared by both lead and lag filters is:

$$C_{lead/lag}(z) = K_{lead/lag}\frac{z - z_0}{z - z_p} \tag{4.9}$$

where $z_o > z_p$ for a lead filter, and $z_o < z_p$ for a lag filter. With the same parameters in the PI controller after tuning ($K_{PI} = 1; z_{PI} = -1; p_{PI} = 1$), the switching motion controller cascading $C_{PI}(z)$ with $C_{lead}(z)$ or $C_{lag}(z)$ becomes:

$$C_{PI,lead/lag}(z) = K_{lead/lag}\frac{z+1}{z-1}\frac{z - z_0}{z - z_p} \tag{4.10}$$

The most important consideration when tuning lead/lag filters is to preserve the closed-loop stability. That is, the magnitude of loop transfer needs to be kept below 0 dB around the -180°crossover area. In the phase plot of Figure 4.5(a), after a PI controller adding constant -90°phase to the $G_d(z)$, the crossover frequencies of both lag-filtered and lead-filtered systems drop to the resonance peak frequency ω_r region. On the magnitude plot of Figure 4.5(a), it is obvious that the lead/lag filters do not eliminate the resonance peak of $G_d(z)$, instead, the peak is lowered just beneath the 0 dB borderline at ω_r. The minimum negative magnitude added from the PI controller and lead/lag filter for closed-loop stability is:

$$|C_{PI,leag/lag}(z_r)| = |K_{PI}\frac{z_r+1}{z_r-1}\frac{z_r-z_o}{z_r-z_p}| = |G_d(z_r)|^{-1} \tag{4.11}$$

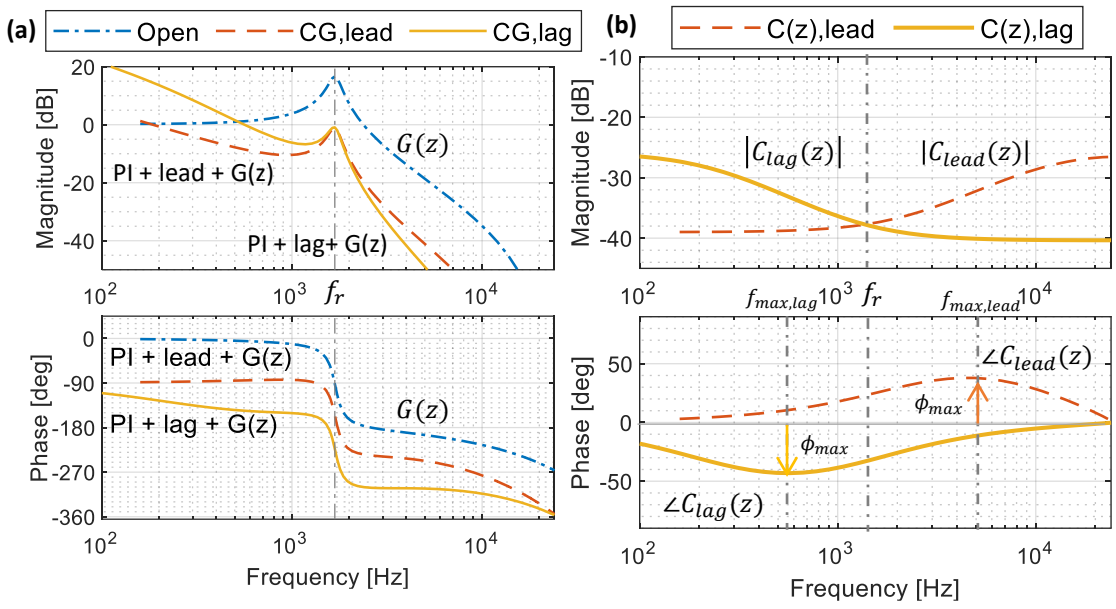

Figure 4.5: Bode plots illustrating (a) the tuned loop transfers $C_{PI,lead}(z)G_d(z)$ and $C_{PI,lag}(z)G_d(z)$ in the forward path of switching motion controllers, and (b) the tuned lead filter $C_{lead}(z)$ and the lag filter $C_{lag}(z)$.

The locations of single pole z_p and single zero z_o in lead and lag filters can be determined through trail-and-fail process with the step response as the reference. They could also be calculated by MATLAB with a desired maximum phase change ϕ_{max} at ω_{max} ac-

cording to following empirical equations:

$$\sqrt{\alpha} = \frac{1}{2} \times tan(45^\circ - \frac{\phi_{max}}{4}) \tag{4.12}$$

$$\omega_{max,lead} = \frac{\omega_r}{\sqrt{\alpha}} \tag{4.13}$$

$$\omega_{max,lag} = \omega_r \sqrt{\alpha} \tag{4.14}$$

where α has its mathematical meaning as the filter parameter in the s-domain expression of lead filter. For the tuned $C_{lag}(z)$ and $C_{lead}(z)$ illustrated in Figure 4.5(b), the ϕ_{max} is selected at 45° in both filters.

Different from the notch filter that only modifies magnitude response near the notch frequency, both lead and lag filters change system responses over the wide frequency range. In the low-frequency range of Figure 4.5(a), the magnitude plot modified by a lead filter hits the -3 dB at a much lower frequency than the plot modified by a lag filter, which leads to a smaller closed-loop bandwidth frequency at just 178 Hz and thus a very slow step response. Comparatively, the closed-loop control bandwidth of the lag-filtered system is slightly higher at 739 Hz, so the step response of lag-filtered system is much faster than the lead-filtered response.

4.2.3 Comparisons on Step Responses

Comparisons on the performance of tuned switching motion controllers in s-domain are illustrated by Bode plots and step responses in Figure 4.6, and the detailed characteristics are provided in Table 4.2. The unity closed loop without any PI controller or filter is provided for reference, so is the closed loop with only a PI controller. The Bode plots shown in Figure 4.6(a)(b) are closed-loop responses from input r to output y, which is 'r2y' in Figure 4.3.

Table 4.2: Bode plots and step responses of the continuous closed-loop actuator system $G(s)$ (415 g load) with a tuned PI controller plus an active damping filter.

Filter	**Bode Plot**		**Step Response**			
Type	Gain Margin	Phase Margin	Rise Time	Overshoot	Undershoot	Settling Time
No PI or filter	3.0 dB @ 2630 Hz	4°@ 2390 Hz	104 μs	95%	88%	17 ms
PI+Notch	6.0 dB @ 1450 Hz	59°@ 685 Hz	245 μs	16%	10%	2.0 ms
PI+Lead	2.1 dB @ 1700 Hz	90°@ 160 Hz	1890 μs	4%	11%	10 ms
PI+Lag	1.9 dB @ 1590 Hz	46°@ 555 Hz	248 μs	25%	12%	10 ms
Only PI	4.1 dB @ 1680 Hz	89°@ 159 Hz	1920 μs	1%	5%	5.5 ms

Due to the fact that the proposed switching motion controllers will be implemented in a digital controller board, the switching motion controllers are also directly tuned in the z-domain with the discretized PA model $G_d(z)$. The tuned z-domain closed-loop systems have their Bode plots shown in Figure 4.7(a) and step responses in Figure 4.7(b).

The switching motion controller with a PI controller and a notch filter gives the best closed-loop step response according to Figure 4.7(b). The rising time is merely 230 μs with a 3% undershoot, and the most useful feature of this critically-damped step response is its minimized settling time around 0.8 ms according to simulations. The switching motion controller with a PI controller and a lag filter is the second best choice, with a 302 μs rising time and a 11% undershoot. Even though the overshoot in the lag-filtered system hits as high as 36%, this large overshoot is not a threatening problem besides prolonging the settling time to 6.4 ms. Because an overshoot in travel curve corresponds to an elongated contact separation distance in the PA-FMS, which may even benefit the insulation strength. Comparatively, the PI controller with a lead filter is too slow to be implemented for an ultrafast switching movement, because of the limited bandwidth brought by the lead filter as analyzed above. Therefore, the lead filter option was not pursued in the hardware implementation tests.

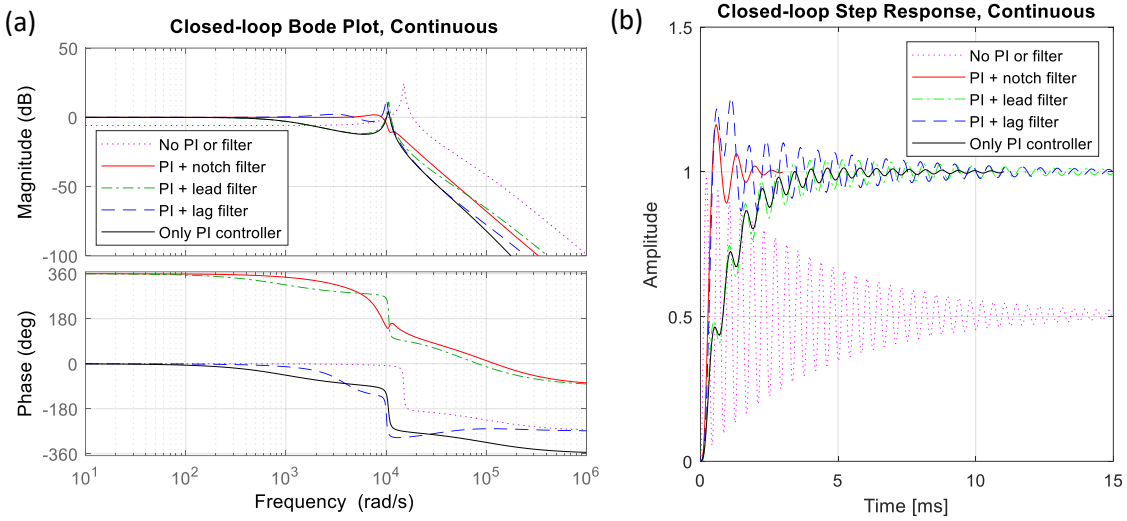

Figure 4.6: Tuned performance of s-domain switching motion control strategies for the $G_d(z)$. The controllers $C(z)$ have a PI controller with a notch, lead, or lag filter.

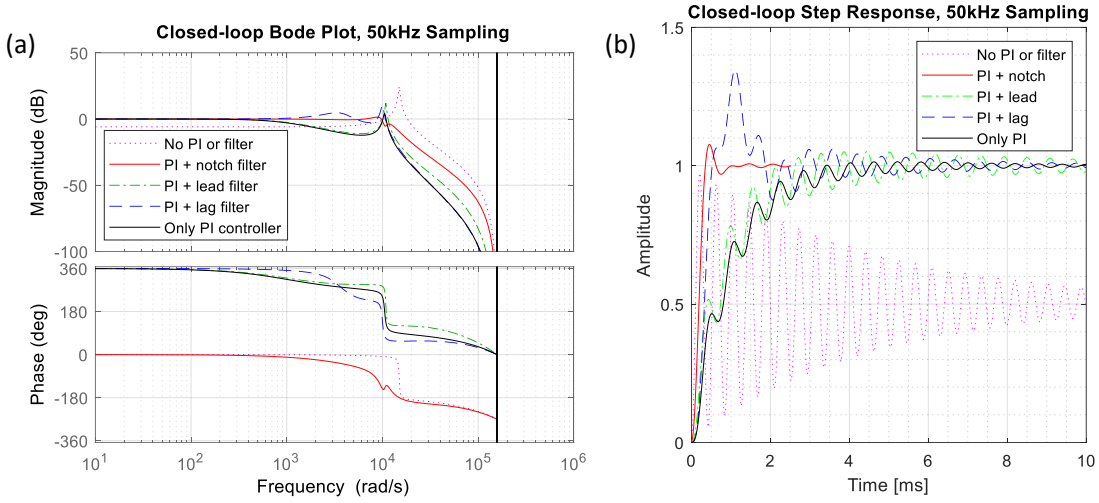

Transfer function of tuned controllers (PI + filter) in 50kHz sampled discrete system:

- PI + notch filter:

$$C_{PI,notch}(z) = 0.296\frac{z-0.7}{z-1}\frac{z^2-1.922z+0.966}{z^2-1.719z+0.757}$$

- PI + lead filter:

$$C_{PI,lead}(z) = 0.034\frac{z+1}{z-1}\frac{z-0.75}{z-0.25}$$

- PI + lag filter:

$$C_{PI,lag}(z) = 0.010\frac{z+1}{z-1}\frac{z-0.85}{z-0.97}$$

Figure 4.7: Tuned performance of z-domain switching motion control strategies for the $G_d(z)$. The controllers $C(z)$ have a PI controller with a notch, lead, or lag filter.

Table 4.3: Characteristics of Bode plots and step responses of Tustin-discretized closed-loop actuator system $G_d(z)$ with a tuned PI controller plus an active damping filter.

Filter	**Bode Plot**		**Step Response**			
Type	Gain Margin	Phase Margin	Rise Time	Overshoot	Undershoot	Settling Time
No PI or filter	3.0 dB @ 2600 Hz	3.5°@ 2370 Hz	108 μs	94%	89%	18 ms
PI+Notch	**12 dB @ 2390 Hz**	**63°@ 959 Hz**	**230 μs**	**2%**	**4%**	**0.8 ms**
PI+Lead	2.1 dB @ 1740 Hz	91°@ 185 Hz	1350 μs	3%	15%	10 ms
PI+Lag	2.7 dB @ 1550 Hz	34°@ 563 Hz	302 μs	34%	12%	6.4 ms
Only PI	4.1 dB @ 1680 Hz	88°@ 159 Hz	1930 μs	2%	4%	5.5 ms
Only I	-30 dB @ 1660 Hz	-106°@ 3150 Hz	Unstable	Unstable	Unstable	Unstable

4.3 Parameter Sensitivity Analysis

The robustness of active damping filters under various parameter values in the PPA40L actuator model is analyzed in this subsection. The tuning of PI controller and filters has used a single set of model parameters given in Table 3.2. In reality, the exact values of these model parameters will possibly change under different working conditions, especially the mechanical-domain parameters that are influenced by the physical connections in actuator setup. The changes in $G_d(z)$ parameters will change the location of the resonant peak, and thus influence the damping effects from filters or even destabilize the overall system. Therefore, the parameter sensitivity analyses are performed in this subsection to evaluate the vibration damping effects under varied parameter values from 50% to 150% from the identified number in Table 3.2. The selected parameters are spring constant k_{piezo} or k, total mass m_{total} or m, damping ratio b_{piezo} o b and electromechanical transformation ratio T_{em} or T.

The pole-zero maps of the discrete, closed-loop actuator control system $G_d(z)$ with 50% to 150% variations in a single variable are shown in Figure 4.8 to 4.11. There are four graphs in each set, the subplot (a) shows the full-view of unit circle (the stability boundary) in the z-domain, and the other three graphs (b)-(d) are the zoomed-in views focusing on

the complex conjugate pole region. The complex conjugate poles are the poles residing near the edge of unit circles, they are also the dominant poles that cause resonant peaks in Bode plots with small damping ratios. During the parameter sensitivity tests, it is mainly the complex conjugate poles being moved around under different parameter values, and the overall closed-loop system gets destabilized once the complex conjugate poles move outside of the unit circle. Therefore, studying the moving tendencies of complex conjugate poles can forecast the performance of the overall actuator system.

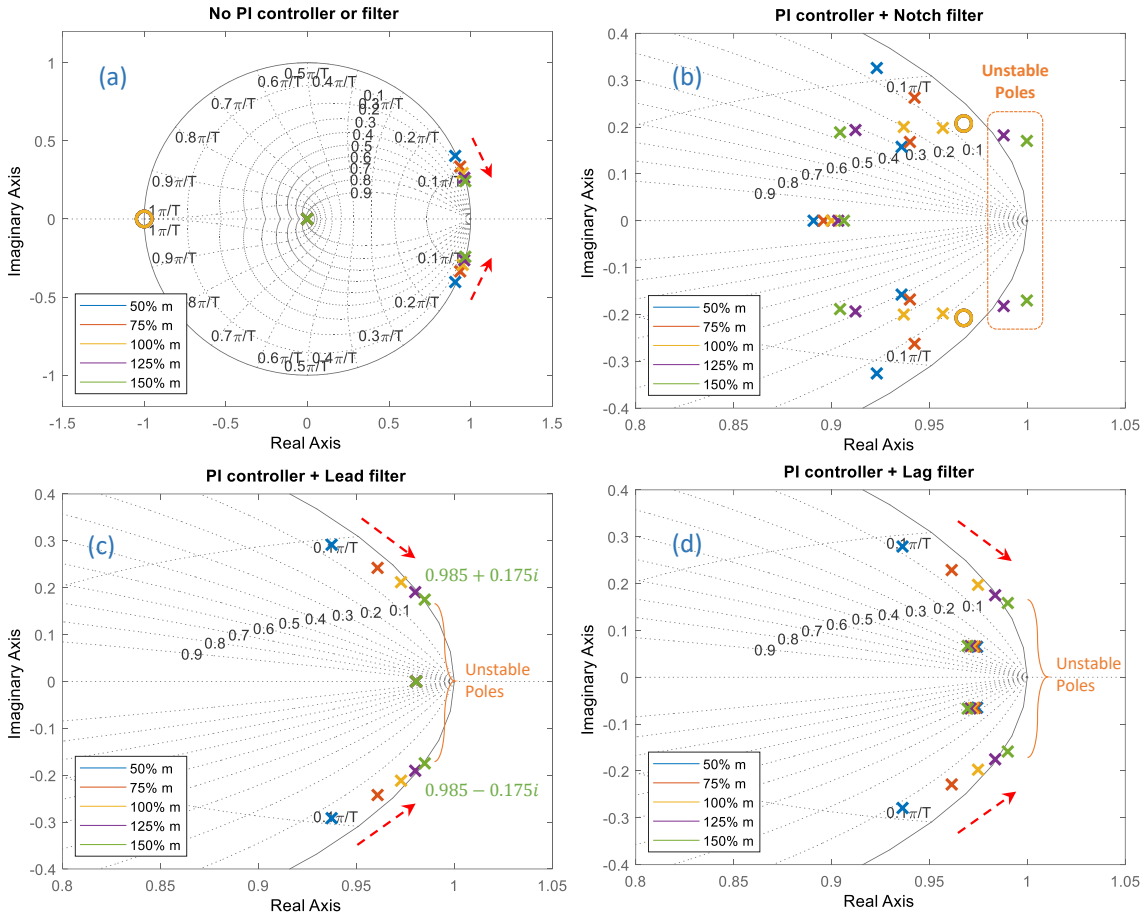

Figure 4.8: Pole-zero maps for parameter sensitivity tests on the total load mass m_{total} in discretized closed-loop PA systems with tuned digital filters.

Sensitivity analysis results on total mass m, varied from its identified value of 0.8 kg, are shown in Figure 4.8. Without a PI controller or active damping filter, the complex poles moving towards the real axis along the unit circle edge, and the stability of closed-

loop system is preserved. In the case of a PI controller with the tuned notch filter in Figure 4.8(b), the pole-zero map gets quite chaotic without a clear tendency of movements, and the closed-loop system gets unstable under 150%m (1.2 kg). Comparatively, the case of a PI controller with a tuned lead filter (Figure 4.8(c)) shows a clear movement tendency of complex poles towards the edge of unit circle, until the heaviest 150%m loading moves slightly out of the stability boundary. The case of a PI controller with a tuned lag filter (Figure 4.8(d)) demonstrates similar movements towards unit circle boundary with instability happens at heaviest 150%m loading. Generally speaking, the pole-zero maps show that the closed-loop actuator system tends to be more unstable with a larger m value, which matches with the intuitive understanding that a larger load mass gives a larger magnitude of vibrations. And the notch filter system gives the worst performance among three filters under varied total mass m values.

Sensitivity analysis results on spring constant k, varied from its identified value of 90 N/μm, are shown in Figure 4.9. The complex poles also move along the unit circle edge when a PI controller or a filter is not inserted. With a PI controller and a notch filter in the Figure 4.9(b), the pole-zero map gets also chaotic, and more pairs of complex poles move outside of unit circle under 50%k and 75%k. The closed-loop system with lead filter (Figure 4.9(c)) also owns an unstable case under 50%k, and the lag filter system (Figure 4.9(d)) has two pairs of unstable poles. The reason for the unstable system with 50%k is about the enhanced vibration in a softer spring: under a lower spring constant condition, the piezoceramic stack gets larger vibration magnitude under the same transformed force F_T like a softer spring. Generally speaking, the notch filter system gives the worst performance for its two pairs of unstable poles under varied spring constant k values.

Sensitivity analysis results on electromechanical transformation ratio T, varied from its identified value of 27 N/V, are shown in Figure 4.10. In this set of analyses, the closed-loop system keeps being stable under all variations of T.The high robustness of closed-loop system under varied T values is an encouraging result, considering a potentially large

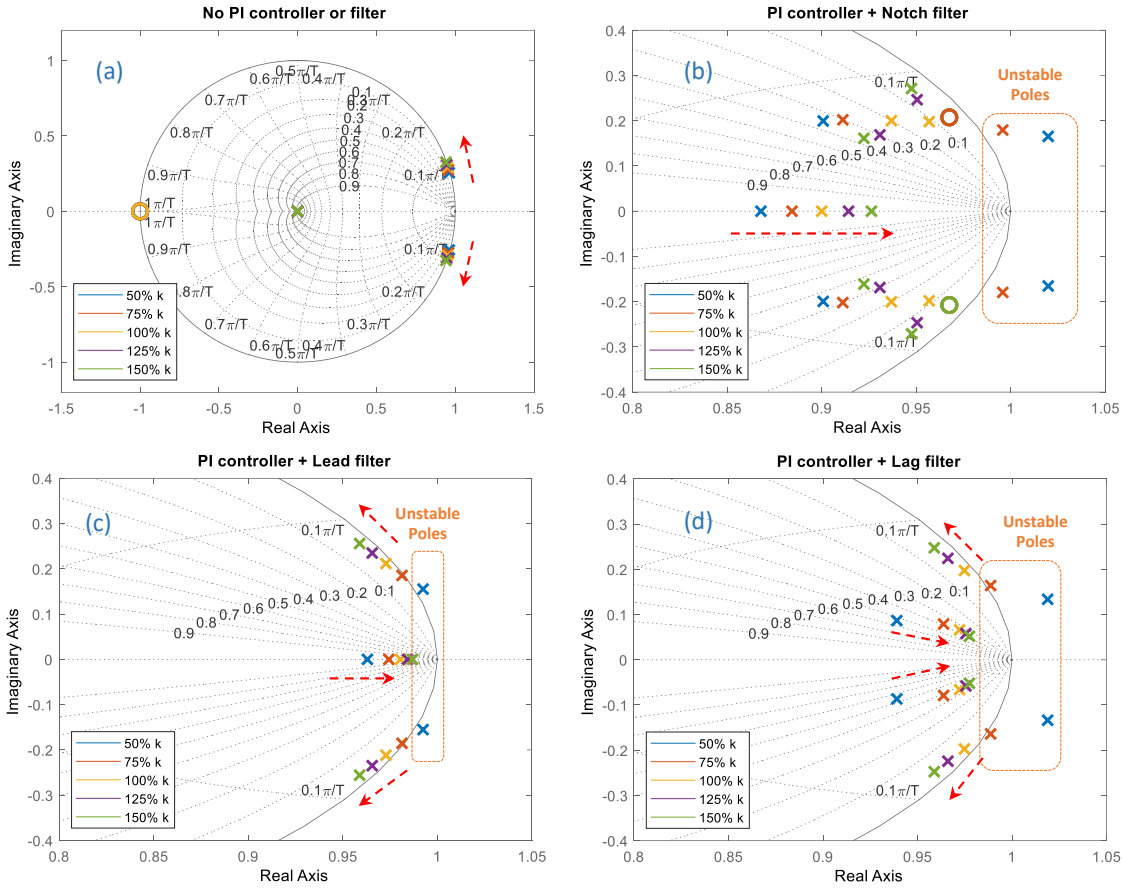

Figure 4.9: Pole-zero maps for parameter sensitivity tests on the spring constant k_{piezo} in discretized closed-loop PA systems with tuned digital filters.

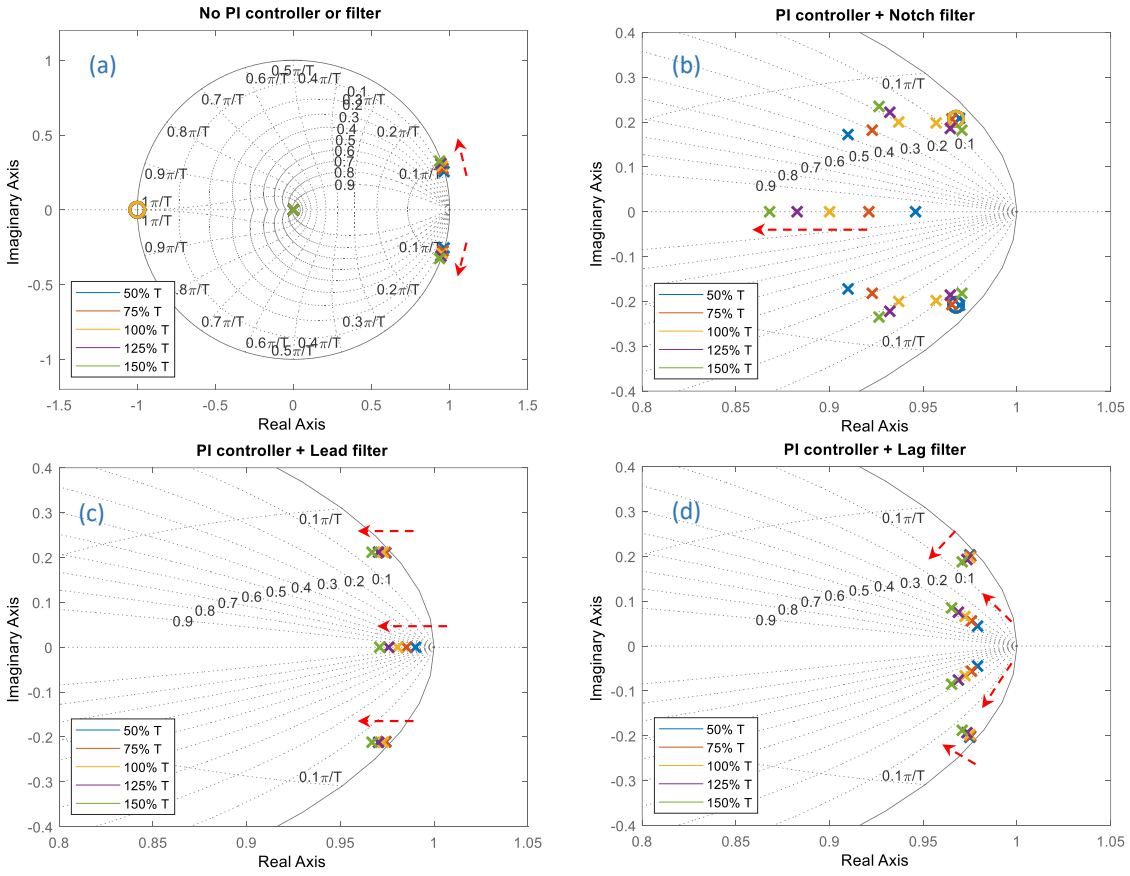

Figure 4.10: Pole-zero maps for parameter sensitivity tests on the electromechanical transformation ratio T in discretized closed-loop PA systems with tuned digital filters.

measurement error in this T parameter because it is a purely experimentally-determined parameter with non-unified expressions (see Table 3.1).

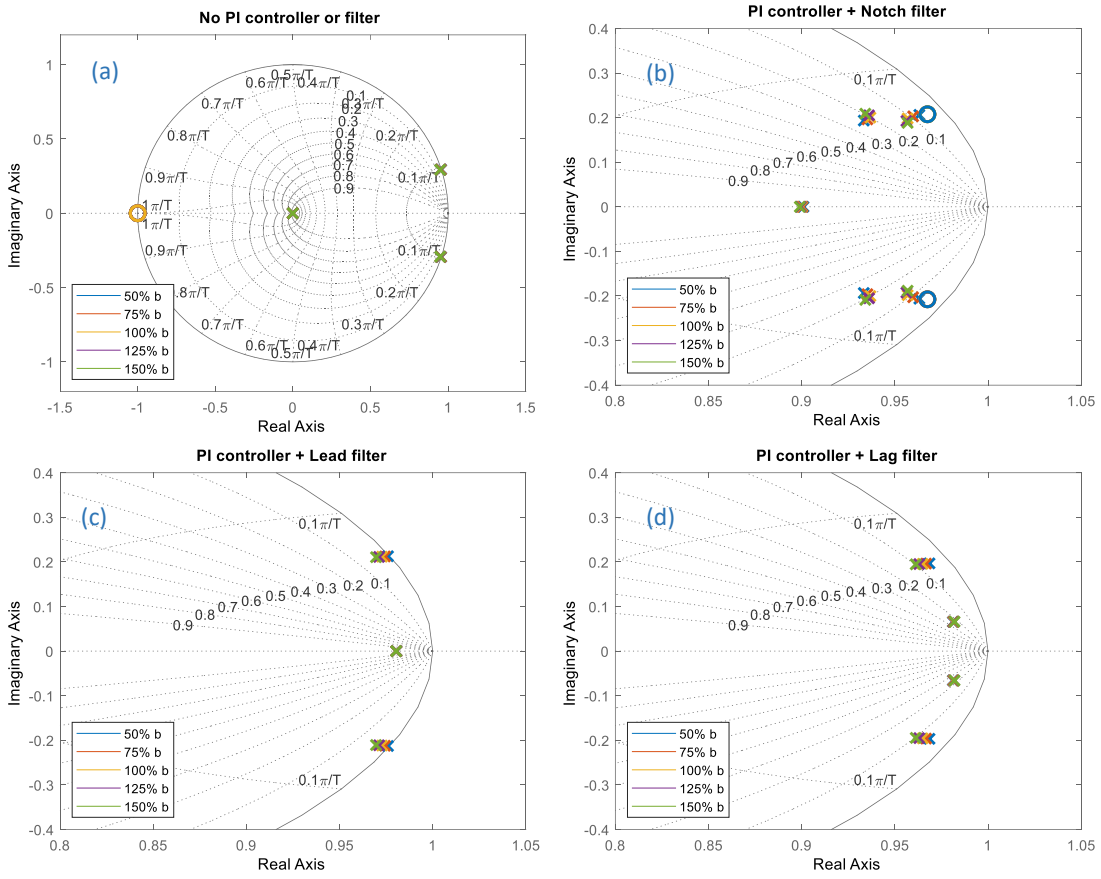

Figure 4.11: Pole-zero maps for parameter sensitivity tests on the damping ratio b in discretized closed-loop PA systems with tuned digital filters.

Sensitivity analysis results on damping ratio b, varied from its identified value of 550 Ns/m, are shown in Figure 4.11. Here the closed-loop systems not only keep being stable at all times, the movements of poles under varied b values are not significant either. It is thus safe to say that the system tolerance on b value variations is quite high. This high tolerance may also be the reason that researchers are satisfied with determination of b values through curve-fitting [77, 89]. So that the 550 Ns/m reference value of b in PPA40L actuator model is also identified from curve-fitting the open-loop travel curves (See Chapter 3).

4.4 Chapter Summary

This chapter investigates and tunes the proposed closed-loop controllers for optimized vibration damping in PPA40L actuator systems. The sensitivity of closed-loop controller with regards to $\pm$ 50% mismatches in PPA40L parameters is also studied through pole-zero maps. Generally speaking, the combination of PI controller with notch filter gives the best simulated performance with the fastest response and low undershoot, but its closed-loop system is the most susceptible to instability under mismatched model parameters. The combination of PI controller with lag filter gives comparable response speed with the notch filter set, but with much larger overshoot and undershoot in step responses. And the lag filter is more tolerant to PPA40L model parameter changes than the notch filter with regards to preserving the stability of closed-loop system. The last choice of vibration damping filter, the lead filter with a PI controller, fails to accelerate the response speed of the system from the slowest scenario with only a PI controller, so that this lead filter option is not pursued in the following hardware implementation tests.

CHAPTER 5
CLOSED-LOOP SIMULATION AND EMBEDDED CODING

With the PPA40L model constructed in Chapter 3 and active damping filters tuned in Chapter 4, the proposed switching motion controllers are verified through closed-loop simulation in this chapter. The closed-loop verifications can check the functionality of switching motion controllers that are converted from their transfer function expressions into embedded firmware codes. The considerations for selecting the controller hardware board and programming platform are also presented.

5.1 Selection of Controller Hardware

An illustration of controller design and implementation workflow is shown in Figure 5.1. So far a PPA40L actuator model has been derived in Chapter 3, and the transfer functions of proposed switching motion controllers have been tuned in Chapter 4. The next stage of workflow is the *Code* stage, which means now the switching motion controllers are ready to be converted from their z-domain transfer functions into hardware executable codes to be implemented in a microcontroller (MCU) or a digital signal processor (DSP). The detailed discussions on choosing a suitable hardware controller board for PA-FMS applications are presented in this section.

The most frequently-used controller boards in published work on PA controls are manufactured by dSPACE [16, 69, 88, 94], such as the DS1104 R&D Controller Board [16, 77, 79, 87]. The most crucial advantage of dSPACE controller boards is their seamless integration with MATLAB Simulink, so that a Simulink program with complicated operators and frequency-domain calculations can be directly converted to a hardware executable in dSPACE boards [94]. Once a Simulink model of a controller gets ready for implementation, the conversion to board-executable codes is carried out automatically through dSPACE

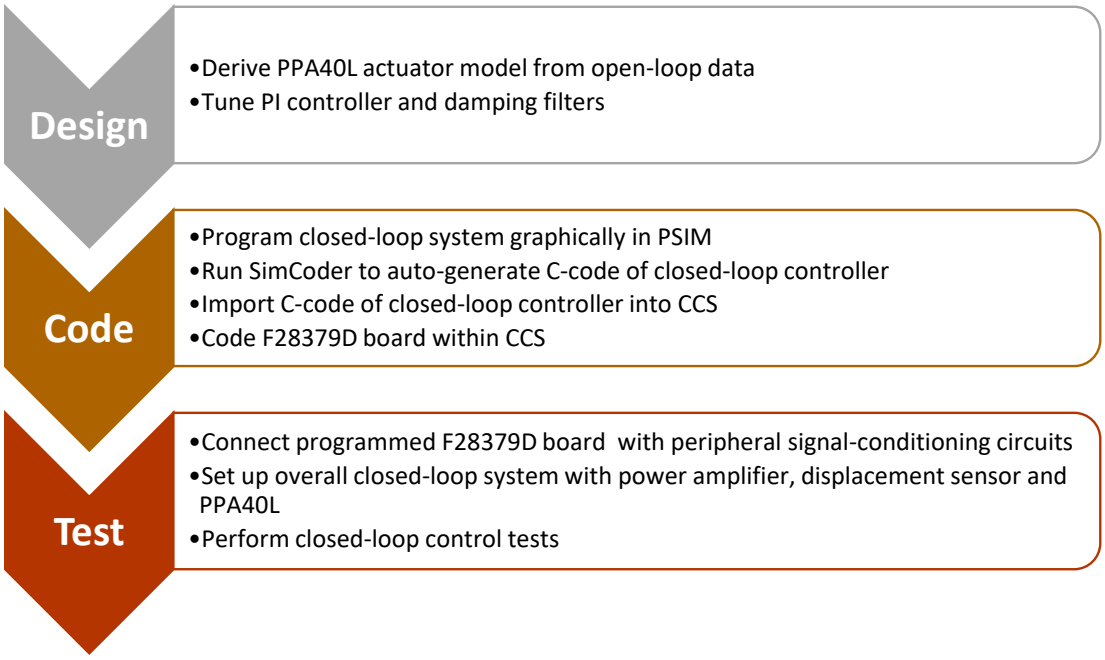

Figure 5.1: Hardware implementation workflow of PPA40L controller design.

modules within the MATLAB environment. Benefited by the ever-growing collections of Simulink library (which also has a physical model for PA) and the strong calculation capabilities of MATLAB environment, the dSPACE controller board has been the first choice for many researchers in PA modeling and control to demonstrate various kinds of trajectory-tracking algorithms[16, 94], hysteresis compensation [88, 95, 96], charge driving [82] and self-sensing techniques [87, 97, 98, 99, 100]. Moreover, dSPACE controller boards are also used in active damping studies in LCL filters for voltage-source converters [101, 102]. The two controller boards are compared in a short list of specifications between dSPACE DS1104 board and TI TMS320F28379D board [103] are provided in Table 5.1, and the differences on unrelated features with PA control are not included here.

Many of the ratings are shared by both TI TMS320F28379D MCU and dSPACE DS1104 controller board. They are both floating-point systems that support computations with fractional numbers. Their CPU clock speeds are both in the 200 MHz range, and the DS1104 is slightly higher than TMS320F28379D with 250 MHz CPU main frequency. Their ADCs

Table 5.1: Comparisons on selected features of two microcontroller (MCU) boards.

Feature	dSPACE DS1104	TI TMS320F28379D
CPU	64-bit	32-bit
	Floating point	Floating point
	250 MHz	200 MHz
	2*16 KB cache	No cache
Memory	32 MB SDRAM	204 KB RAM
	8 MB Flash	1 MB Flash
ADC	16-bit resolution	16-bit resolution
	8 channels	12 channels
	+/- 10V range	0 - 3.3V range
	0.5 MSPS @ 16bit	1.1 MSPS @ 16bit
DAC	16-bit resolution	12-bit resolution
	8 channels	3 channels
	+/- 10V range	0 - 3.3V range
GPIO	20 channels	Up to 169 channels
Software	Matlab Simulink	CCS C-script
Price	$5,300	$33

have the same resolution, and the ADCs in TMS320F28379D are lower in the input voltage range but higher in the sampling speed with 1.1 MSPS (millions of samples per second) at 16-bit resolution. Because a TI TMS320F28379D MCU can also properly serve the needs with its competitive performance, it is chosen as the hardware demonstration board in this dissertation. An image of TMS320F28379D LaunchPad is shown in Figure 5.2.

5.1.1 Coding Software - CCS and PSIM

For TI C2000^{TM}-series MCU evaluation boards like TI TMS320F28379D LaunchPads, they are mostly coded within a TI-provided integrated development environment (IDE) called Code Composer Studio (CCS). As a 22-years-old IDE for embedded processor programming, CCS mainly supports programs written in C, C++ and assembly. Thus the coding process of TI TMS320F28379D LaunchPads through CCS is not as graphical and interactive as the coding in dSPACE boards through MATLAB Simulink. Whereas, the

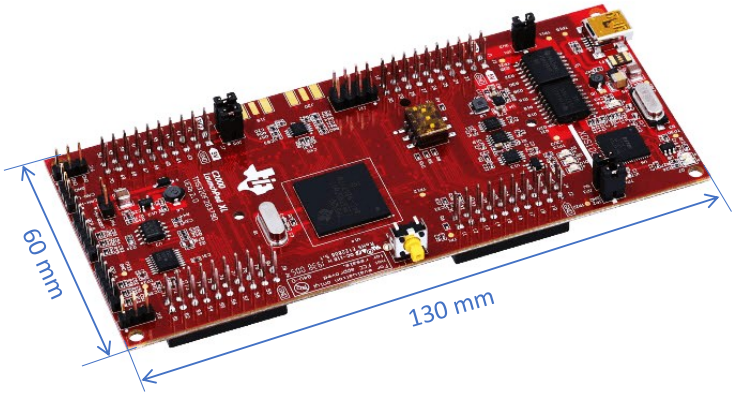

Figure 5.2: Photo of TI TMS320F28379D LaunchPad, the selected board for hardware implementation of switching motion controllers in this study.

CCS is still required for programming TI C2000 MCUs.

In this PA control scenario, although the closed-loop system with controller $C(s)$ and $C_d(z)$ have been tuned in their transfer function expressions in MATLAB, the CCS cannot compile the MATLAB script directly and make it executable in TMS320F28379D MCU. There are a handful of intermediate stages between a transfer function and a hardware-executable program, not to mention the required hardware routines like configuring general-purpose digital I/O (GPIO) terminals, initializing hardware interrupts, and setting up ADC and DAC parameters.

A type of software modules that helps expedite the coding process in embedded processors is usually referred as automatic code generators, such as the Simulink Coder^{TM} in Simulink and the SimCoder^{TM} in Powersim (also abbreviated as PSIM). The functions of automatic code generators are turning non-executable programs (like Simulink block diagrams) into MCU-executable programs (like C/C++ programs), and this conversion is done automatically by the software. The dSPACE boards utilize exactly the Simulink Coder^{TM} to achieve direct conversions from Simulink models to hardware programs.

Without using dSPACE boards or Simulink Coder^{TM}, similar automatic code conversions can be performed with SimCoder^{TM} in PSIM. PSIM is also a simulation software with very similar interfaces and libraries as Simulink, but PSIM mainly focuses on power

electronics applications like motor drives and power supplies. SimCoder^{TM} is an add-on library of elements that are running inside PSIM platform. These elements represent hardware functions like A/D conversion and D/A conversion that can be automatically converted into C-language commands. The C-language scripts are imported into CCS for building and debugging. Finally, the F28379D MCU board gets its CPU programmed by CCS, now the F28379D MCU board is ready to receive inputs and issue commands to other components in the closed-loop hardware system. In short, the detailed steps of coding a TI TMS320F28379D LaunchPad using PSIM SimCoder and CCS are listed in Figure 5.1.

5.2 Closed-loop Model and Program

Implementing a discrete controller $C_d(z)$ into a closed-loop system with time-domain PA model is referred as the closed-loop simulation in this section. Improved from mathematical multiplications of transfer functions in Chapter 4, the closed-loop simulation uses electrical components like resistor, capacitor and inductors to simulate time-domain responses of PPA40L actuator under different control inputs. The functionality and stability of the proposed $C_d(z)$ are checked with a continuous actuator model under non-step driving signals like ramp and trapezoidal waveforms. On the MCU side, the $C_d(z)$ is expressed as difference equations in one code block of the overall C script for hardware controller implementations. There are many other blocks inside the same C-script, including A/D conversion, D/A conversion and general purpose I/O (GPIO) interrupts that constitute the closed-loop controller.

5.2.1 Electrical Equivalent Circuit of Electromechanical Model

Constructing an electromechanical model of PPA40L actuator (Figure 3.10) in PSIM needs a new approach due to following reasons. Firstly, PSIM with its graphical programming environment like Simulink requires that the time-domain actuator model presented by differential Equation 3.4 must be converted into a network of graphic blocks. Secondly, PSIM

does not provide mechanical blocks like mass or spring or damper, so these components in actuator mechanical domain must be replaced by corresponding electrical components like resistor or capacitor or inductor. Thirdly, there is no public information about how to model a PA within PSIM. As a result, the equivalent electrical circuit of PPA40L actuator in PSIM has been established essentially from scratch in this study.

Luckily, it has been found that the governing equations of PAs are very similar to the ones in a permanent magnet DC motor according to [16]. After all, electrical motors are also a kind of actuators that convert electrical energy to mechanical energy. On the other hand, PSIM provides a tutorial on "Electric Machine Modeling" that elaborates on deriving electrical and mechanical equations, constructing electrical equivalent subcircuits out of equations, and packaging the subcircuits into a graphic block that can be included in another PSIM simulation [104]. Following these steps, the governing equations of the PPA40L actuator are derived from Figure 3.10 after incorporating a new parameter - the gain of power amplifier K_{amp} - into the electrical domain of PA model:

$$R_{damp}C_{piezo}q' + q - T_{em}x = C_{piezo}K_{amp}(V_{in} - \frac{H(q)}{K_{amp}}) \tag{5.1}$$

$$m_{total}x'' + b_{piezo}x' + (k_{piezo} + \frac{T_{em}^2}{C_{piezo}})x = \frac{T_{em}}{C_{piezo}}q - F_{ext} \tag{5.2}$$

The electrical equivalent circuit of Equation 5.1 and 5.2 are shown in Figure 5.3. The left loop of Figure 5.3 is the graphical representation of Equation 5.1, and the right loop of Figure 5.3 is the graphical representation of Equation 5.2. Therefore, none of the elements in Figure 5.3 has any physical meaning related with the actuator, they are just graphic representations of the equations. This is the biggest difference between this electrical equivalent circuit and the original electromechanical actuator model in Figure 3.10, because the components in Figure 3.10 have their physical meanings in PA structures.

The analogous correlation for using a parallel connection of resistor-capacitor-inductor

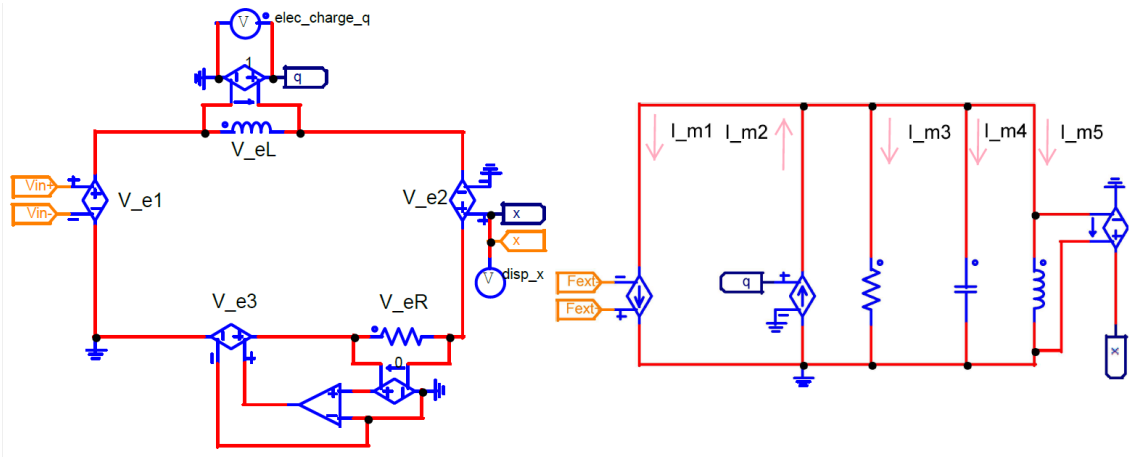

Left Loop: $V_{e1}(t) = C_{piezo}K_{amp}V_{in}(t); V_{eL}(t) = R_{damp}C_{piezo}q'(t); V_{e2} = T_{em}x(t); V_{eR} = q(t); V_{e3} = C_{piezo}H(q)$

Right Loop: $I_{m1} = F_{ext}(t); I_{m2} = \frac{T_{em}}{C_{piezo}}q(t); I_{m3} = b_{piezo}x'(t); I_{m4} = m_{total}x''(t); I_{m5} = \left(k_{piezo} + \frac{T_{em}^2}{C_{piezo}}\right)x(t)$

Figure 5.3: Proposed electrical equivalent circuit representing the electromechanical model of the PPA40L actuator in PSIM closed-loop simulation.

to represent original mass-spring-damper in the mechanical domain are shown in Equation 5.3. Here the three parallel branches share the same voltage drop, $V_R = V_C = V_L = x'$, and x' is the velocity of the actuator represented by the current through a unit-gain resistor. Then the position x of the actuator is represented by the current through a unit-gain inductor, and the acceleration x'' of the actuator is represented by the current through a unit-gain capacitor. After assigning a resistance of $1/b_{piezo}$, a capacitance of m_{total}, and an inductance of $1/(k_{piezo} + T_{em}^2/C_{piezo})$, the left-half of Equation 5.2 is represented graphically by this parallel resistor-capacitor-inductor connection in Figure 5.3. Again, these electrical components in Figure 5.3 are not physically-existed features in PA, they are simply graphic

expressions of mathematical terms in Equation 5.2.

$$\begin{aligned} x &= \int V_L dt = i_L(L=1); \\ x' &= V_R = i_R(R=1); \\ x'' &= \frac{dV_c}{dt} = i_c(C=1); \end{aligned} \tag{5.3}$$

5.2.2 Hardware Coding and Event Flow

Closed-Loop Simulation Diagram

With the electrical equivalent subcircuit of the PPA40L actuator constructed in previous subsections, the switching motion controllers can be coded into the TI F28379D MCU LaunchPad through a PSIM model. The same PSIM model is used for closed-loop simulation with its simplified block diagram shown in Figure 5.4. From the lower left corner where the PPA40L subcircuit resides, the position of actuator x_{piezo} is converted to a voltage signal $V_{disp,sen,out}$ through the displacement sensor. The $V_{disp,sen,out}$ is the real-world input signal to the MCU board, and it is sampled by the ADC at sampling frequency f_s and turned into a digital signal V_{ADC} coming into the C block. The C block is a special element provided by SimCoder within PSIM that accepts hand-coded C-scripts, so that all the customized functions for switching motion controllers are implemented in the C block. Checking the functionality and correctness of this C block is the primary goal of the closed-loop simulation, because the C block contains self-created codes that may cause hardware errors during controller operations. The output of C block is a low-voltage signal V_{DAC} outputted through MCU DAC. This V_{DAC} works as the input signal to the power amplifier, after a voltage amplification by a ratio of K_{amp}, a high-voltage signal V_{piezo} is outputted from the power amplifier to drive the PPA40L actuator. Now the control system of PPA40L actuator is closed by the MCU board as shown in Figure 5.4.

Figure 5.5 shows the detailed element connections in the closed-loop simulation in

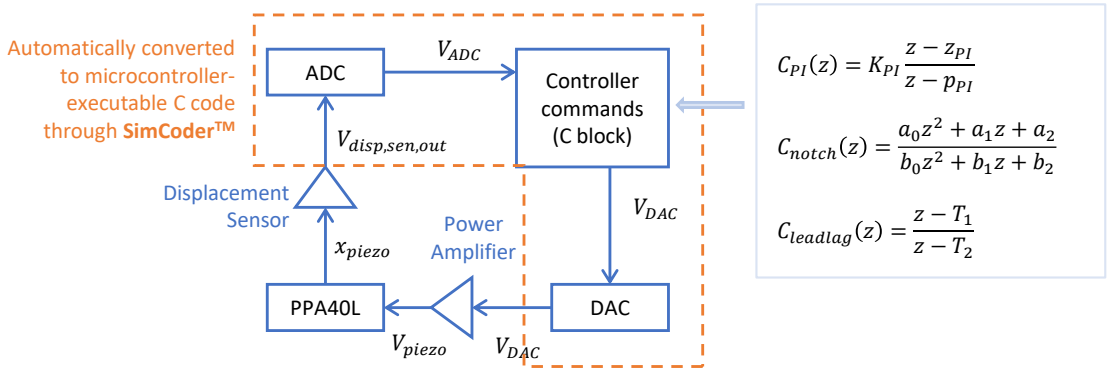

Figure 5.4: Block diagram of the closed-loop simulation for PPA40L actuator.

PSIM. Rooted from block diagram in Figure 5.4, the PPA40L block contains the subcircuit shown in Figure 5.3. The output of PPA40L block x_{piezo} goes through a proportional block representing the displacement sensor (K = -8 mV/μm), a low-pass filter representing the 10 kHz bandwidth of displacement sensor. The output voltage of displacement sensor in Figure 5.5 is $V_{disp,sen,out}$. This $V_{disp,sen,out}$ voltage is divided by three to be reduced from 0 - 12 V range to 0 - 4 V range, in order to avoid damaging the 3.3 V ADC in the MCU. The ADC block samples at 50 kHz to generate the digital signal V_{ADC}, which is fed as one input into a SimCoder C block. The other three inputs are trigger signals coming from GPIO ports in the MCU, and their functionalities on guiding the event flow of controller codes will be discussed in next subsection.

As shown in Figure 5.5, the only visible information of the Simcoder C block is its input and output ports. This means that once the terminal variables of the C block are properly defined, the internal functions are not limited to predefined ones in the PSIM library. This unlimited flexibility of C block functions is actually the biggest advantage of using this Simcoder C block to implement switching motion controllers. Because SimCode C blocks can include complicated functions that are not supported by graphical elements in the PSIM library, such as user-defined waveshape and if-else decisions. In this simulation model, all the if-else decisions and controller difference equations are contained within a single C block. The output side of the C block has the controller output V_{DAC} and a

debugging probe x_{ADC}. Then the DAC block converts the outputs of the digital controller into analog voltage signals V_{in} at a frequency of 50 kHz, as synchronized with the 50 kHz ADC. Finally, the analog V_{in} waveform flows into the power amplifier whose bandwidth is represented by a 300 kHz low-pass filter, and the gain K_{amp} has been integrated inside the PPA40L subcircuit. In this way, the control loop of closed-loop simulation has been closed.

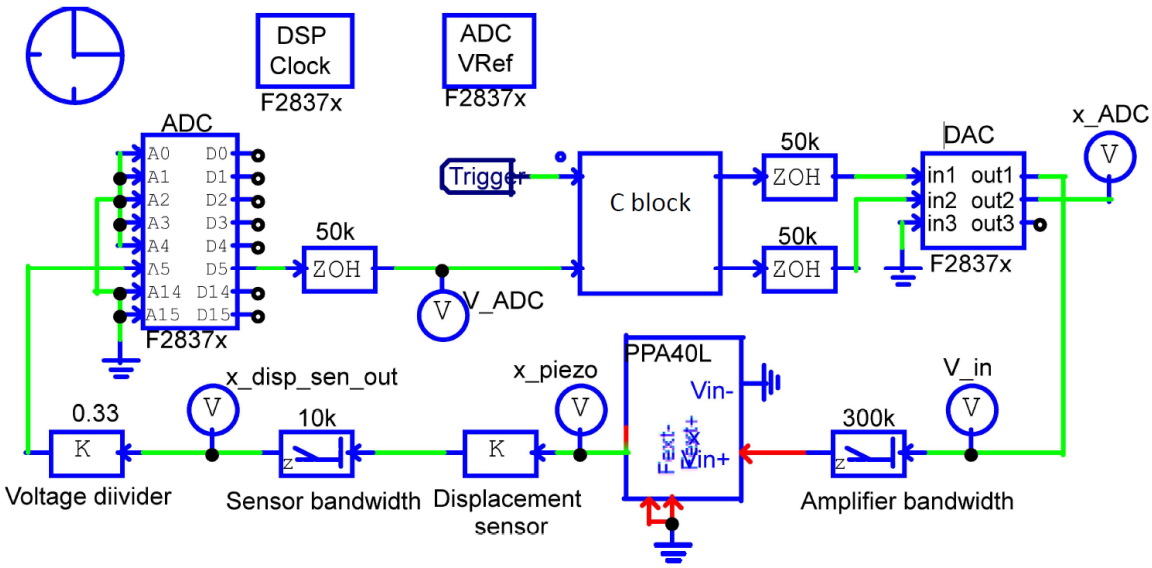

Figure 5.5: PSIM setup with SimCoder elements (ADC, DAC, DSP clock, ZOH) and the PPA40L subcircuit for closed-loop simulation.

Flowchart of the Controller Block Program

The detailed event flow within the SimCoder C block is shown in the "PSIM - C block Flow" of Figure 5.6. This C block flow starts with obtaining real-time boolean value of trigger signal through GPIO ports, and the real-time voltage value of the divided sensor output voltage V_{ADC} through ADC port. The real-time position of actuator x_{ADC} can be calculated out of V_{ADC}. Depending on the boolean values of trigger inputs, if both the "SAFETY" and "CHARGE" values are true, the program advances to check the "RELEASE" value; if either the "SAFETY" or the "CHARGE" value is false, the program bypasses all remaining stages and directly goes to the end of controller block. An additional "SAFETY" trigger

signal is used to avoid mistriggering by an unstable "CHARGE" signal. The second if-else decision checks the value of "RELEASE" signal: if the "RELEASE" value is false, the controller should charge up its output and increase PA displacement up to the high level x_{high}, and hold at x_{high} to keep the contacts in PA-FMS firmly closed; if the "RELEASE" value is true, the actuator should start to release its output and decrease its displacement down to the low level x_{low}, and the movement of actuator (load top) during this "RELEASE" process is the travel curves being controlled during PA-FMS switching-off process.

The controller reference input x_d is calculated as follows. As the voltage increases and the PA expands with "CHARGE = 1, RELEASE = 0" trigger signals, the desired displacement x_d is a ramp-up signal defined by $x_d = (t_{lead,total} - t_{lead,now})/t_{lead,total} * x_{high}$. Here $t_{lead,total}$ is the total lead time that x_d increases from 0 to x_{high}. The $t_{lead,now}$ is a countdown timer goes from $t_{lead,total}$ to 0, and when $t_{lead,now}$ equals zero, the x_d reaches the desired maximum displacement value of x_{high}. Similarly, during voltage decreasing process to shrink PA with "CHARGE = 1, RELEASE = 1" trigger signals, the x_d is a ramp-down signal defined by $x_d = (x_{high} - x_{low}) * t_{tail,now}/t_{tail,total} + x_{low}$. When the count-down timer $t_{tail,now}$ drops from $t_{tail,total}$ to 0, the x_d drops from x_{high} to x_{low}. Collectively, the desired displacement x_d is a trapezoidal waveform with predefined lead time t_{lead} and tail time t_{tail} for driving the PA to move accordingly.

$$x_{err}[n] = x_d[n] - x_{ADC}[n] \tag{5.4}$$

$$x_{PI,out}[n] = x_{PI,out}[n-1] + x_{err}[n] - Z_{PI}x_{err}[n-1] \tag{5.5}$$

$$x_{notch,out}[n] = x_{PI,out}[n] + a_1 x_{PI,out}[n-1] + a_2 x_{PI,out}[n-2] - b_1 x_{notch,out}[n-1] - b_2 x_{notch,out}[n-2] \tag{5.6}$$

$$x_{lag,out}[n] = x_{PI,out}[n] - T_1 x_{PI,out}[n-1] + T_2 x_{lag,out}[n-1] \tag{5.7}$$

After the reference x_d and the feedback x_{ADC} are both obtained, the error of these two variables is then fed into the difference equations that govern the controller. The PI controller comes first, and its difference equation shown in Equation 5.5 is transformed from $C_{PI}(z)$ given in Figure 5.4. A notch or a lag filter comes after the PI controller in the C block flow of Figure 5.6, and their difference equations are shown in Equation 5.6 and Equation 5.7. The output of controller function, $x_{filter,out}$, is once the final output of controller as illustrated in Bode plots, step responses and pole-zero maps in last chapter. However, in this chapter, the $x_{filter,out}$ is not the final output at the DAC port of microcontroller board, as a conversion from a displacement value $x_{filter,out}$ back to a voltage value V_{DAC} is needed according to $V_{DAC} = x_{filter,out}/x_{max} * (V_{max} - V_{min})$. The x_{max} is the maximum displacement that the PA can achieve under the MCU control.

Finally, the output signal of the C block is a 0-3.3 V analog voltage signal V_{DAC} through MCU DAC. The DACs in F28379D MCU have buffers at their output terminal that boost their output drive capability, so the MCU LaunchPad can substitute the function generator used in open-loop tests (Figure 3.5) to drive the power amplifier.

Flowchart of the Microcontroller C Program

After finishing the C block program and the overall closed-loop graphical model, the C project to be coded in F28379D LaunchPad through CCS can be automatically generated by SimCoder in PSIM. . The event flow of auto-generated MCU code is shown as a separate column in Figure 5.6. Like all other embedded systems, the MCU LaunchPad loads the codes from its flash to its RAM once the board is powered up or the RESET button is pressed. The execution of software codes starts with the *main()* function, which calls *Initialize()* function and enables global interrupts. Within the *Initialize()* function, the ports for ADC, DAC and GPIO (trigger signals) are defined, and the ADC interrupt is initialized

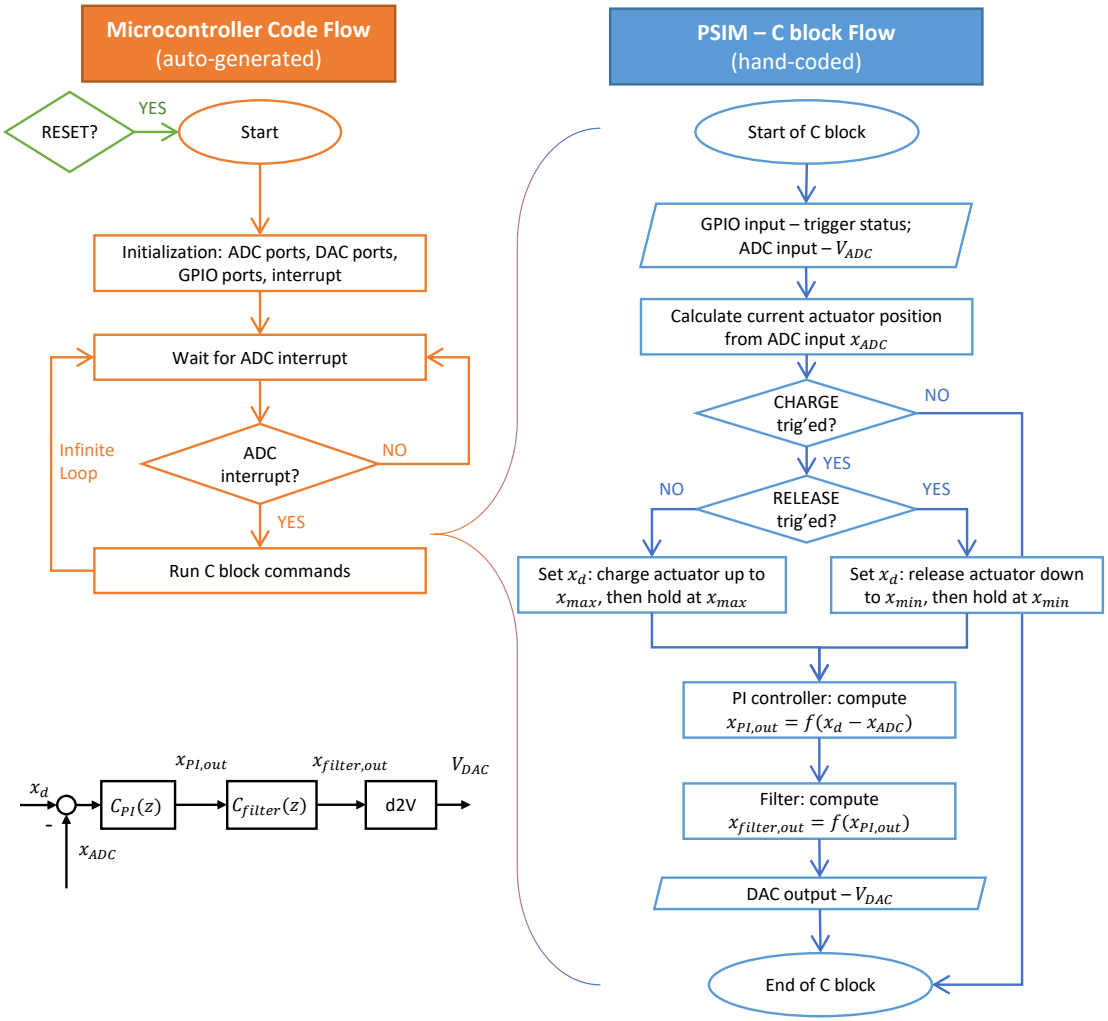

Figure 5.6: Flowchart of auto-generated microcontroller code and hand-coded C-block code in PSIM. Closed-loop simulation aim to verify the correctness of hand-coded C-block code within the PSIM environment.

at 50 kHz. The 50 kHz is thus the sampling frequency of ADC, it is also the output update frequency of DAC because the DAC functions are incorporated within the ADC interrupt routine.

After the ADC interrupt is initialized, the MCU enters an infinite loop of following events: wait for ADC interrupt, enter ADC interrupt routine once triggered, execute ADC interrupt routine codes including the C block commands, and then wait for the next ADC interrupt call. The existence of an infinite loop means all the C block commands will be executed from the top line to the bottom line every 20 μs (at 50 kHz ADC interrupt frequency) once the MCU board is powered up. This repetitive nature of MCU code has guided the design of C block programs. Some triggers like "SAFETY", "CHARGE" and "RELEASE" are introduced as flags to indicate the current status of controller flow.

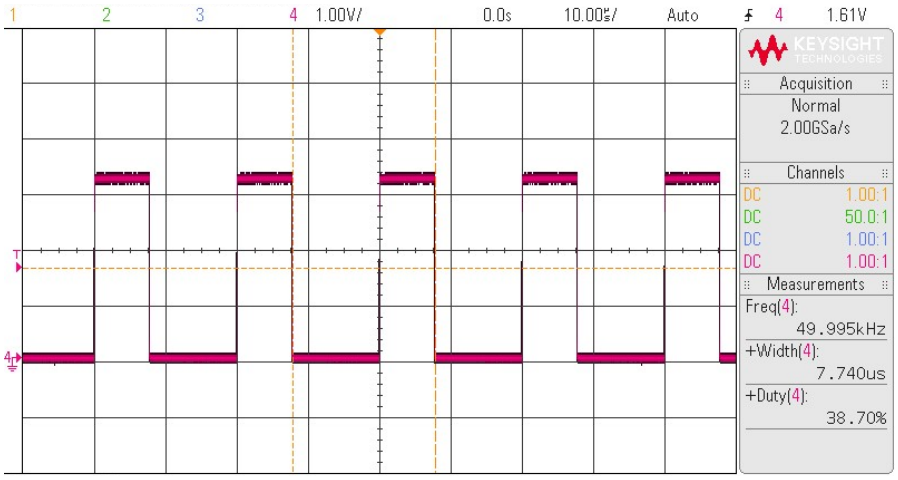

Figure 5.7: Experimentally obtained ADC interrupt frequency and duty cycle from the F28379D MCU board executing the closed-loop PI controller with a notch filter.

A controller update rate of 50 kHz in the MCU has been confirmed experimentally as shown by Figure 5.7. A GPIO pin was set to high right after the infinitely-loop ADC interrupt was entered, even before the C block software commands were executed. And then this GPIO pin was set to low right before the ADC interrupt was about to exit, after all the C block commands were finished. The pulse width of 7.74 μs shown in Figure 5.7 indicated the true time duration of controller code executions within the F28379D MCU

board. The controller codes only occupied 38.7% duty cycle of the ADC interrupt time window, so a stable ADC frequency of 50 kHz was maintained in the hardware-coded switching motion controllers.

Figure 5.7 also implies the maximum DAC control update rate (also the ADC sampling frequency) using this F28379D MCU board is about 125 kHz, considering the total execution time per ADC cycle is about 8 μs (more specifically, 7.74 μs). For this thesis study, a 50 kHz interrupt frequency is chosen as an intermediate level that does not overburden the MCU board nor control the PA too slowly. Moreover, a 50 kHz ADC frequency can sample up to 25 kHz harmonics of an input signal without significant distortions according to Shannon's theorem, so the dominant resonant peaks in the several kilohertz range of the PPA40L system bode plots (see Figure 4.7) can be captured easily.

5.3 Closed-Loop Simulation Results

Simulated waveforms from closed-loop models are provided in this subsection. As shown in Figure 5.3, the control loop is constructed with the equivalent circuit of PPA40L actuator (with 415 g load mass), ADC and DAC modules in MCU boards, and signal conditioning peripherals. Most importantly, the PA controllers being tested in these simulation circuits are exactly the same commands as the ones to be flashed into MCU board. Once these closed-loop simulation gives satisfactory vibration damping performance, it is very likely that the MCU board will give similar control performance in hardware implementation tests.

Case 1: Full Switching Cycle

Figure 5.8 shows a low-speed, full-range switching cycle with 10 ms lead time t_{lead} and 1 ms tail time t_{tail}. During closed-loop simulation for vibration damping performance, the desired high level of displacement x_{high} is set as 44 μm under 150 V driving voltage as usual, but the desired low level of displacement x_{low} is elevated to 4 μm to get larger

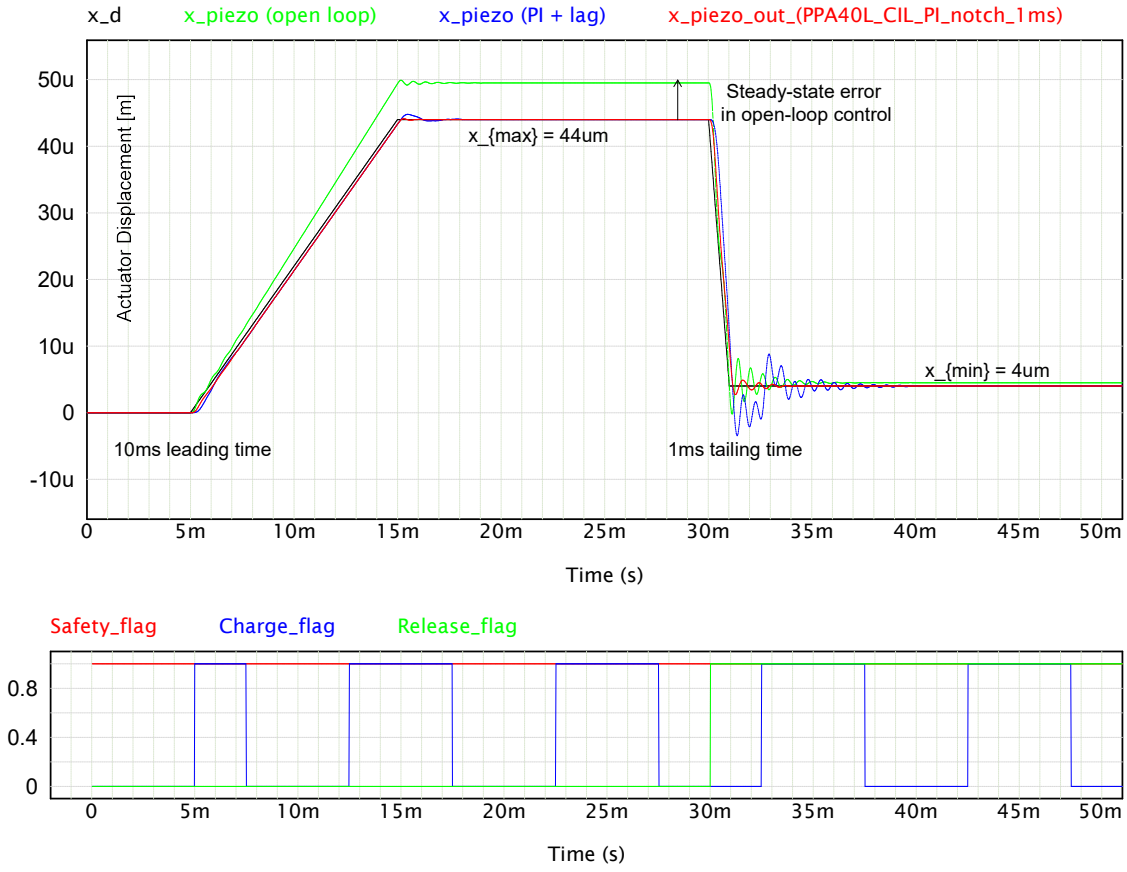

Figure 5.8: Simulated waveforms of full-range travel curves in closed-loop simulation with slow-speed switching (t_{lead} = 10 ms, t_{tail} = 1 ms).

"controllable range" for MCU DAC output.

If the x_{low} is set at 0 μm during MCU-controlled actuations, the subsequent vibration will oscillate above and below the 0 μm reference line. Although the MCU board can output positive V_{DAC} to compensate downward movements of actuator, the MCU has no means to output negative V_{DAC} to compensate upward movements of actuator that lead to more harmful undershoots. Thus, for the purpose of demonstrating vibration damping through MCU board, the actuator is set at an above-zero settling position like 4 μm.

The simulated travel curves under the open-loop control, the closed-loop control with a PI plus a lag filter, and the closed-loop control with a PI plus a notch filter are illustrated in Figure 5.8. It is a distinct contrast that the open-loop travel curve deviates significantly from the reference signal x_d at a high displacement level, while the closed-loop travel curves adhere closely to x_d with eliminated steady-state errors thanks to their PI controllers.

The turning points in travel curves are triggered by the SAFETY, CHARGE and RELEASE signals as shown in Figure 5.8. For demonstration purposes, both SAFETY and RELEASE triggers are connected to step signals that change from 0 to 1 for only once. While the CHARGE trigger is connected to a square signal that constantly switches between 0 and 1 to show the immunity of controller to unstable inputs, such as a bouncing button that issues the CHARGE signal. As shown in Figure 5.8, the actuator charging-up process is initiated at the first rising edge of CHARGE signal and continued to reach the x_{high} level despite the CHARGE signal keeps jittering afterward, so that this highly-stable triggering design can function normally under a noisy environment in reality.

Case 2: High-frequency Vibration Attenuation

Figure 5.9 shows the attenuation performance on high-frequency vibration from three switching motion control strategies. The simulated control strategies keep the same with Case 1, but the reference displacement input x_d in this case has a tail time t_{tail} of 150 μs to incite high-frequency vibration in open-loop PA system.

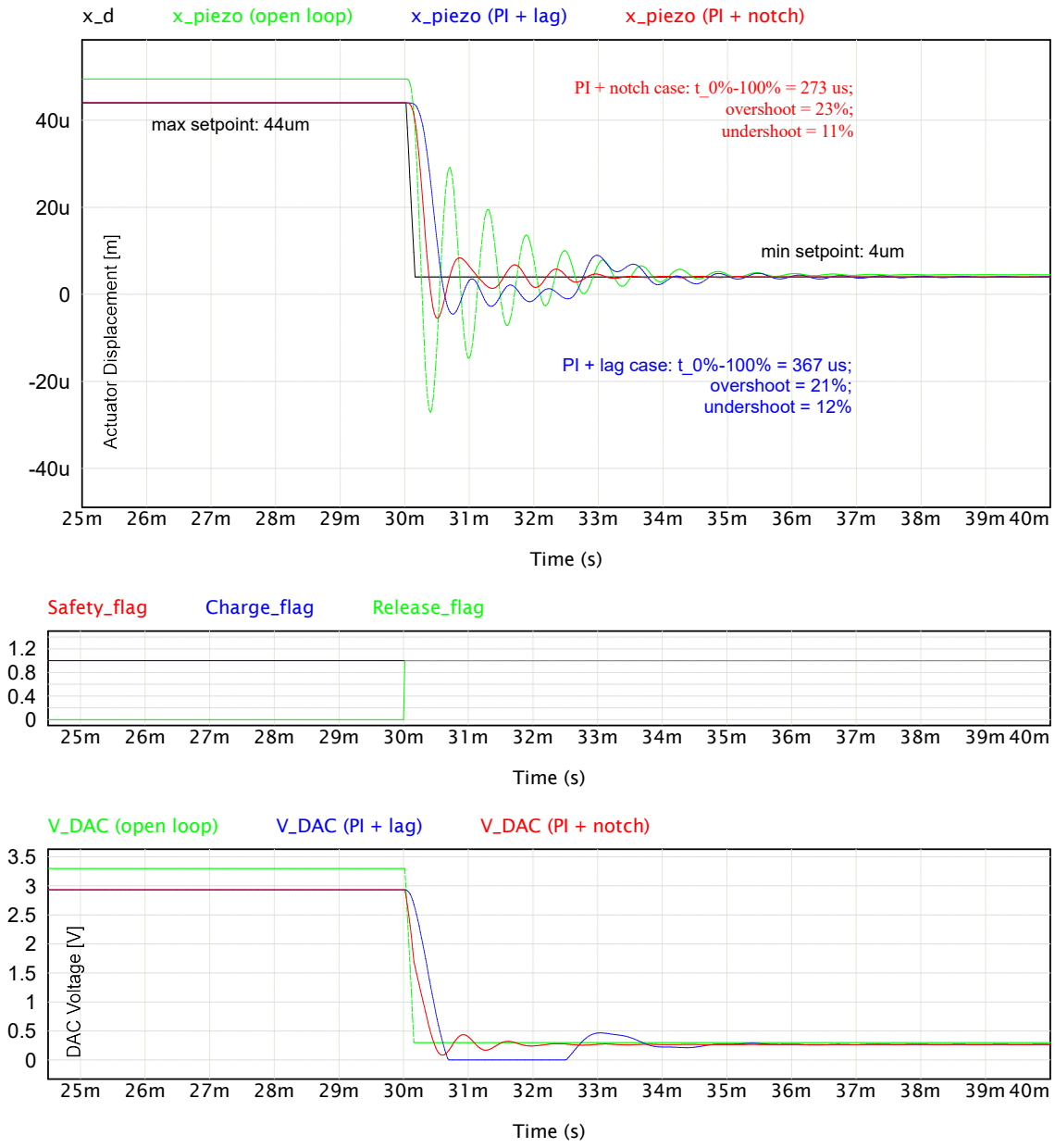

Figure 5.9: Simulated waveforms from closed-loop verification to demonstrate damping effects on the high-frequency vibration. The reference displacement x_d has a 150 μs tail time for the PPA40L actuator carrying a 415 g load mass.

According to Figure 5.9, both notch and lag filters can successfully damp the high-frequency vibration with a resonant frequency of 1680 Hz. The notch filter performs better than the lag filter as expected. Compared to open-loop travel curves with 75% overshoot and 62% undershoot, the notch-filtered travel curve has a full-range switching time t_{sw} of 273 μs, an overshoot of 23% and an undershoot of 11%. Comparatively, the lag-filtered travel curve has a slightly larger t_{sw} of 367 μs and similar overshoot and undershoot around 10%.

The DAC output voltage waveforms are also given in Figure 5.9. The V_{DAC} waveform is clearly trimmed at 0 V in "PI + lag" scenario; thus, the movements of actuator in the negative half-plane (below 0 μm) are not controlled by the MCU outputs. This is the reason why the minimum setpoint of displacement is above zero, so that the uncontrolled region with a negative V_{DAC} is minimized. Comparatively, the V_{DAC} in "PI + notch" scenario stays above zero all the time, so the movements of actuator are continuously adjusted by the MCU controller to achieve a functional closed-loop control.

Case 3: Low-frequency Noise Attenuation

Figure 5.10 shows the attenuation performance of actuator controllers on the externally-introduced, low-frequency vibration affecting the travel of the PA. The external vibration is represented by a 200 Hz sinusoidal waveform with 5 μm peak-to-peak magnitude in this simulation. As guided by experimental observations, the vibration starts at the same time moment as the PA switching-off process initiates, because it is the high acceleration force during switching-off process that shakes the PA base block and generates the low-frequency vibration.

According to Figure 5.10, the open-loop travel curve is affected by the low-frequency vibration and fluctuates along with the external noise signal. To the contrary, the vibration magnitudes in lag-filtered and notch-filtered travel curves are negligible since 5 ms after the switching-off process starts. The counteractions of external oscillations in closed-loop

travel curves are performed by the waving V_{DAC} voltages in closed-loop systems, which makes the PA expand or shrink accordingly with external disturbances from a shaking base block. The load top x_{piezo} stays relatively stable after the PA actively counteracts the external vibration.

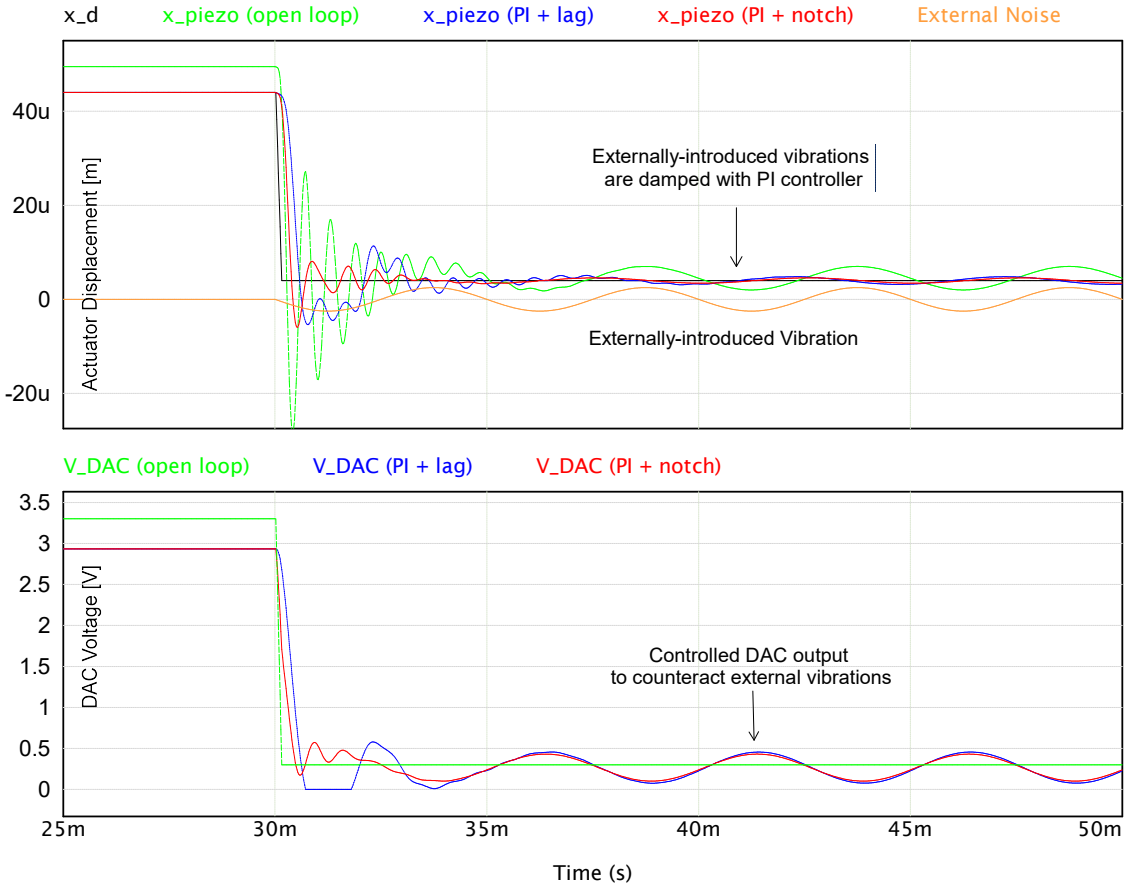

Figure 5.10: Simulated waveforms from closed-loop verification to demonstrate the damping effects on the externally-introduced, low-frequency vibration. The reference displacement x_d has a 150 μs tail time for the PPA40L actuator carrying a 415 g load mass.

The external mechanical disturbances can come from different directions. So far, we have only discussed the vibration coming from an unstable base block underneath the actuator 3.5. The mechanical disturbances could also come from PA-FMS structures above the actuator, such as the bushings carrying stationary contacts in Figure 2.8. These bushings are under compressive force (>150 N) when the moving contacts carried by actuator are firmly pressed onto the stationary contacts. They are vertically deformed by the com-

pressive force. Once the compressive force from PA is removed during contact opening process, the bushing ends may be subject to uncontrolled vibration. Similar to the actuator-side vibration, the bushing-side vibration may also change contact gap distance and thus PA-FMS insulation strength. From the PA control perspective, the mitigation of bushing-side vibration can be similar to actuator-side vibration attenuation considering they are both low-frequency dynamics.

5.4 Chapter Summary

This chapter selects a TI TMS320F28379D LaunchPad as the MCU hardware to implement the proposed switching motion controllers. The programming of controller functions into MCU board is facilitated by the CCS and the PSIM, and the functionality of embedded controller codes is verified by the closed-loop simulation under three control strategies: open-loop, closed-loop with a PI controller and a lag filter, and closed-loop with a PI controller and a notch filter. The simulation results have demonstrated that both control strategies with a PI controller can eliminate steady-state errors and reduce low-frequency noises. The notch-filtered control performs the best in closed-loop simulation by meeting all the targeted goals of PA travel curves.

CHAPTER 6
HARDWARE IMPLEMENTATION OF MOTION CONTROL STRATEGIES

In this chapter, the proposed motion control strategies for FMS switching operations are implemented in the PPA40L actuator setup and compared with experimentally obtained travel curves. The hardware implementation of closed-loop control systems with TMS320F28379D MCU LaunchPad and signal conditioning circuits are first described with related practical considerations. Next, the travel curves of PPA40L actuator under PI control only, PI control with a lag filer, or PI with a notch filter control strategies are measured from the hardware tests. Finally, the measured travel curves are compared with published switching travel curves in PAs and Thomson coil-actuated travel curves to consolidate the outstanding performance of proposed switching motion controllers both in width and depth.

6.1 Test Setup with Signal Conditioning Circuit

6.1.1 Overview

The block diagram in Figure 6.1 shows how the F28379D MCU interfaces with other devices in the closed-loop controller implementation tests. Compared to the open-loop system block diagram of Figure 3.1, it can be seen that the MCU board substitutes the function generator to issue input signals into the power amplifier, that is, the V_{signal} in the open-loop control is replaced by the V_{DAC} in the closed-loop control. The outputs of displacement sensor are routed back into the MCU board to closed the control loop.

Grounding Reference

Due to the low level of component integration in the current lab setup and the sub-millisecond switching time in PA signals, the ground references for all components in the closed-loop

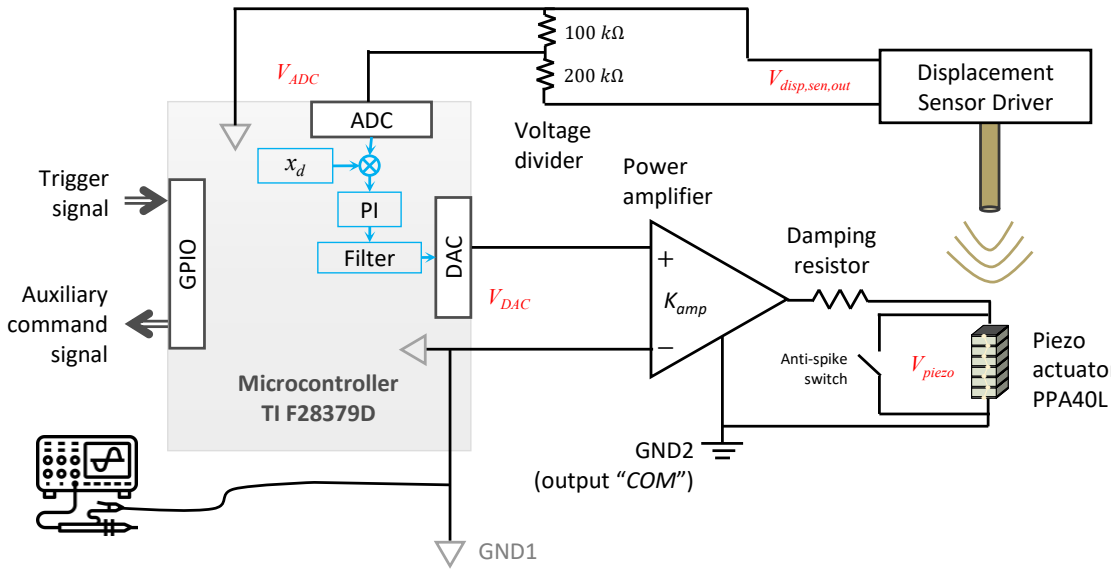

Figure 6.1: Schematic of the closed-loop hardware test setup with the MCU board and the PA system.

system should be analyzed in detail. The MCU board has four internally connected GND needle pins to interface the ground references of all peripherals. For example, the ground reference of the unbalanced BNC input terminal in the power amplifier is hooked onto the GND pin 22 of MCU (near the DAC1 pin 30), and the ground reference of output terminal in the driver of the displacement sensor is hooked onto the GND pin 62 of MCU (near the ADC pin 66). If neglecting the potential differences of four GND pins on the same MCU board, a common ground reference GND1 is shared among the MCU board, the input side of power amplifier and the displacement sensor driver. When using non-isolated probes, such as Teledyne Lecroy PP016 probes, to measure $V_{disp,sen,out}$, V_{ADC} and V_{DAC} waveforms, the ground clips of probes are also hooked onto this GND1 ground reference.

There is a second ground reference in the hardware setup: the GND2 point at the "COM" output terminal of power amplifier, due to the input-output isolation inside the power amplifier. As illustrated in the back panel of AE Techron 7224 amplifier of Figure 3.2, there are three separate output terminals: "OUTPUT" (positive), "COM" (negative) and "CHASSIS GROUND" (ground). A 2.7 Ω factory-installed resistor is used to connect

"COM" terminal with "CHASSIS GROUND" terminal to lift the "COM" potential off the "CHASSIS GROUND" potential. Considering the "CHASSIS GROUND" potential is the same as the input-side ground reference GND1, a different ground reference at the "COM" output terminal is named as GND2 in Figure 6.1. When measuring the piezo driving voltage V_{piezo} through the same oscilloscope with the other three channels whose BNC shields are interconnected, an isolated probe (Tektronix P5200) is used to separate the GND2 potential on the actuator side of the probe from the GND1 potential on the oscilloscope side of the probe.

Interpreting the power amplifier as the dividing line between the control loop and the power loop, all components in the control loop share the same ground reference GND1 (the MCU, the displacement sensor, and the input side of power amplifier), and all the components in the power loop share the same ground reference GND2 (the PA and the output side of power amplifier). These two loops are isolated from each other by the internal isolation of the power amplifier. In this way, there is no ground loop problem existing in the hardware implementation setup.

MCU as an Embedded Controller

In Figure 6.2, it can be found that the established closed-loop controller does not need a standard computer (desktop or laptop) being in the control loop to "instruct" the controller during operations. Using a separate computer to instruct controller operations is a common approach in PA controllers that are implemented with dSPACE boards [77, 95, 94]. Being a different way of hardware implementation for PA-FMS applications, the F28379D MCU board loads the controller codes from its own flash memory without computer interference, and it is even powered independently by a 5 V wall charger. This means that a fully-developed F28379D MCU board can perform all the expected controller functions to instruct its own peripherals once a 5 V DC supply is provided.

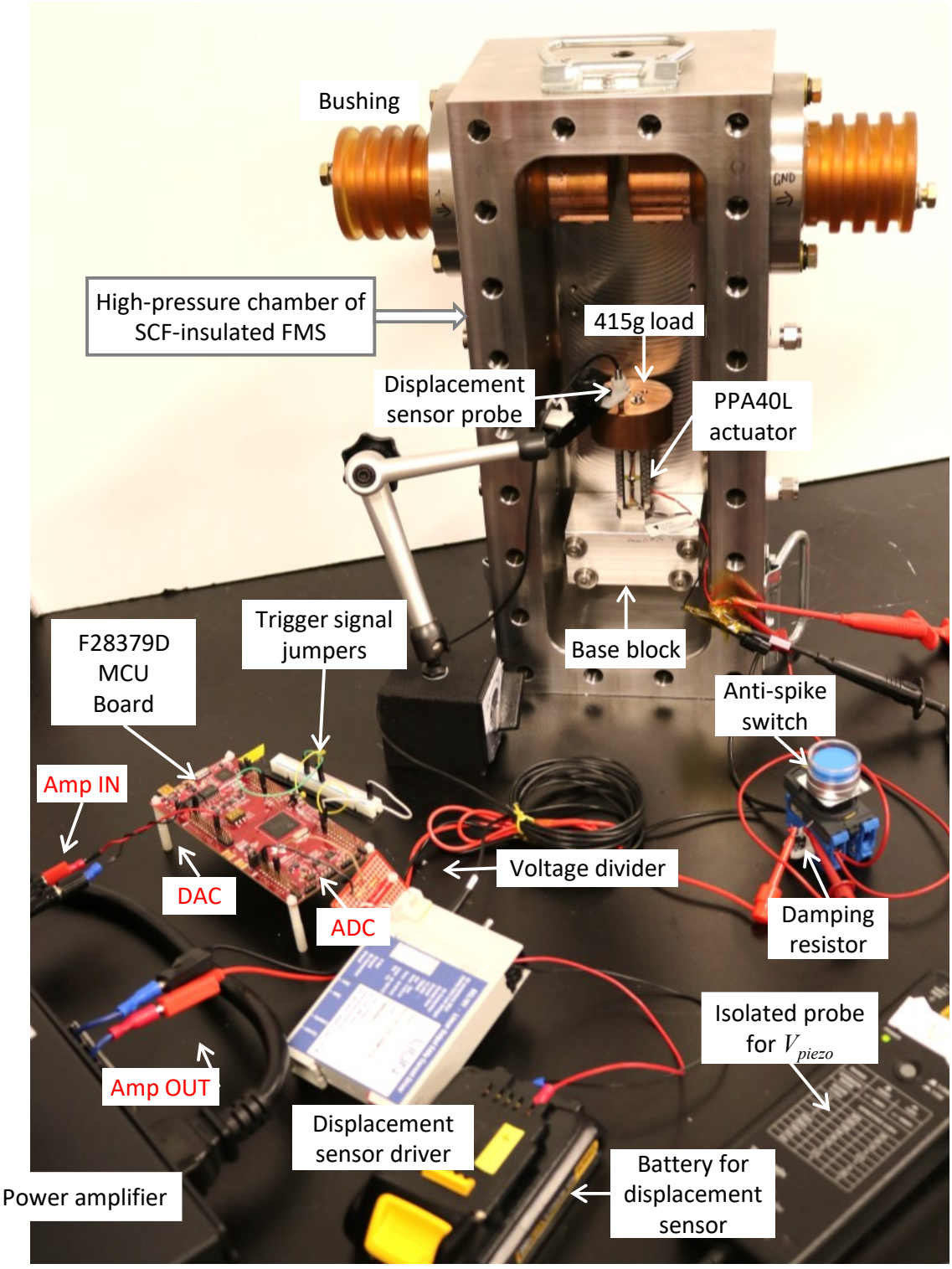

Figure 6.2: Photo of closed-loop test setup with the PPA40L actuator carrying a 415 g load mass with oscilloscope probes connected.

6.1.2 Considerations of the Driving Branch

The driving branch starts from the DAC terminal of MCU board and ends at the PPA40L actuator being driven, with the power amplifier interfacing and isolating the control loop from the power loop as shown in Figure 6.1. The practical considerations in the driving branch include the DAC drive capability, the DAC output voltage range, and an anti-spike switch being added to protect the PPA40L actuator.

The DACs in the F28379D MCU can drive up to 100 pF and 5 kΩ of load. The unbalanced BNC input of power amplifier has about 50 pF of parasitic inductance from terminal to ground, which means the parasitic capacitance of connection wires between the DAC in MCU and the input in power amplifier must be less than 50 pF. A previous mistake made here was using a 1 m long BNC-to-alligator cable to connect the DAC, so the total capacitive load summed up to 95 pF and the DAC signal was significantly distorted. The solution to this problem is simple: a pair of 5 cm long jumper wires are used to connect DAC pins with amplifier input terminal (with BNC-to-banana connector) as shown in Figure 6.2, and the wires are twisted for better noise cancellation.

The linear output voltage range of DACs in F28379D MCU is merely 0.3 V to 3 V. The DACs can generate voltages outside this range from 0.02 V to 3.3 V, but the linearity is not guaranteed due to the buffer limit [103]. Multiplied by the maximum gain of 20 in the power amplifier, the controllable driving voltage range onto the PPA40L actuator is 0.4 V to 66 V with direct DAC signals. If a full driving voltage range of -20 V to 150 V is needed from the same power amplifier, there could be an additional op-amp stage to artificially expand the DAC signal range, such as from 0.3 V $\sim$ 3 V to -1 V $\sim$ 10 V.

A sample op-amp circuit to convert the unipolar DAC signal to bipolar voltage is shown in Figure 6.3. The basic configuration of a summing amplifier can be found in [105], with an additional red LED placed at the output to clamp any excessive negative output beyond -1.6 V. Because the output of op-amp V_{out} could saturate down to negative rail voltage of -12 V when the DAC is disconnected (high impedance to the summing op-amp), which

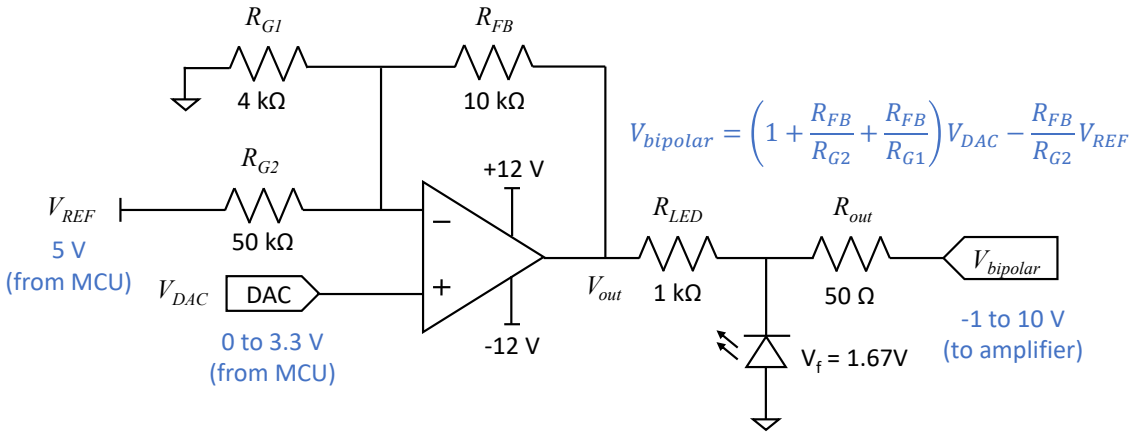

Figure 6.3: Sample circuit to convert the unipolar DAC voltage (0.3 V $\sim$ 3 V) to bipolar output (-1 V $\sim$ 10 V) with linear amplifications.

will lead to a dangerous -240 V driving voltage after the 20 times of multiplication through the power amplifier. To avoid an excessive negative $V_{bipolar}$ value, a red LED with 1.6 V forward voltage is connected with its anode grounded. Once the DAC is disconnected from the non-inverse input of summing op-amp, the red LED starts conducting and keeps a $V_{bipolar}$ output around -1.6 V. The 50 Ω resistor R_{out} is added for impedance matching with subsequent stages, and it can be removed if not necessary.

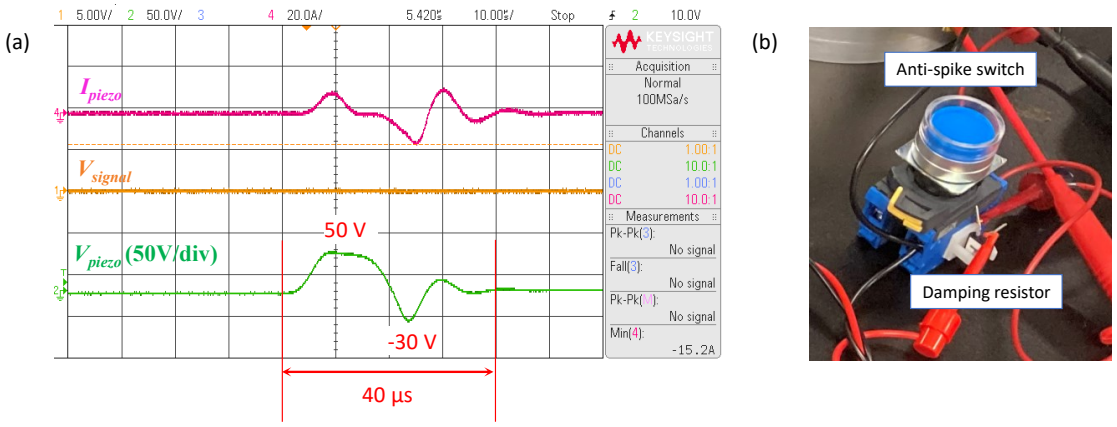

Figure 6.4: (a) The turn-on spike from AE Techron 7224 power amplifier under a capacitive load (like PPA40L actuator). To avoid this fast-transient spike damaging the actuator, an (b) anti-spike switch is used to short out the actuator when turning on the amplifier and reconnect the actuator into the power loop afterwards.

The third practical consideration in the driving branch is closely related with the power amplifier. It is found experimentally that with a capacitive load (like the PPA40L actuator) at the output, this AE Techron 7224 amplifier causes very sharp -30 V to 50 V spikes within a 40 μs duration at the time moment that its output voltage is enabled, although the amplifier input signal stays at absolutely zero as shown in Figure 6.4. These turn-on transients are very disturbing because their negative peak voltage is already below the allowed -20 V driving voltage of PPA40L actuator. Also, the PPA40L actuator generates a high-pitched "clink" sound every time the power amplifier is enabled, meaning that the mechanical deformations are triggered by these turn-on transients in an even higher speed than the desired fast switching motion.

For the purpose of avoiding possible structural damage caused by turn-on transients of power amplifier, a 120 V, 10 A rated push button switch (Figure 6.4(b)) is used to bypass the actuator and let the power amplifier only see a resistive load (the damping resistor) while turning on. This anti-spike switch also provides mechanical support for the damping resistor in the hardware installation.

6.1.3 Considerations of the Sensing Branch

The sensing branch starts from the displacement sensor driver and ends at the ADC pin of MCU. The dominant practical concern in the sensing branch is the mismatch between the displacement sensor driver output range $V_{disp,sen,out}$ and the ADC input range V_{ADC}. The maximum input voltage at MCU pins is 4.6 V [103], but the $V_{disp,sen,out}$ may reach up to 12 V when the sensor probe is off the target. For the purpose of linearly attenuating $V_{disp,sen,out}$ into the safe range of V_{ADC}, a resistive voltage divider with two through-hole resistors is implemented.

The broadband frequency analysis of the added voltage divider had revealed its low-pass filtering functionality experimentally, so a more accurate equivalent circuit of the resistive voltage divider should be Figure 6.5(a). The accuracy of the equivalent circuit is

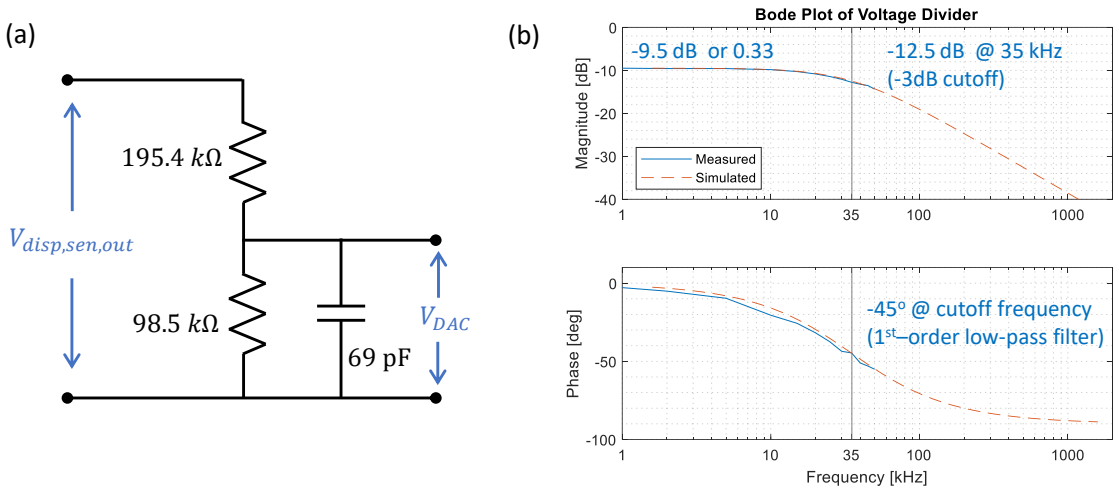

Figure 6.5: Experimentally-determined circuit of the voltage divider and the Bode plot showing its low-pass filtering performance.

confirmed by an experimentally-obtained Bode plot shown in Figure 6.5(b). Although the two through-hole resistors, 195.4 kΩ and 98.5 kΩ, are connected originally as a resistive voltage divider, the final circuit performs like a low-pass filter with 35 kHz bandwidth according to its Bode plot. At low frequencies below 10 kHz, the output voltage V_{ADC} keeps being 1/3 of the input voltage $V_{disp,sen,out}$ with a slight phase delay. Considering the bandwidth of displacement sensor driver is also merely 10 kHz, the constructed voltage divider will not distort $V_{disp,sen,out}$ signal. And its bandwidth of 35 kHz is higher than the maximum 25 kHz frequency sampled by a 50 kHz ADC in MCU. In short, the added voltage divider can properly attenuate the $V_{disp,sen,out}$ signal by 66% to the V_{ADC} signal without significant distortion.

6.1.4 Considerations of the Digital I/O Branch

The third section of MCU hardware setup to be considered is the digital I/O pins, which are also commonly referred as general-purpose I/O or GPIO pins. Different from analog terminals like ADC and DAC in the MCU board that interface with PA peripherals, the digital GPIO ports are responsible for the communication between this MCU and other con-

trollers, such as the main controller for the overall HCB. In the current hardware setup, the GPIO ports receive external trigger signals (like CHARGE and RELEASE in Figure 5.6) to instruct operations of closed-loop controllers and visualize controller status by onboard LEDs for visual indications. Similar to analog ports, there are also several practical considerations in the digital I/O branch designs, especially the anti-floating measures with pull-up resistors and the anti-bouncing measures with GPIO input qualifications.

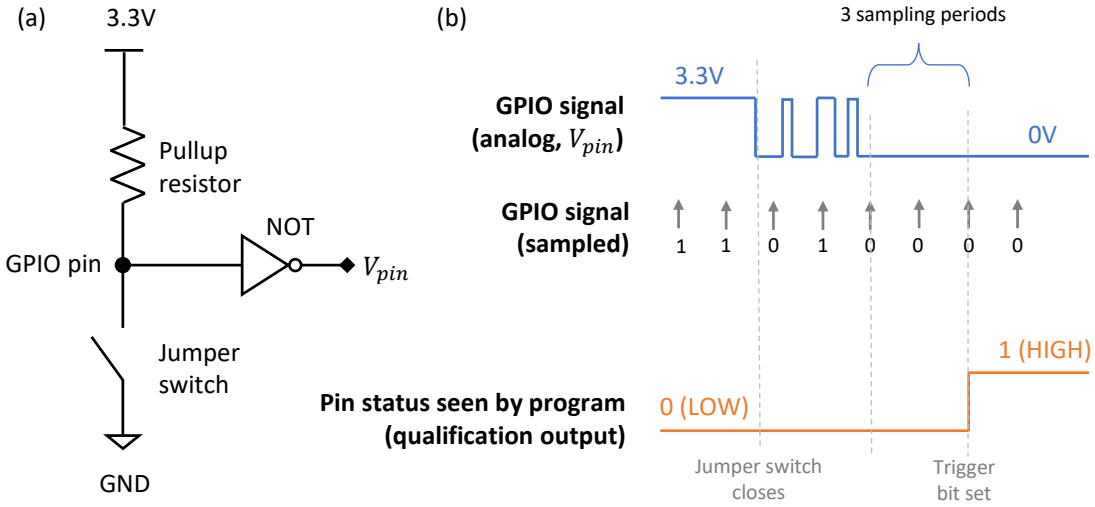

Figure 6.6: Illustrations of digital I/O pin settings in F28379D MCU board. (a) shows the pull-up resistor and the inverted GPIO reading by the NOT gate, (b) shows the working principle of GPIO input qualification with 3 sampling periods.

It is found experimentally that using a hardware component to issue trigger signals, such as pushing a button or switching a jumper wire, would be inevitably entangled with input floating and input bouncing problems. The input floating problem happens when a digital input pin is not connected with any defined voltage potential (i.e. floating). If the program reads the status of a floating pin, the GPIO pin value will become undefined and unreliable. The solution to this pin-floating problem is very straightforward: enable the internal pullup resistors connected to GPIO pins in the MCU board. Figure 6.6(a) illustrates a digital input pin with a pullup resistor and an input NOT gate. Before closing the jumper switch to GND, the GPIO pin is always hooked up to 3.3 V potential through the board-

internal pullup resistor, so the pin status V_{pin} keeps being '0' after the NOT gate, no matter whether the pin is physically connected to any non-zero voltage potential or just floating in the air. Once the jumper wire is switched to zero, the pin potential is clamped down to zero and the pin status V_{pin} changes to '1' definitely. In short, enabling pullup resistors on GPIO pins can solve the floating pin problem and let the program read the pin status correctly.

Even though the program can read the pin status correctly with pullup resistors, the GPIO pins could be physically unstable once disturbed by the input bouncing problem, especially when using a push button to trigger. As illustrated in Figure 6.6(b), a bouncing button will cause the analog voltage on GPIO pin to glitch. The sampled digital pin status may bounce back and forth between '0' and '1'. If the program is edge-triggered by this GPIO pin, there could be multiple triggers being issued when the button is manually pushed once. Instead of physically dampening the button in hardware, it is easier to debounce the V_{pin} signal by prolonging the input qualification period. For example, waiting for 3 sampling periods of the same sampled values before outputting the pin status to the program. So that the pin status as seen by the main program keeps being '0' even though the analog voltage on the pin hits 0 V temporarily during the bouncing period. In short, setting input qualifications on GPIO pins can solve the input bouncing problem and let the program read the pin status once it settles.

6.2 Results from the Closed-Loop Controller Tests

6.2.1 Test Settings and Driving Signals

In all hardware implementation tests presented in this chapter, the PPA40L actuator was constantly loaded with the 415 g copper mass during actuation. Considering the hardware constraints in the closed-loop test setup, all the proof-of-concept tests presented in this section were performed at reduced voltage levels. A set of test waveforms shown in Figure 6.7 is provided as the example for controller test settings. Channel 1 of oscilloscope was V_{DAC}, which was the DAC output of MCU board and also the input signal to the power

amplifier. After 20 times of amplification through the power amplifier, the driving voltage measured at terminal leads of PPA40L actuator was V_{piezo} at channel 2 of the oscilloscope. Different from the 0 to 150 V driving voltage range used in previous sections, with a 3.3 V MCU board as the signal source, the driving voltage range was limited within 0 - 66 V in all MCU-controlled tests. And the expected maximum displacement of actuator in closed-loop hardware implementation tests was also down-scaled from 44 μm at 150 V to 15 μm at 51 V driving voltage.

The desired displacement x_d was set to 0 μm before t_1 as shown in Figure 6.7. Then the reference displacement input x_d was ramped up from 0 μm up to 15 μm linearly within 10 ms (t_1 to t_2), and held constant at 15 μm for 30 ms (t_2 to t_3). Next, the switching-off process happened from t_3 to t_4 when the x_d dropped from 15 μm down to 5 μm within a tail time t_{tail} of 1 ms. Similar to the tail time definition in open-loop tests in Chapter 3, the tail time t_{tail} used in this chapter referred to the time duration from the high input level (x_{max} in x_d) to the low input level (x_{min} in x_d). After t_4, the reference input x_d was kept constantly being at 5 μm. This above-zero steady-state position of 5 μm was set on purpose, so that the driving voltage V_{piezo} had the 0 - 17 V reserved space for active damping. If the steady-state position were set at 0 μm, the MCU could not output a negative DAC voltage to actively instruct the actuator moving against vibration.

The channel 3 of oscilloscope of Figure 6.7 was the output voltage of displacement sensor driver $V_{disp,sen,out}$, whose probe was connected in the reverse direction from open-loop test setup to keep uniform ground reference on GND1 (Figure 6.1). A falling $V_{disp,sen,out}$ meant the actuator was expanding to 15 μm displacement during t_1 and t_2, while a rising $V_{disp,sen,out}$ meant the actuator was shrinking from 15 μm displacement down to 5 μm during t_3 and t_4.

The channel 4 of oscilloscope in Figure 6.7 was the voltage representation of desired displacement V_d. It was calculated by $V_d[V] = x_d[\mu m] * 8000[V/m] + 0.02[V]$ in the controller code, and then outputted at the second DAC (DAC2) terminal in the MCU board.

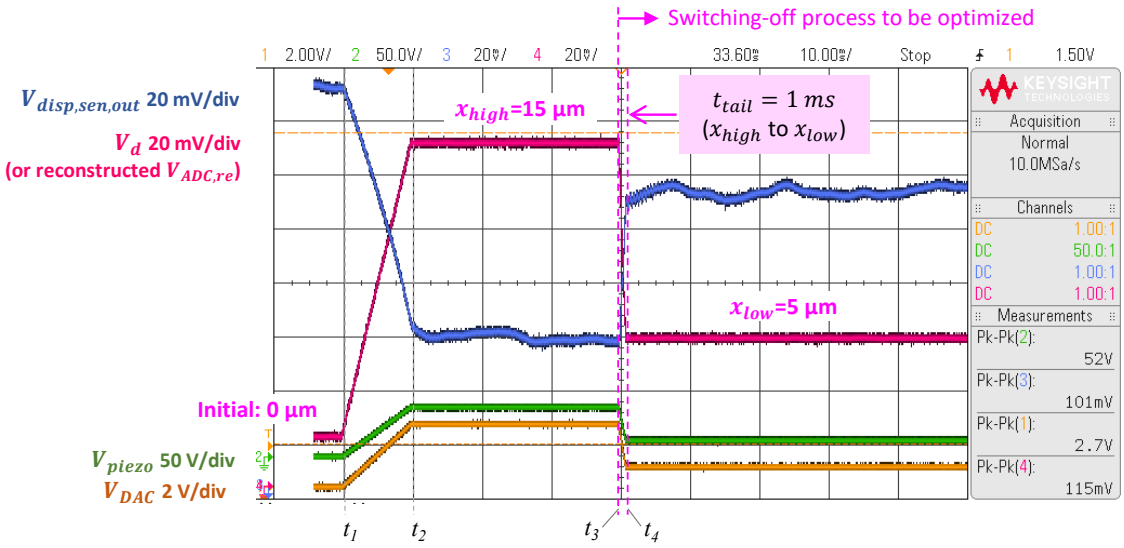

Figure 6.7: Examples of the driving signals for controller implementation tests. The curves were measured during a MCU-controlled open-loop PA actuation test under t_{tail} = 1 ms.

The 8000 V/m was the sensing ratio of the displacement sensor and the V_d could be compared with $V_{disp,sen,out}$ during t_2 and t_3 to see the magnitude of steady-state displacement error. The 0.02 V was added as the voltage bias to lift V_d curve up above the 0.02 V minimum output of DAC in MCU. In this way, the time moments of turning points, i.e. t_1, can be matched visually in oscilloscope screenshots. Sometimes, the DAC2 terminal outputted the reconstructed ADC voltage $V_{ADC,re}$ as measured at the channel 4 of oscilloscope, such as in Figure 6.8 below. The "reconstructed $V_{ADC,re}$" meant it was not the real input voltage at ADC terminal of MCU V_{ADC} shown in Figure 4.2, instead, it was calculated by $V_{ADC,re}[V] = x_{ADC}[\mu m] * 8000[V/m] + 0.02[V]$. Considering the x_{ADC} was calculated by $x_{ADC} = (V_{base} - V_{ADC})/8000/K_{divider}$, so the reconstructed $V_{ADC,re}$ was a representation of x_{ADC} for easy demonstration through oscilloscope screenshots.

6.2.2 Low-frequency Vibration Attenuation

As classified in Chapter 3, the vibration observed from open-loop travel curves could be divided into a high-frequency component characterized by the vibrational dynamic model) and a low-frequency component (external disturbances that cannot get represented by a

vibrational dynamic model). Without a well-characterized model, this low-frequency vibration could still be attenuated with a fast-enough PI controller in the loop, such as using a 50 kHz control update rate for a 170 Hz vibration as in Figure 6.8.

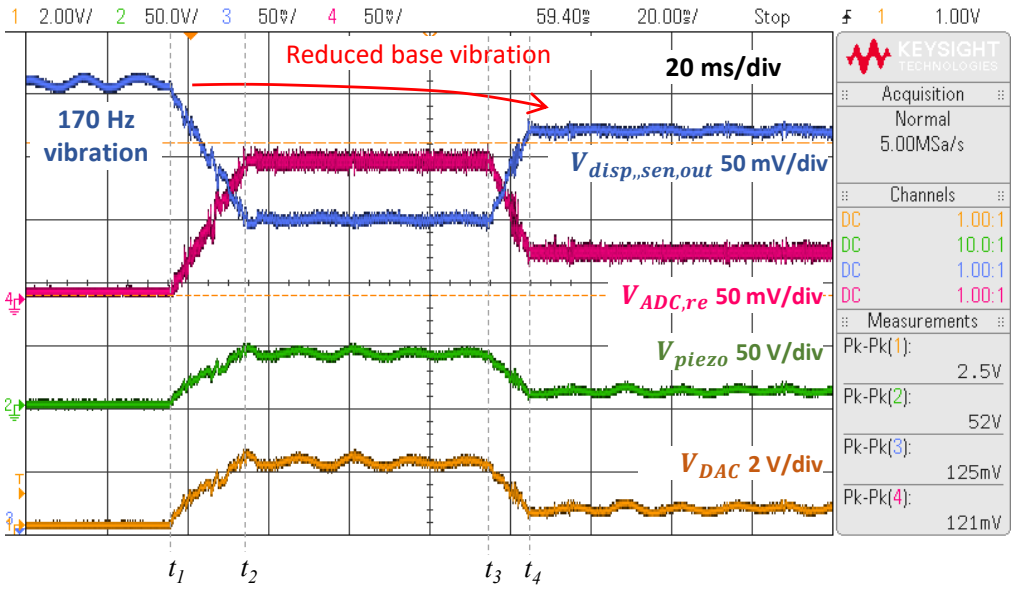

Figure 6.8: Attenuation on low-frequency vibration with a PI controller in the closed-loop system.

The time durations of switching-on and holding-at-high process in Figure 6.8 were doubled from the ones used in Figure 6.7, and the tail time t_{tail} in x_d was elongated to 10 ms so that the high-frequency vibration were avoided as much as possible under these slow actuation process. Also, the channel 4 of oscilloscope read reconstructed $V_{ADC,re}$ from DAC2 in MCU. Besides the above changes in signal time durations and channel 4, the other controller settings kept the same with ones defined in Figure 6.7.

The successful low-frequency vibration attenuation had been demonstrated in Figure 6.8. Before the closed-loop PI controller started at t_1, the peak-to-peak amplitude of 170 Hz vibration was 2 μm. This vibration amplitude was reduced right after the PI controller was started, reaching a 0.5 μm peak-to-peak value after the switching-off was finished at t_4. Without any vibration model, this attenuation was achieved by the PI controller instruct-

ing the driving voltage V_{piezo} to vibrate against the external base vibration. As shown in Figure 6.8, both V_{DAC} and V_{piezo} were sinusoidally vibrating in a similar frequency but opposite phase as the base vibration in $V_{disp,sen,out}$. Thus, the resulting movement of actuator's load top was held at a relatively constant position with reduced vibration amplitude, just like the simulated performance as shown in Figure 5.10.

6.2.3 High-frequency Vibration Attenuation

For the high-frequency vibration that was generated from internal vibrational nonlinearity of the PA, using only a PI controller in the loop could attenuate them, but the resulting travel curves were too slow to qualify as a "ultrafast switching" in PA-FMS applications as demonstrated by simulations in previous chapters (Figure 5.10). An active damping filter like a notch or lag filter was added into the switching motion controllers, and the three closed-loop switching motion controllers being implemented in hardware were: PI controller only, PI controller with a notch filter, and PI controller with a lag filter. The comparisons of experimentally obtained travel curves among these three closed-loop controllers (plus open-loop method) can demonstrate their pros and cons in practical situations.

The desired displacement was kept at the same 0-15-5 μm in high-frequency vibration attenuation tests. Similarly, the voltage settings and most time duration settings were kept the same with low-frequency vibration attenuation tests. The major difference was that a much shorter tail time t_{tail} in x_d was used in high-frequency vibration attenuation tests, such as 140 μs, 240 μs and 500 μs, so that the vibration nonlinearity of actuator could dominate the travel curves after the switching-off.

The controller parameters of three closed-loop strategies for hardware tests are given in Table 6.1. Both PI controllers and notch/lag filters were started with MATLAB-tuned parameters given in Figure 5.10, then slightly tuned by changing parameter values in the CCS program during hardware tests, and finally reached the best damping performance with parameters given in Table 6.1. By comparing the MATLAB-tuned controller parameters

Table 6.1: Comparisons on the damping filter transfer functions after the MATLAB tuning and after the in-lab hardware tuning.

	MATLAB Tuned	**Hardware Tuned**
PI Only	$0.01\frac{z+1}{z-1}$	$0.009\frac{z+1}{z-1}$
PI + Lag Filter	$0.01\frac{z+1}{z-1}\frac{z-0.85}{z-0.97}$	$0.009\frac{z+1}{z-1}\frac{z-0.85}{z-0.95}$
PI + Notch Filter	$0.303\frac{z-0.7}{z-1}\frac{z^2-1.922z+0.966}{z^2-1.719z+0.757}$	$0.22\frac{z-0.7}{z-1}\frac{z^2-1.924z+0.977}{z^2-1.745z+0.793}$

with the final hardware-tuned ones, the changes made in the notch-filtered controller were more significant. There was only a 10% reduction in the proportional gain in the PI-only controller and the lag-filtered controller, while the notch-filtered controller needed about a 30% reduction to stabilize the system. Besides, the notch filter also needed a 10% change in notch frequency from 1680 Hz to 1850 Hz to minimize small noise in notch-filtered travel curves under switching off (small noise to be illustrated in Figure 6.9(c)), while the parameter change for the lag filter was merely 2%.

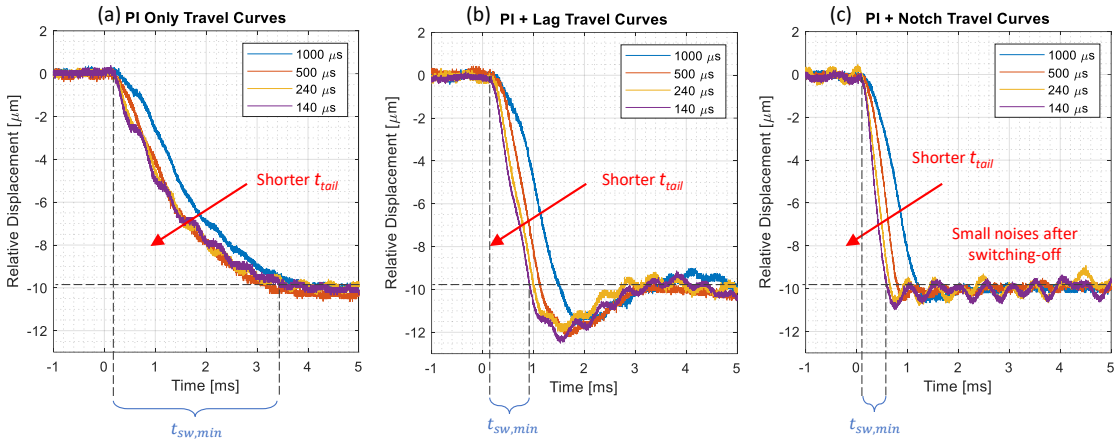

Figure 6.9: Experimental travel curves controlled by three closed-loop control strategies under different tail time t_{tail} in the reference input trajectory x_d, which are grouped by the type of switching motion control strategy.

By reducing the tail time t_{tail} in the reference input trajectory x_d from 1 ms down to 140 μs, the switching-off time t_{sw} in closed-loop controlled actuations could be shortened accordingly. As shown in Figure 6.9, the t_{sw} was the time duration between the time

Table 6.2: Comparisons on experimental performance of switching motion control strategies at t_{tail} = 140 μs.

Strategy	**Switching** t_{sw}	**Settling** t_{settle}	**Undershoot**
Open-loop	235 μs	9.14 ms	53%
PI + notch	595 μs	4.92 ms	9%
PI + lag	855 μs	3.73 ms	6%
PI only	3874 μs	3.14 ms	0%

moment that the actuator top left the initial position (0 μm), and the time moment that the actuator top first hit the steady-state position (-10 μm). For travel curves under PI-only control strategy in Figure 6.9(a), their t_{sw} values stayed about 3 to 4 ms, no matter the input tail time t_{tail} was 140 μs or 1 ms. This slow response or limited bandwidth in a PI-controlled system was directly caused by the existence of resonance peak in the closed-loop system, and the lack of loop shaping components like notch and lag filters to increase system bandwidth.

After adding a lag filter into the closed-loop system with a PI controller in Figure 6.9(b), the output travel curve could track the desired input trajectory x_d better, with an obviously reduced t_{sw} in output travel curves at a lowered t_{tail} in reference input. The minimum t_{sw} achieved in a lag-filtered system under 140 μs t_{tail} was below 1 ms. Compared to lag-filtered system, the notch-filtered system with a PI controller in Figure 6.9(c) could track the input x_d even faster, with a minimum t_{sw} being down to 0.5 ms under 140 μs t_{tail}. At the same time, there was more irregular noise existed in notch-filtered travel curves after the switching-off process than the other two groups of travel curves. The after-switching noise in lag-filtered travel curves was smaller in magnitudes, and the PI-filtered travel curves were almost free from small noise. The effects of the low-amplitude noise in a larger collection of travel curves will be discussed with reference to Figure 6.10.

The attenuation of high-frequency vibration that dominated fast-switching travel curves was demonstrated in Figure 6.10, with closed-loop travel curves under PI-only, PI with

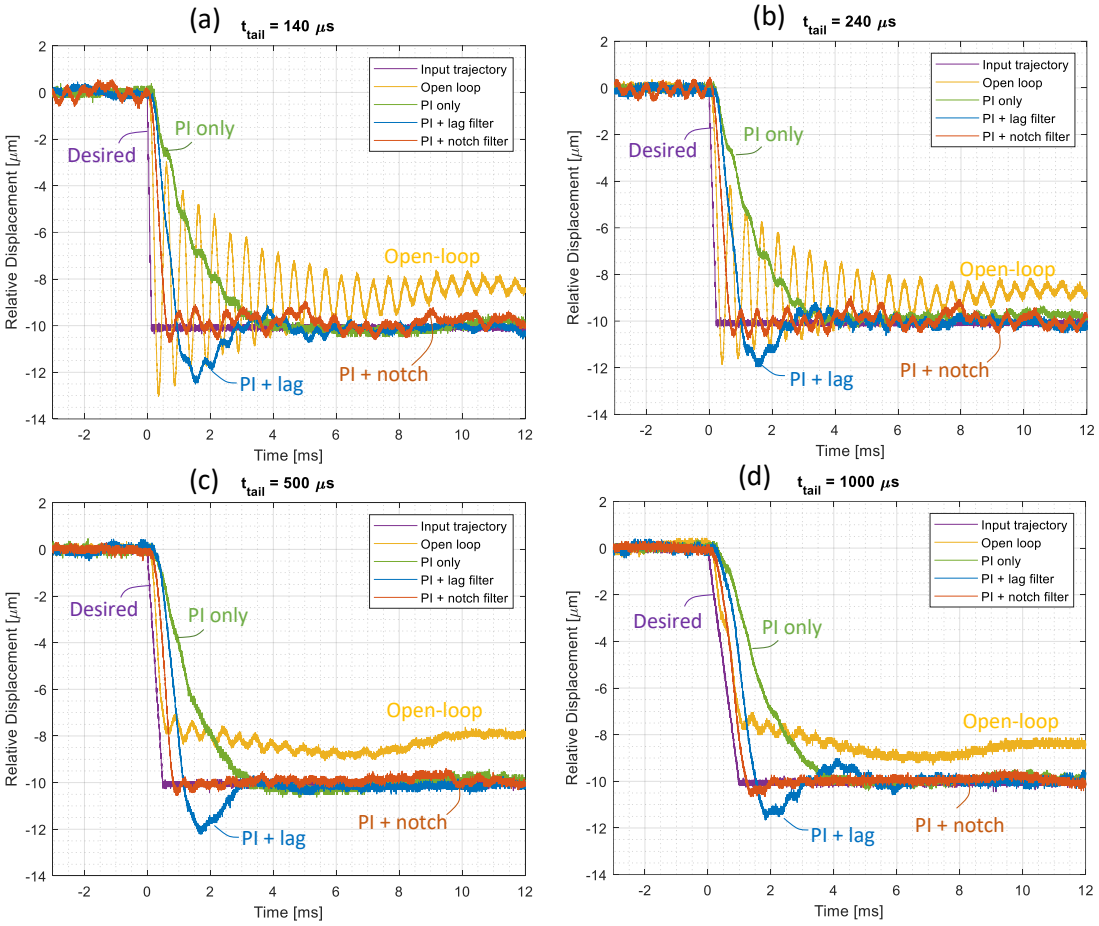

Figure 6.10: Comparisons on experimental travel curves from three closed-loop control strategies and open-loop control under different tail time t_{tail} in the input trajectory x_d.

lag, and PI with notch strategies compared to open-loop travel curves. As shown in Figure 6.10(a)(b), the vibration in open-loop travel curves was substantial even in this down-scaled 15 μm to 5 μm actuation range. Moreover, when the vibration was less dominant in slow actuations like Figure 6.10(c)(d), the steady-state displacement mismatch of 1.7 μm from desired trajectory x_d became more obvious. And this steady-state error had degraded the tracking accuracy of actuator movements.

The problem of steady-state trajectory-tracking error had been solved with a PI controller in the loop. As shown in all sub-figures of Figure 6.10, the PI-only controlled travel curves reached the full 10 μm displacement range after 3 ms, and staying on the steady-state position steadily with the almost-zero undershoot and overshoot. This complete elimination of both steady-state error and vibration in travel curves had accomplished most of the control expectations, except the switching time t_{sw} requirement. Therefore, a PI controller was included in all switching-motion control strategies as the baseline solution.

On top of PI controller performance, the travel curves modified by a notch filter or a lag filter had exhibited faster switching speed as shown in Figure 6.10, after trading-off a part of overshoot and undershoot performance. By evaluating the amplitude of remnant noise in travel curves after the switching-off process, the notch-filtered system seemed less stable than the lag-filtered system under ultrafast actuations. For example, the notch-filtered travel curve in Figure 6.10(a) had an undershoot of 9% because of the displacement sag around 5 ms. Comparatively, the lag-filtered travel curve in Figure 6.10(a) hit an undershoot of 6% early at 4 ms and kept within ± 5% error band afterwards.

Careful analyses of the low-level noise in travel curves of Figure 6.10(a)(b) revealed that these disturbances were irregular and undetermined like some "white noise" triggered by fast actuations. Also, the amplitude of the small noise was already attenuated after changing the notch frequency from 1680 Hz to 1850 Hz (Table 6.1) to accommodate real-world conditions. On the other hand, even though the lag-filtered travel curves also had distinguishable ripples, the ripples were relatively minor compared to the inevitable over-

shoot and undershoot patterns shared by all lag-filtered curves under both fast and slow actuations. Not much hardware tuning effort was needed on the lag filter (only 2% change) to achieve the optimal performance of the vibration attenuation. Therefore, although the notch-filtered travel curves had smaller t_{sw}, the lag-filtered travel curves were free of uncontrolled noise and thus keeping better system stability after the switching-off process.

The key characteristics of vibration-damped travel curves obtained from proof-of-concept tests under 140 μs actuation are generalized in Table 6.2. In summary, to achieve as fast as possible switching process in a PA-FMS, a notch filter with a PI controller is the first choice for critically-damped closed-loop control. But the tuning of the notch filter must continue into hardware tests to eliminate random noise that are hard to get captured in the vibrational dynamic model of PA. If the undershoot of notch-filtered travel curves fails to meet insulation strength expectations in the PA-FMS, a lag filter is a backup choice after trading-off part of the switching time of travel curves. The other two strategies, only the PI controller or a PI controller with a lead filter, have been confirmed as too slow to get implemented in fast switching operations of PA-FMS, although their overdamped travel curves had almost zero overshoot and undershoot after switching-off.

6.3 Comparison with Existing PA Control Strategies

Table 6.3 presents the comparisons between achieved switching travel curves in this paper with reported step responses and controller bandwidth in representative publications. It is clear that the proposed switching motion controller (PI + notch type) has used only 10% of a common rise time to move a double-weighted load for reaching a similarly long travel distance. At the same time, the vibration is well-confined with less than 10% of overshoot and undershoot. Therefore, the significance of proposed switching motion control strategies has been validated by internal comparisons with open-loop scenarios and external comparisons with representative PA control studies in literature.

Table 6.3: Comparisons on switching motion performance of the proposed control strategy (PI + notch) with the reported PA control methods in literature.

Reference	Displacement [μm]	Load [g]	Response Speed / Bandwidth
[16]	7.8	250	t_{rise}=6ms, t_{settle}=15ms
[14]	25	4	t_{settle}=6ms, overshoot=20%
[11]	2.5	102	f_{BW}=2070Hz
This study	10	500	t_{sw}=0.6ms, t_{settle}=5ms, f_{BW}=1760Hz,undershoot=9%

6.4 Comparison with Travel Curves from Thomson Coil Actuators

Besides the reduced overshoot and settling time, the significance of proposed switching motion controller for the overall PA-FMS can also be revealed by comparing to the reported Thomson coil-actuated FMS travel curves in literature. A closed-loop PA travel curve under t_{tail} = 500 μs (PI controller with notch filter) is normalized in Figure 6.11 for profile comparisons with travel curves reported in Thomson coil-actuated FMS, which also have their displacement ranges normalized to [0, 1].

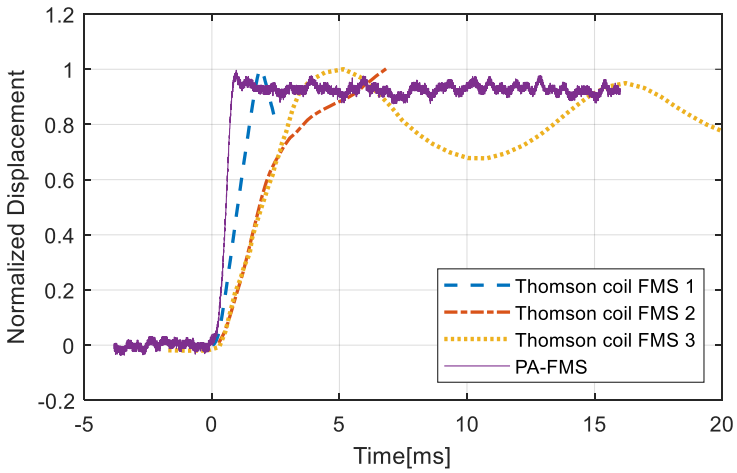

Figure 6.11: Comparisons on normalized displacements of PA-FMS with reported travel curves of Thomson coil-actuated FMS in literature [7, 27, 106].

As shown in Figure 6.11, the closed-loop controlled travel curve of PA-FMS is the

closest to critical damping with the fastest speed and the smallest overshoot or undershoot. The travel curves from Thomson coil actuators are still oscillatory and slow even after a gas damper [27, 106] or a closing coil [7] has been used. Therefore, although Thomson coil-actuated FMS give much higher travel distances like 30 mm in [27, 106] and 10 mm in [7], PA-FMS can give faster switching operations with more damped travel curves than most Thomson coil-actuated FMS. Benefited from its vibration-free travel curves, a PA-FMS can accommodate advanced HCB control strategies to better protect MVDC systems like the sequential tripping technique.

6.5 Chapter Summary

This chapter presents the closed-loop experimental setup for hardware implementation tests on proposed switching motion controllers. The practical considerations are discussed on DAC voltage limit, voltage divider characteristics, digital I/O input qualifications and pull-up resistor settings. Due to hardware limitations, a smaller displacement range of 15-5 μm was used in closed-loop tests, which was down-scaled from the 44-0 μm travel range achieved in open-loop tests. Although the travel range had been reduced, these proof-of-concept tests still demonstrated the vibration attenuation performance with four switching motion control strategies.

Comparatively, the switching motion controller with a PI controller and a notch filter achieved the fastest switching operation among all closed-loop strategies, but its undershoot value was also the highest due to irregular noise triggered under ultra-fast switching-off movements. If the undershoot value of the notch-filtered system fails to meet expectations of insulation strength in PA-FMS, the damping filter can be changed to a lag filter for a smaller undershoot and a smaller settling time, after prolonging the switching time by 40%. Finally, The notched-filtered switching motion controller of PA-FMS has been compared with published PA control strategies to demonstrate its outstanding performance. A notch-filtered PA travel curve is compared with Thomson coil-actuated travel curves in literature.

CHAPTER 7
DRIVING HARDWARE IMPROVEMENTS FOR ACCELERATED PIEZOELECTRIC ACTUATION

In this chapter, the power-amplifier-based driving hardware will be improved to facilitate ultrafast piezoelectric actuation. The first improvement is using a quadrant-shifting method to achieve a higher current-sinking capability in the driving hardware. With the quadrant-shifting method, the PA can be discharged within a shorter period of time, and the contact actuations inside a PA-FMS can be accelerated. The discussions on the driving hardware improvement come from the driving problems in PPA120XL tests, in which the PPA120XL actuator cannot achieve the targeted switching speed due to the limited driving capability of the power amplifier. The proposed solution to the PPA120XL driving problem is a specific design based on the general quadrant-shifting method that may apply to different piezo drivers. The second improvement uses the different driving hardware to accomplish sequential triggering of individual stacks inside a multi-stack PA. With the sequential-triggering method, the deformation speed of piezoelectric stacks can match the propagation velocity of stress waves inside the piezoceramic.

7.1 Four-Quadrant Operation of Power Amplifiers

The quadrant-shifting method is proposed for two-quadrant or four-quadrant power modules, including power amplifiers and power supplies. The output characteristics of a four-quadrant power module are illustrated in Figure 7.1(a) with the current scale on the horizontal axis and the voltage scale on the vertical axis. The first quadrant (Quadrant I) is the region where most power modules are rated, in which the power module will output a positive voltage ($V_{amp} > 0$) and a positive current ($I_{amp} > 0$) as illustrated in the amplifier output convention of Figure 7.1(b). If a power module can output a positive voltage

($V_{amp} > 0$) and a negative current ($I_{amp} < 0$), that is, this power module sinks the current from its load and the Quadrant II is entered. Working in Quadrant I & II is the capability shared by two-quadrant power modules, but they cannot safely operate in Quadrant III or Quadrant IV with a negative output voltage ($V_{amp} < 0$). The power modules that can safely operate in all four quadrants are referred to as the four-quadrant power modules, such as the AE Techron 7224 power amplifier used in this study.

Given the safe operations in all four quadrants, a four-quadrant power module could have asymmetrical operation limits in different quadrants. As illustrated in Figure 7.1(a), the negative limits of voltage and current can be smaller than the positive limits with $|I_{min}| \leq |I_{max}|$ and $|V_{min}| \leq |V_{max}|$. Then a problem will occur if a larger negative current limit is needed from the power module than the positive current limit, that is, $|I_{min}| > |I_{max}|$. This requirement for a larger negative current limit exists in the PA operations within the PA-FMS of this study, which counteracts with the inherent output current limits of the AE Techron 7224 power amplifier with -25 A for I_{min} and 40 A for I_{max} being used in this study.

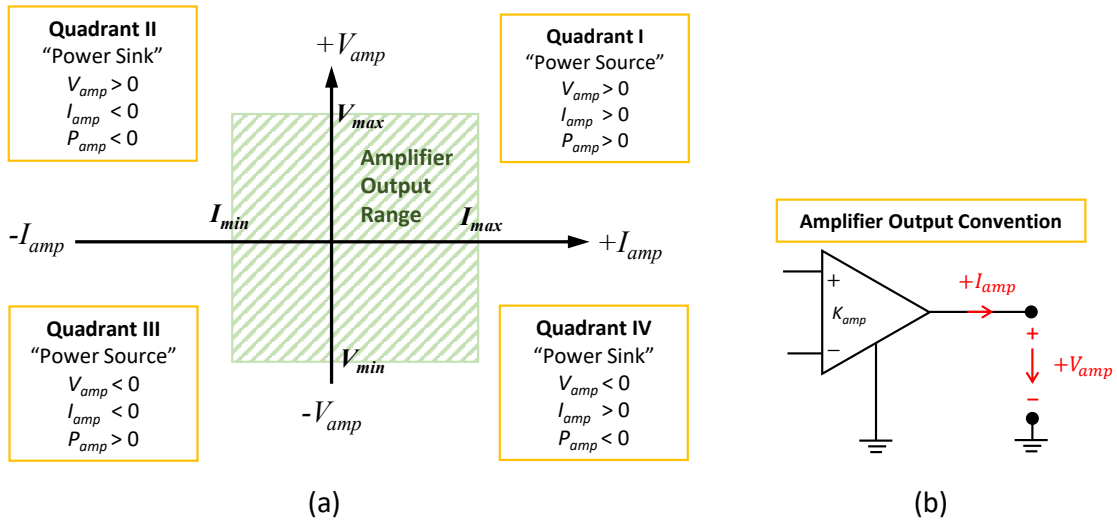

Figure 7.1: Illustration of (a) output characteristics and (b) output convention in a four-quadrant power module.

7.2 Quadrant-Shifting Method

In order to achieve a higher negative current output from a power module like AE Techron 7224 power amplifier, a general method to shift the operational quadrants horizontally between Quadrant I and II is developed. This quadrant-shifting method can be widely applied to other kinds of voltage-controlled power modules with one-, two- or four-quadrant operation capabilities. Because only the current output characteristics of a power module get modified like in Figure 7.2(a) and the internal structure of the power module stays unchanged. The conceptual circuit for achieving the horizontal-quadrant-shifting is shown in Figure 7.2(b).

As shown in Figure 7.2(b), a current shift source is added in parallel to the output of a voltage-controlled, four-quadrant power amplifier. The amplifier works in the voltage-controlled mode so that its terminal voltage V_{amp} is under control while its terminal current is changing. For the purpose of shifting the driving output range leftward along the current axis, the current shift source is set to draw a current I_{css} flowing from the amplifier terminal to the ground. Therefore, the total output current of driving hardware (power amplifier and current shift source) is:

$$I_{out}(t) = I_{amp}(t) - I_{ccs}(t) \tag{7.1}$$

By increasing the peak value of I_{ccs}, the negative limit of the output current $I_{out,min}$ can be shifted leftward to a smaller value as illustrated in Figure 7.2(a). Although the positive current limit of the output current $I_{out,max}$ is reduced accordingly, the influence could be minimized by selecting the correct time moment to introduce the current shift source into the circuit. An example of selecting the proper time moments for the current shifting operations will be presented in the next subsection.

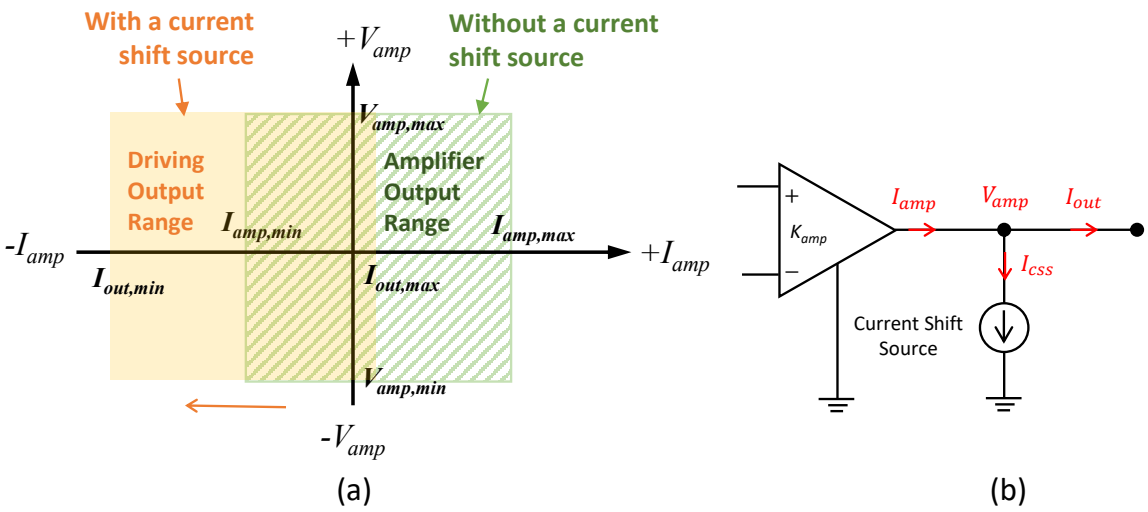

Figure 7.2: Illustration of (a) horizontal-quadrant-shifting method for a four-quadrant power amplifier. This quadrant-shifting can be achieved in (b) the conceptual circuit with a current shift source at the output of power amplifier.

7.3 Accelerated Driving for the PPA120XL Actuator

In this section, the proposed quadrant-shifting method is implemented to accelerate the driving speed of the PPA120XL actuator. The existing problem is first distinguished when using the power amplifier itself to drive the PPA120XL actuator . Next, the current-chopped load curve of PPA120XL actuator during actuation processes is illustrated to show the limited driving capability of the power amplifier in Quadrant II operations. Finally, the quadrant-shifting branches are designed with MOSFETs and resistors for accelerated discharging processes in the PPA120XL actuator.

7.3.1 Limited Driving Speed for PPA120XL Actuator

The controller development process of the PPA120XL controller meets more practical issues than the controller development for the PPA40L controller. Moreover, these practical problems come as early as in the first step on open-loop travel curve measurements, where the PPA120XL actuator cannot achieve targeted speed due to the limited driving capability of the power amplifier. Although the driving capability of the power amplifier can be

boosted by cascading more modules or using a more powerful amplifier, the compactness of the overall PA-FMS system will be reduced in this way further. An alternative solution is to add a parallel discharge branch in the power circuit to accelerate the driving process of the PPA120XL actuator, so that a smaller piezo driver can be used to boost the compactness and power density of the overall PA-FMS system.

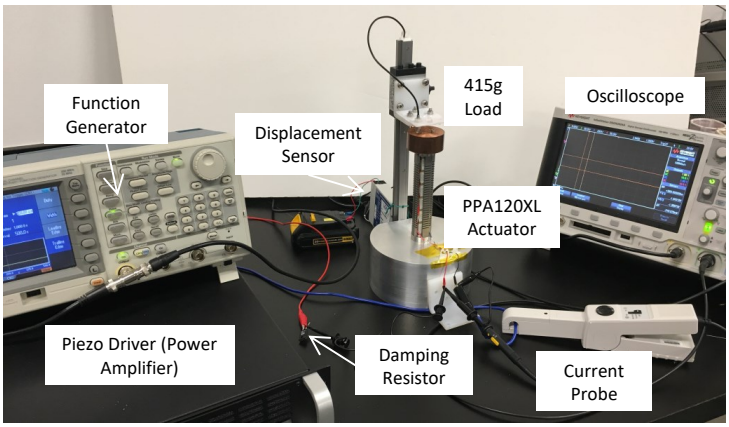

Figure 7.3: Test setup to measure the open-loop actuation performance from the PPA120XL actuator (no closed-loop controller) based on the same open-loop schematic in Figure 3.1. The piezo driver is an AE Techron 7224 model power amplifier.

The open-loop actuation performance of the PPA120XL actuator was measured using the setup in Figure 7.3. Implementing the same circuit as for the PPA40L actuator open-loop tests (Figure 3.1), the power amplifier (used as the piezo driver) received trigger signals from a function generator. The power amplifier also outputted 0 - 150 V voltage to drive the PPA120XL actuator with a 1 Ω damping resistor in the power loop. The PPA120XL actuator was physically mounted onto an aluminum base block of approximately 3.5 kg of mass. It carried a 415 g load mass resembling the total mass of contacts, contact plate and insulator in the PA-FMS prototype. The current flowing from the negative terminal of the PPA120XL actuator to the negative output of the power amplifier was measured by a current probe (Keysight 1146B, DC to 100 kHz). All the signals from function generator, power amplifier, displacement and current probe were collected and displayed together in the oscilloscope.

A new problem that had not been observed in PPA40L tests was the chopped driving current I_{piezo} through PPA120XL actuator while the tail time t_{tail} of function generator signal was reduced. This chopped current had excited the unwanted disturbance in travel curves d_{piezo}. As shown in Figure 7.4(a), a normal actuation of the PA was accompanied by a triangular-shaped I_{piezo} curve with a sharp peak down to -25 A, with 400 μs of t_{tail} in V_{signal} from function generator. When the t_{tail} dropped from 400 μs to 300 μs with all other parameters stayed the same, a period of uncontrolled disturbances occurred in the d_{piezo} of Figure 7.4(b). At the same time moment when the d_{piezo} disturbance started, the I_{piezo} was chopped from -23 A to -19 A, and the driving power P_{piezo} reached its peak value at 1.93 kW. Therefore, it was very likely that the disturbed slope in d_{piezo} was caused by the current chopping-off event from the power amplifier.

(a) Normal output
current slew rate = 25A/500µs
$t_{tail} = 400\mu s$

(b) Current-chopped output
current slew rate: 23A/250µs
$t_{tail} = 300\mu s$

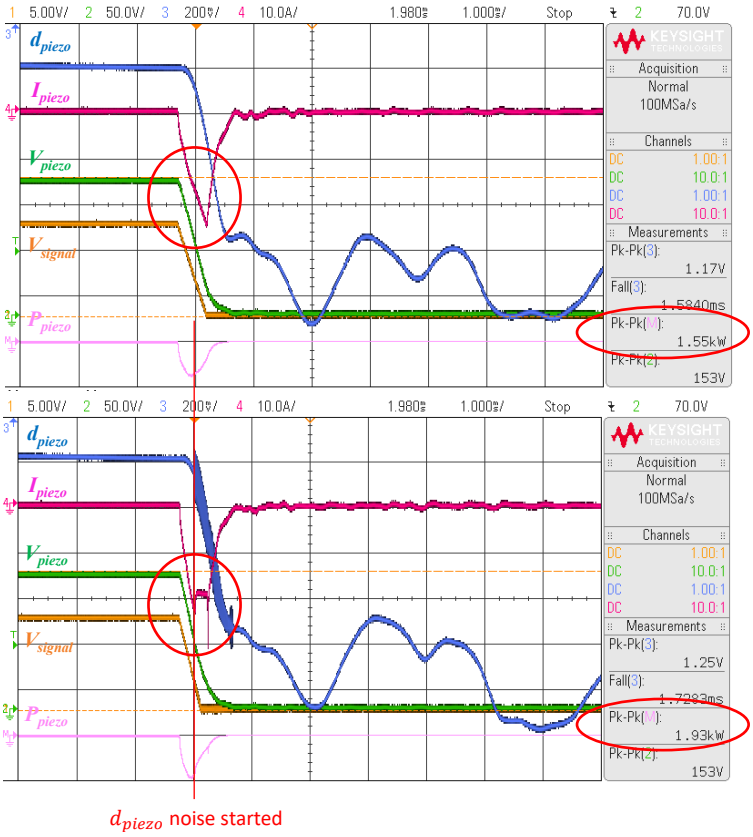

Figure 7.4: Experimental travel curves d_{piezo} of the PPA120XL actuator; (a) the driving current I_{piezo} was normal under a small slew rate (-25A/500μs), (b) the I_{piezo} was chopped off by power amplifier output limits under a large slew rate (-25A/250μs).

After several rounds of tentative tests with different V_{piezo}, t_{tail} and m_{totoal} values, it was found that the current chopping was more likely to happen at a higher slew rate dI_{piezo}/dt, instead of a higher absolute value of current I_{piezo} or driving power P_{piezo}. As given in Figure 7.4, the normal actuation had a peak current of -25 A, but the linearized current slew rate was only 0.05 A/μs; while the current in the noisy actuation situation got chopped before it reached -25 A, and it slewed at an almost doubled rate of 0.09 A/μs before the tipping point. A high slew rate reaching 0.09 A/μs was more likely to be the "criterion of current chopping" in the power amplifier than a current magnitude reaching -25 A peak. Moreover, the current chopping was found in another test when the I_{piezo} slewed at 0.1 A/μs, although the $V_{piezo,pp}$ was only 121 V and the P_{piezo} was only 1.59 kW. According to this data point, the P_{piezo} was unlikely the criterion of current chopping in the power amplifier either.

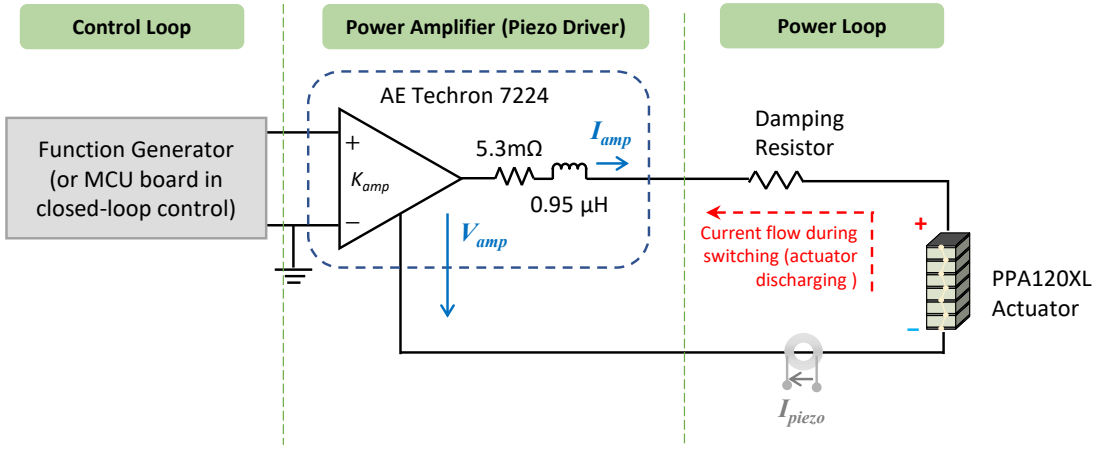

Figure 7.5: Illustration of current flow direction during a PPA120XL actuation process within the power loop of actuator setup.

The power amplifier was most likely the device that limited the driving current I_{piezo} during open-loop tests, because it is the only "active" device that can selectively change the current waveforms in the power loop. As shown in Figure 7.5, the power amplifier is the tie between the low-voltage control loop and the high-voltage power loop within the actuator system, and it isolates the two parts with separated ground references. The output terminal of the power amplifier is connected with the power loop of the actuator system as shown in

Figure 7.5, and the output impedance of power amplifier is 5.3 mΩ in series with 0.95 μH.

The convention for current direction and voltage polarity for the power amplifier is given in Figure 7.5. The positive current flow direction refers to an amplifier current I_{amp} flowing from the amplifier positive output terminal to the actuator and then returning back to the negative output of power amplifier. The current probe measuring I_{piezo} was placed according to this positive current flow direction. However, during actuation processes in the PA-FMS prototype, the I_{piezo} actually flew from the actuator (positive terminal) into the amplifier (positive output terminal), and this was the reason why I_{piezo} kept being negative in all PPA40L test scopes (Figure 3.6) and PPA120XL test scopes (Figure 7.4).

With a sinking current flowing into the power amplifier during actuation processes, it is reasonable to assume some protection mechanisms have been evoked to clamp this current and avoid any damage to the internal circuit of the amplifier. Although the AE Techron 7224 amplifier can supply positive voltage and negative current in the aforementioned PA tests, it is not a perfect four-quadrant amplifier with symmetrical ratings on both voltage and current axis. A *V-I* plane illustrating the four-quadrant operation is shown in Figure 7.6. With the current scale on the horizontal axis and the voltage scale on the vertical axis, the AE Techron 7224 can extend its operation region over all four quadrants, but not evenly covered. For example, the maximum positive current the 7724 amplifier can output is about 40 A, but the maximum negative current outputted from the same amplifier is only about -25 A.

Working in the Quadrant II during PA-FMS switching processes, the power amplifier is a "power sink" as the loop current flows into it for energy dissipation. Its internal mechanism automatically clamps the sinking current to limit the dissipation power. The "power source" that supplies the energy is the PPA120XL actuator, which stores the capacitive electrical energy E_{piezo} in its piezoceramic layers during the 150 V voltage holding period:

$$E_{piezo} = \frac{1}{2} C_{piezo} V_{piezo}^2 = V_{avg} I_{avg} t_{sw} \tag{7.2}$$

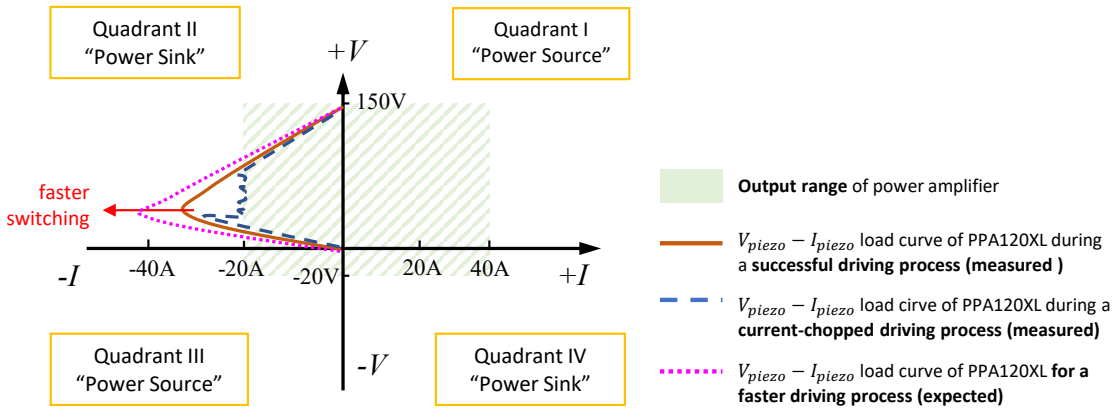

Figure 7.6: Load curves of the PPA120XL actuator under successful and current-chopped driving processes from experiments. The expected load curve under a faster driving process is also drawn for comparison.

The value of E_{piezo} can be estimated once the high-level driving voltage is known (i.e., 150 V for both PPA40L and PPA120XL). If a shorter switching time during the voltage discharging process is desired, a higher product value of $V_{avg}I_{avg}$ is inevitable according to equation 7.2. As the average driving voltage V_{avg} is often a determined value from a voltage-controlled power amplifier that outputs pre-defined voltage waveforms, it comes to the I_{avg} to become larger for getting a smaller switching time t_{sw}. Unfortunately, it was already beyond the sinking current limit (-20 A) of AE Techron 7224 amplifier before the PPA120XL actuator reaching its 250 μs switching time target (as proposed in 2.5). The fastest actuation achieved in PPA120XL open-loop tests is 1 ms as shown in Figure 7.7(a). Figure 7.7(a) also validates the simulated driving current waveform from the electromechanical model of the PPA120XL actuator according to the experimental data. Based on the validated PPA120XL model, a peak sinking current of -51 A is needed for an actuation completed with 270 μs. The peak sinking current should reach -81 A if the PPA120XL actuator needs to be actuated with 200 μs.

A higher sinking current must be drawn from the PPA120XL actuator to accelerate the discharging processes of the actuator's internal capacitance. This higher sinking current can be achieved with a more powerful amplifier with a higher power rating. However, a larger

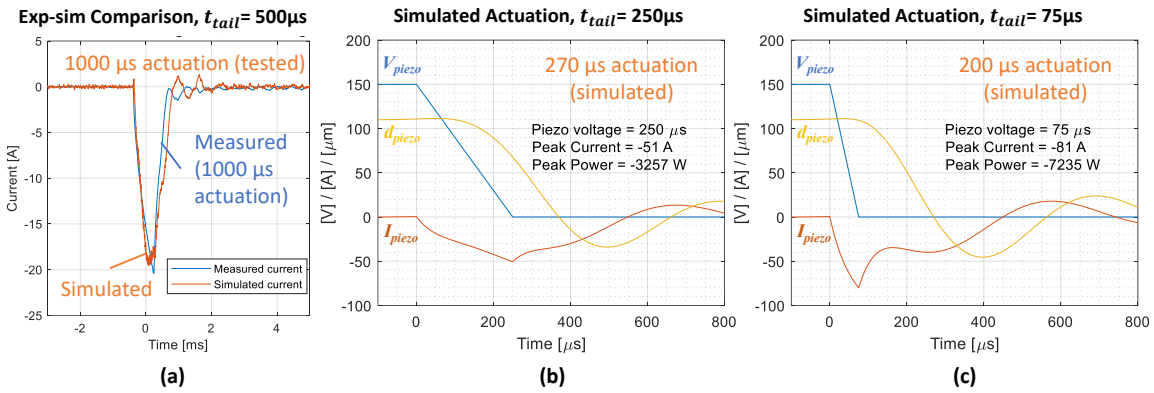

Figure 7.7: Illustration of four-quadrant operation of the power amplifier, and the *V-I* load curve of PPA120XL actuation processes in the Quadrant II under different driving situations.

power amplifier means a higher volume and a larger weight of the overall PA-FMS solution. The SCF-insulated PA-FMS prototype is only 400*160*150 mm^3. Comparatively, the AE Techron 7224 amplifier is almost three times in volume compared to the PA-FMS chamber with a size of 600*500*100 mm^3. It will make less sense to use an even larger power amplifier with more than 1 kW in continuous power rating to save 100 μs in discharging a 51 μF capacitor.

7.3.2 Quadrant-Shifting Branch Design

The implementation of the quadrant-shifting method in the PPA120XL actuator is illustrated in Figure 7.8. This method works for piezoelectric actuations that open contacts in PA-FMS by shrinking the piezoceramic stack. That is, the voltage discharging process should be accelerated for faster PA-FMS switching motion. In order to accelerate the capacitance discharging process through the PA, parallel branches with MOSFET or IGBT switches (SWs) and resistors are added in parallel to the PPA120XL actuator on the power loop side as shown in Figure 7.8.

The working principle of quadrant-shifting branches is explained with reference to Figure 7.9. The PPA120XL is modeled by a single 50 μF capacitor and a single parallel branch with a MOSFET SW_1 and a 1 Ω discharge resistor R_1. As shown in Figure 7.9(a)(b), the

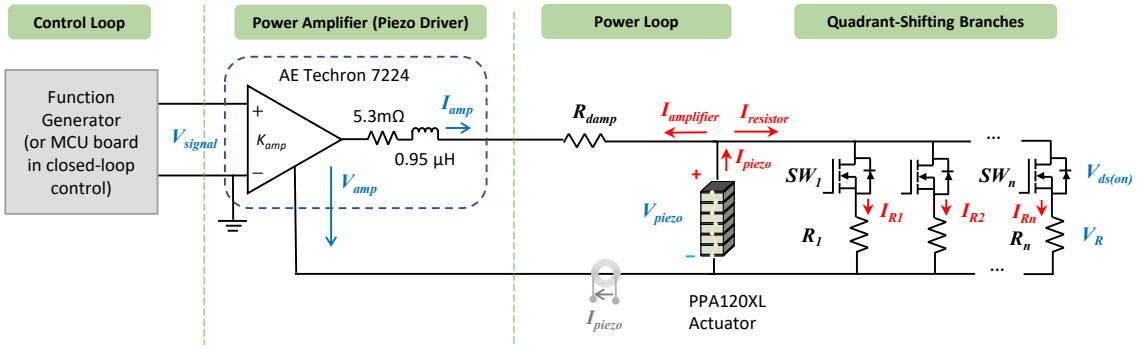

Figure 7.8: Hardware block diagram of PPA120XL driving system with parallel quadrant-shifting branches for the accelerated switching speed.

SW_1 is kept constantly off at $t < t_1$ when no current is flowing and the PA is held at high-level driving voltage 150 V. The switching-off process starts at t_1 when the SW_1 is turned on. After a short delay t_{delay} of 15 μs (t_1 to t_2), the SW_1 starts to discharge the PA. This t_{delay} is determined by coordinating the peak instantaneous current rating of the actuator, dynamic characteristics of the MOSFET switch, and the value of the discharge resistor. As shown in Figure 7.9(a), $I_{piezo}(t_2)$ and $I_R(t_2)$ reach around 150 A instantaneously at the time moment of turning on SW_1. Then, the $I_R(t)$ shows an exponential decay with a time constant of $R_1 C_{piezo}$.

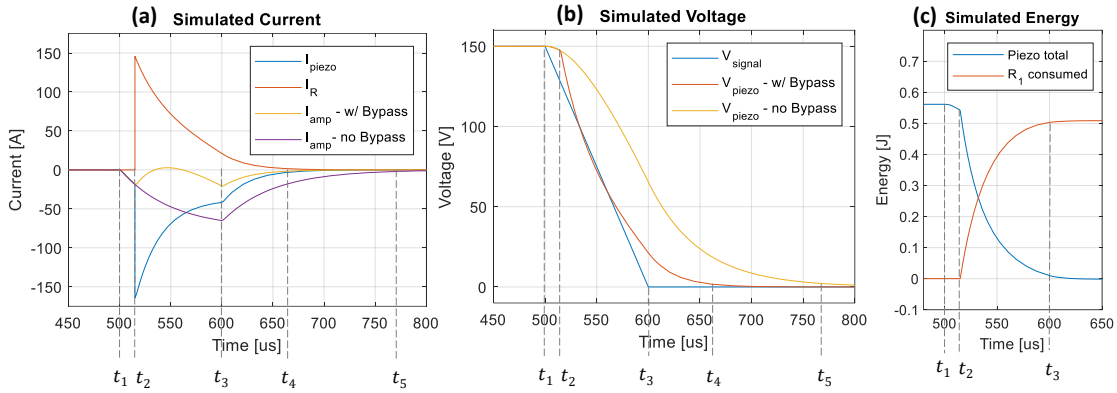

Figure 7.9: Simulated accelerated switching process with a discharge resistor R_1 of 1 Ω, a delay t_{delay} of 15 μs, and the PPA120XL actuator simplified into a 50 μF capacitor.

According to the current relationship, $I_{piezo} = I_{amp} + I_R$, the majority of I_{piezo} flows through the discharge resistor, so the sinking current flowing into the power amplifier I_{amp}

is kept smaller than 20 A. The tail time of amplifier's input signal is set at 100 μs (t_1 to t_3) according to Figure 7.9(b). The Figure 7.9(b) also shows the accelerated voltage discharge from 150 V to 0 V within 160 μs (t_1 to t_4), which has been reduced from the original 280 μs discharging time (t_1 to t_5) without the quadrant-shifting branches.

Given the 150 A instantaneous current flowing through the actuator and the discharge resistor, the total energy being discharged is well below 1 J according to Figure 7.9(c). This limited amount of energy dissipation can make the hardware implementation of quadrant-shifting branches feasible and compact.

7.3.3 Applicability of Quadrant-Shifting Branches

With the help of quadrant-shifting branches, the required sinking capability of the piezo driver is significantly reduced for the PA-FMS design that uses a shrinking actuator to open contacts. In this way, the piezo driver is no longer needed to be a high-bandwidth linear amplifier with 30 kHz bandwidth like AE Techron 7224. High-voltage, high power DC power supplies with much lower bandwidth (i.e., several or tens of Hz for Magna-Power models) may satisfy the driving requirements as illustrated in Figure 7.10. The piezo driver can also be customized for a smaller volume and less weight to boost the power density of the overall PA-FMS setup.

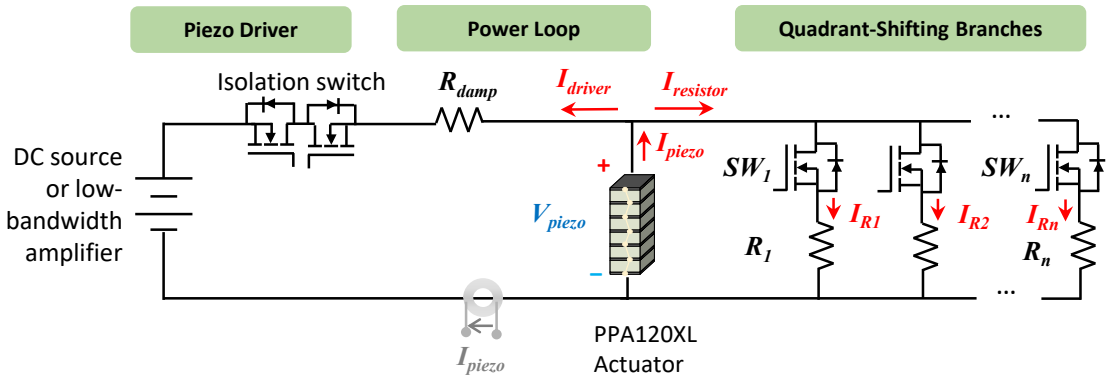

Figure 7.10: Concept drawing about using a DC power supply as the piezo driver after the quadrant-shifting branches are added.

According to Figure 7.10, the DC power supply can slowly charge up the internal capacitance of PA as there is no time requirement for contact reclosing speed in PA-FMS so far. The high-level driving voltage (i.e., 150 V for PPA120XL actuator) can be maintained with zero driving current I_{driver}. Therefore, this small I_{driver} can be easily interrupted by an isolation switch once the switching-off signal is issued. To switch off the PA-FMS by discharging the PA, the isolation switch is first turned off to isolate the DC source (I_{driver} = 0). Then the bypass switches in quadrant-shifting branches are turned on to discharge the PA ($I_{piezo} = I_{resistor}$).

All discussions in this section are for piezoelectric actuations that need to discharge the actuator with a falling voltage (i.e., 150 V to 0 V) to open the PA-FMS contacts. For the other type of piezoelectric actuation that needs a rising voltage (0 V to 150 V) to open the contacts by expanding the actuator, the second improvement on the driving hardware is recommended.

7.4 Sequential-Triggering Method for Ultrafast Piezoelectric Driver

Different from the simultaneous driving method adopted for PPA40L and PPA120XL actuation in previous chapters, this section explores another driving method that sequentially triggers the movements of individual stacks in a multi-stack PA. This time-sequence driving method is designed to match the deformation speed with the propagation velocity of the piezoceramic stress wave, and an extremely ultrafast actuation with less than 30 μs of response time has been achieved in [8].

To estimate the velocity of a simplified one-dimensional stress wave within piezoceramic, according to [8], the piezoceramic body is assumed as purely elastic following Hooke's law in Equation 7.3 with T being the mechanical stress, E being the Young's modulus and $u(t, z)$ being the time-dependent displacement of actuator along the z-axis.

$$T = E\frac{\partial u(t,z)}{\partial z} \tag{7.3}$$

Following the Newton's second law for an infinitesimal volume element, the time-domain relationship between the mechanical stress T and the displacement u with the density ρ as the coefficient is:

$$\frac{\partial T}{\partial z} = \rho \frac{\partial^2 u(t,z)}{\partial t^2} \tag{7.4}$$

Correlating equation 7.3 with 7.4, the propagation velocity of stress wave v can be obtained in:

$$\frac{\partial^2 u(t,z)}{\partial t^2} = v^2 \frac{\partial^2 u(t,z)}{\partial z^2} \tag{7.5}$$

$$v = \sqrt{E/\rho} \tag{7.6}$$

The Young's modulus and density of piezoceramic can be found from material property tables about Tokin® (KEMET® and Cedrat®) actuators in [50], or PI Ceramic® actuators in [107]. Because the piezoceramic material used in PPA120XL and PPA40L actuators is not explicitly specified in the datasheet provided by Tokin®, the stress velocity in Cedrat actuators cannot be reliably calculated. Therefore, a new series of PAs from PI Ceramic GmbH® is referenced in this section with their piezoceramic material properties being given in [107]. For a P888.91 actuator made from PIC252 piezoceramic, which is a modified material from PIC255 piezoceramic in [107], the stress wave propagated through P888.91 actuator has a theoretical velocity of:

$$v = \sqrt{E/\rho} = \sqrt{\frac{15.6 \times 10^{10}[N/m^2]}{7.8 \times 10^3[kg/m^3]}} = 4472\ m/s \tag{7.7}$$

According to [8], the Laplace transform of Equation 7.5 with zero initial conditions and

its generic solution is:

$$\frac{\partial^2 U(s,z)}{\partial z^2} = \frac{s^2}{v^2} U(s,z) \tag{7.8}$$

$$U(s,z) = Ae^{-\frac{s}{v}z} + Be^{\frac{s}{v}z} \tag{7.9}$$

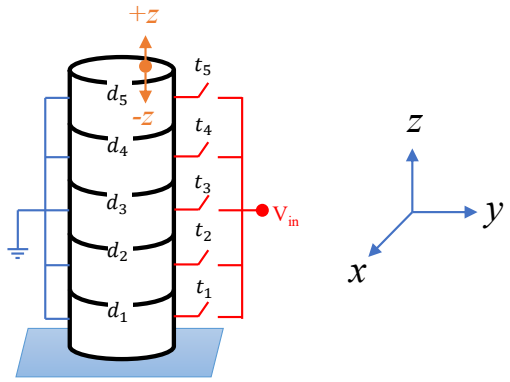

Figure 7.11: Illustration of multi-stack structure in a PA with five cascaded stacks.

The equation 7.9 suggests a two-way propagation of stress wave along both +z and -z direction after the driving voltage is applied. So far, only the +z stress is utilized in PA to move the load vertically with the -z stress neglected. For the discussions on the sequential-triggering method, the -z stress of a higher stack becomes especially helpful on damping the excessive +z stresses being transferred from lower stacks. Referring to Figure 7.11, the -z stress wave of the fifth stack on the top can counteract with +z stress waves transferring from the first stack to the fourth stack standing below. With good timing among these five stacks, the final travel curve d_5 measured from the top of the fifth piezoceramic block can be critically damped without excessive vibration.

The simulation circuit to preliminarily determine the triggering delay for the best vibration damping performance is shown in Figure 7.12. The parameters of piezo stacks come from PI Ceramic® P888.91 actuator. With a stack length of 36 mm in a P888.91 actuator, the estimated travel time of stress wave through one stack is $0.036/4472 = 8\mu s$. The time

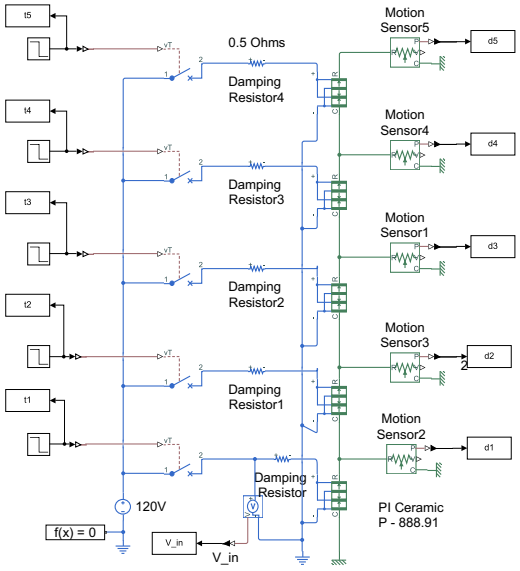

Figure 7.12: Simulated multi-stack PA with five cascaded stacks for demonstrating the sequential-triggering method in Simulink.

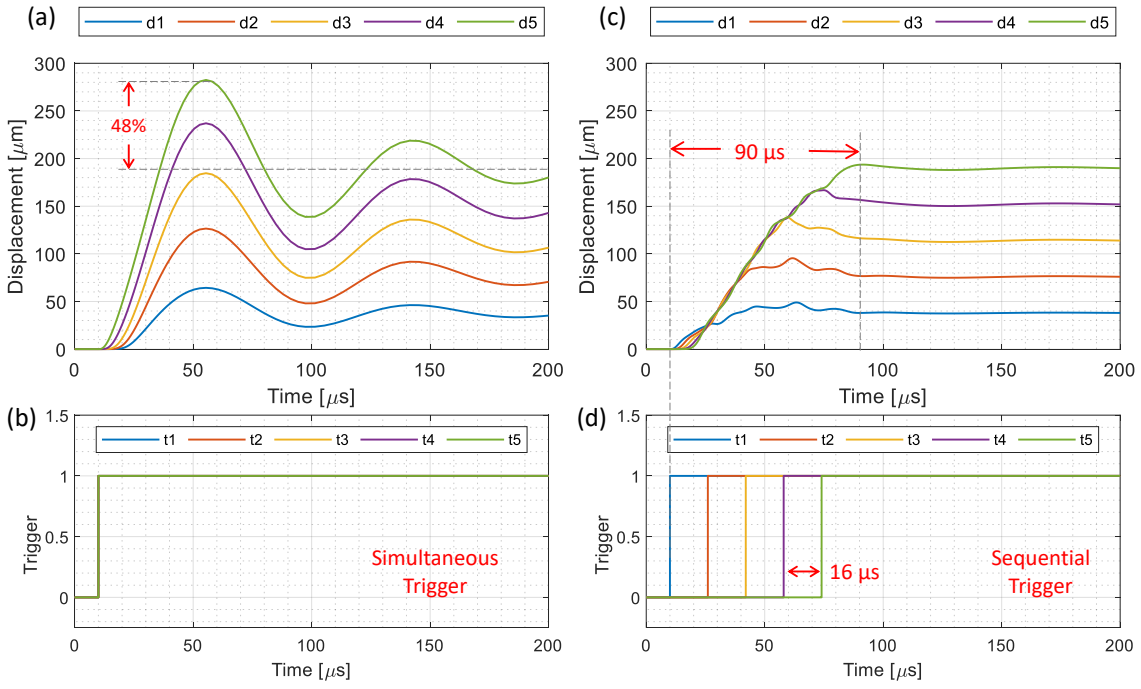

Figure 7.13: Simulated travel curves of individual stacks in a five-stack PA under (a) simultaneous triggering of all five stacks or (c) sequential triggering of individual stacks one after another. (b) is the time sequence of simultaneous triggering, and (d) is the time sequence of sequential triggering.

delay between triggering two adjacent piezoceramic stacks star should be larger than $8\mu s$.

The vibration damping performance of sequential triggering method is illustrated in Figure 7.13(b), as a comparison to the travel curves obtained under simultaneous triggering method in Figure 7.13(a). In a simultaneous triggering event of Figure 7.13(a), all five stacks are applied under a 120 V driving voltage simultaneously. A large overshoot of 48% and an undershoot of 27% has been observed in the simultaneously-triggered d_5 curve, which is the displacement of the fifth piezoceramic stack on the top. After the sequential triggering is applied in Figure 7.13(c) with an optimal time delay of 16 μs, the d_5 displacement becomes critically damped with almost no overshoot or undershoot. Meanwhile, a rise time of 90 μs over a 190 μm full-range displacement is an extraordinary performance, which is almost 500% boost in average movement speed from the goal of 250 μs over 100 μm displacement as targeted in the current PA-FMS EDISON project.

7.5 Chapter Summary

This chapter presents two methods to improve the driving hardware for piezoelectric actuation processes: the quadrant-shifting method and the sequential-triggering method. The first quadrant-shifting method can be implemented with MOSFET-resistor branches connected in parallel to the power amplifier's output terminal. According to the simulation results, the quadrant-shifting branches help the peak discharge current of the PPA120XL actuator reach down to -150 A for accomplishing the actuation within 160 μs. A 40% reduction in the switching time is achieved from the original value of 280 μs without the quadrant-shifting branches. At the same time, the negative current output of the power amplifier is kept less than its sinking current limit. The second sequential-trigger method can be implemented with a DC voltage source and multiple controlled switches connecting to the individual piezoceramic stacks. The time delay between triggering individual switches can shape the travel curve of the piezoceramic stack on the top of the actuator, and a time delay of 16 μs is chosen to attenuate the overshoot in the simulated PA travel curves opti-

mally. The sequential-triggering method can achieve a short switching time of 90 μs for a 200 μm travel in a five-stack actuator.

CHAPTER 8
CONCLUSION AND FUTURE WORK

8.1 Conclusion

This dissertation has focused on understanding the controllability of PAs in FA-FMS to achieve fast and steady travel curves for meeting the requirements of hybrid circuit breakers. The main contribution of this dissertation include: (1) the proposed switching motion controllers are capable of achieving sub-millisecond actuation of a heavy payload over a large displacement and the vibration in PA travel curves is minimized; (2) the proposed comprehensive dynamic model of the PA has captured the dominant high-frequency vibration existed in PA travel curves; (3) the proposed systematic tuning approaches for active damping filters can achieve critical damping in PA system responses along with a high controller bandwidth; (4) the proposed closed-loop simulation and microcontroller hardware implementation approaches have verified the vibration-attenuation performance of switching motion control strategies.

From the perspective of PA control strategy development, a series of switching motion controllers have been proposed and experimentally verified on achieving sub-millisecond actuations of a heavy payload over a large displacement. Moreover, the vibration in PA travel curves is minimized at the same time. The underdamped PA travel curves in a PA-FMS result from a short actuation time (like 140 μs) and a heavy payload (like 500 g) for the PA. After identifying the two-part vibration in open-loop travel curves of a prestressed stack PA, the dominant high-frequency vibration has been captured by a linearized dynamic model. Based on the constructed model, closed-loop controllers with notch filters, lead filters and lag filters are systematically tuned for approaching critical damping in step responses. The tuning principles of switching motion controllers are derived from frequency-

domain analysis and the Nyquist stability criterion. The high bandwidth of 1760 Hz has been achieved in the closed-loop controller with a notch filter. Next, the closed-loop simulation is performed to verify the functionality of embedded controller codes for the selected microcontroller board. Finally, the hardware implementations of four switching motion control strategies in 10 μm actuation tests have been compared on their vibration attenuation performance. The low-frequency vibration has been effectively attenuated by 75% through the PI controller. The high-frequency vibration has been well-confined with a 60% reduced undershoot, a 45% reduced settling time, and a sub-millisecond switching time of 0.6 ms in the notch-filtered travel curve. The measured switching motion performance of the notch-filtered system has also been compared with representative studies in literature to demonstrate its significance. In the outlook of this thesis, three prospective ideas are proposed with their preliminary simulation or experimental results presented.

From the perspective of PA-FMS and HCB development, a significant advantage of PA-FMS over conventional Thomson coil actuated FMS has been identified and experimentally demonstrated. The high controllability of piezoelectric actuators allows advanced control strategies like PI controllers and active damping filters. Therefore, the switching motions of contacts in PA-FMS can be optimized with critically damped travel curves. Compared to most Thomson coil actuated FMS with oscillatory travel curves, the PA-FMS with vibration-free switching motion is more suitable for next-generation HCBs using the sequential tripping technique so that the peak fault current and total energy absorption can be minimized during DC circuit interruptions to protect MVDC systems better.

8.2 Future Work

The research presented in this dissertation can be potentially improved from the following aspects.

Firstly, self-sensing techniques can be adopted to obtain displacement outputs of PAs without a dedicated displacement sensor. A functioning closed-loop PA control relies on

obtaining the feedback signal of actuator displacement quickly and accurately. So far, a separate eddy-current displacement sensor (Lion Precision ECL101 with U5 probe) has been used for displacement feedback. Unfortunately, this sensor probe cannot go into the high-pressure chamber of PA-FMS because the inner-chamber space is very limited, and the U5 eddy-current probe is probably not compatible with the supercritical carbon dioxide environment. As an alternative solution, the self-sensing techniques for obtaining actuator displacements inside the high-pressure chamber can be tried. Here the self-sensing means the actuator and the sensor are collocated in one PA. In this way, the same actuator will execute external commands as an actuator and detect its own changes as a sensor. This advanced self-sensing method can be tried out in future work.

Secondly, the developed design procedures and tuning guidelines of switching motion controllers can be applied to other PAs, such as the PPA120XL actuator to be installed in the SCF-insulated PA-FMS. To de-risk the controller development for the PPA120XL actuator and the overall PA-FMS, controller-hardware-in-the-loop (CHIL) tests will be performed. The controller hardware (the microcontroller board) will be tested with the signals generated from a real-time simulator like an FPGA. The real-time simulator will run the behavior models of the actuator and the PA-FMS with < 1 μs of time steps to simulate the real-world responses.

Thirdly, the experimental verification of the proposed quadrant-shifting method and sequential-triggering method can be performed. For the quadrant-shifting method, the components of MOSFETs and resistors have been selected and partially soldered but not tested yet. For the sequential-triggering method, the multi-stack PA under test can be either modified by unbundling the lead wires of a Cedrat-manufactured actuator or assembling the PA in-lab with customized prestressing springs and individual PA stacks.

Appendices

APPENDIX A

FEEDBACK CONTROL ANALYSIS AND DESIGN

The constructed vibrational dynamics model of PPA40L actuator is represented by a 3rd-order transfer function as in Equation 4.2, which is different from other vibrational dynamics modeled in a 4th-order [67] or a 6th-order [52] transfer function. The higher-order vibrational dynamics models are usually curve-fitted from frequency responses measured with laser displacement sensors and dynamic signal analyzers in [52, 67].

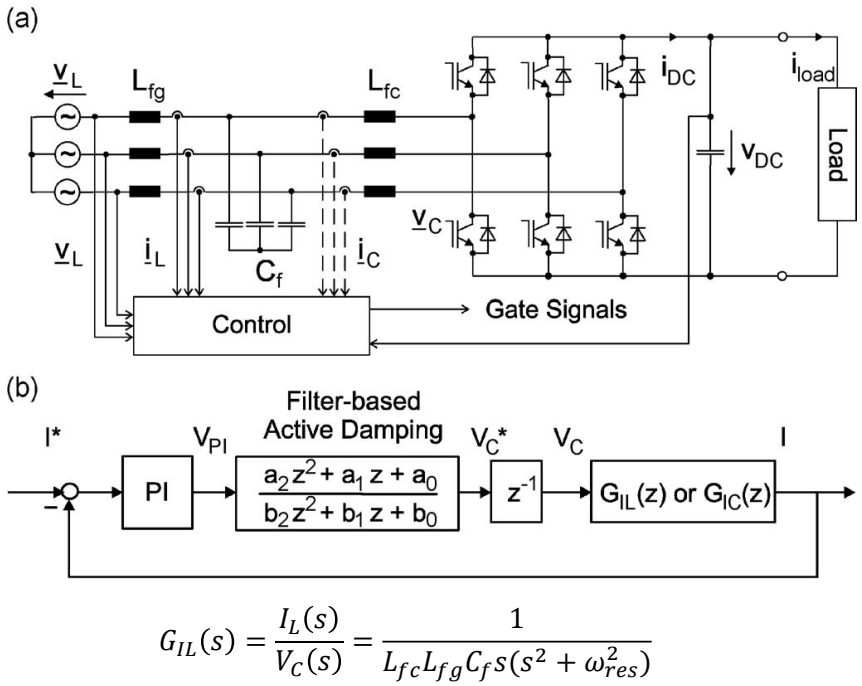

$$G_{IL}(s) = \frac{I_L(s)}{V_C(s)} = \frac{1}{L_{fc}L_{fg}C_f s(s^2 + \omega_{res}^2)}$$

Figure A.1: LCL-filter-based grid-connected voltage source converters. (a) hardware and control scheme, (b) current control loop model [101].

Compared to travel curve controls in PAs, oscillation damping in 3rd-order systems has been studied more thoroughly in another application of power electronics field - the resonance damping in LCL filters for pulse width modulation (PWM) converters. As il-

lustrated in Figure A.1(a) [101], an LCL filter interfaces the grid with a voltage source converter and a load. The transfer function $G_{IL}(s)$ of a lossless LCL filter from the converter output voltage $V_C(s)$ to the AC-side line current $I_L(s)$ constructs a 3rd-order system, and the open-loop Bode plot of $G_{IL}(s)$ in Figure A.1(c) has similar resonant peak with the Bode plot of $G(s)$ in the PPA40L actuator (Figure 4.1(c)). Moreover, the proposed control system for the LCL filter in Figure A.1(b) also has a PI controller and a filter for oscillation/vibration damping with a unity feedback loop, just like the control loop proposed for PPA40L actuator in Figure 4.2.

There are three types of active damping filters used for LCL filters: notch, low-pass and lead-lag [101, 102, 108]. The characteristic frequency responses of these three filters provided in [101] are shown in Figure A.2. The notch filter focuses on canceling the resonant peak in the Bode diagram as introduced above, while the stopping band should be accurate in notch frequency and narrow in bandwidth to reach satisfactory damping performance [14, 52, 53, 64]. On the other end of frequency-selectivity, using a low-pass filter to damp all high-frequency responses including the resonant peak range is an intuitive approach, but it will significantly reduce the bandwidth and response speed of the overall system [101]. For a system with requirements for a fast response like PPA40L actuator, a non-selective low-pass filter is avoided to preserve system bandwidth. An intermediate solution between the single-frequency-damped notch filter and the all-higher-frequency-damped low-pass filter is a lead-lag filter, which adds phase modifications over a limited range of frequency as shown in Figure A.2(b). Therefore, this study will also evaluate the vibration damping performance of both lead filter and lag filter in PPA40L actuator system.

A lead-lag filter boosts the system performance by following the Nyquist stability criterion. The Nyquist stability criterion in open-loop Bode plots counts -180°crossings in the frequency range with gain magnitude above 0 dB, and the system is stable when the positive crossing number equals the negative crossing number [93]. For 3rd-order systems like $G(s)$ in a PA and $G_{IL}(s)$ in an LCL filter, there is no positive crossing and only one

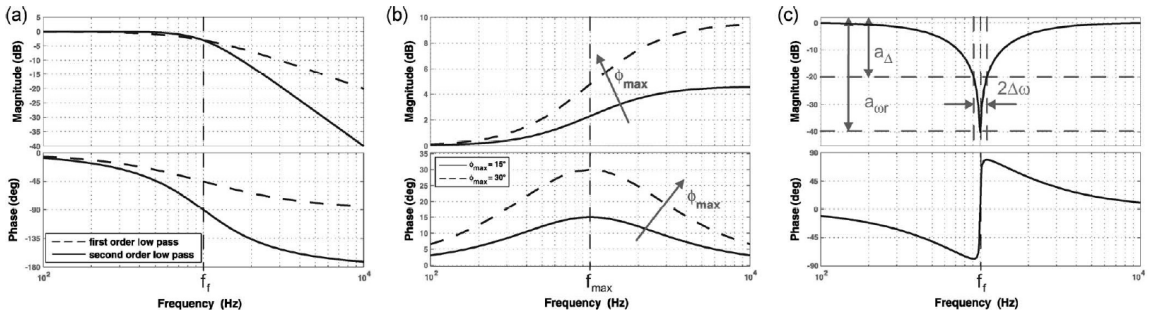

Figure A.2: Characteristic frequency response of (a) low-pass filter, (b) lead filter, and (c) notch filter [101].

negative crossing in their phase curves, so the negative crossing must reside outside the positive-gain region to avoid destabilizing the system. Figure A.1(c) shows a worst case about $G_{IL}(s)$ in LCL filter that the negative crossing resides within the positive-gain region, so an active damping filter must be used to stabilize the system. Figure 4.1(a) shows a self-stabilized system about $G(s)$ in PPA40L actuator, because the negative crossing resides slightly outside of the positive-gain region. But the distance between 0dB-crossover frequency and -180°crossover frequency is so tiny that any minor change in system parameters may destabilize the system. Therefore, a damping filter is also needed in PA systems for more robust closed-loop performance.

In Chapter 3, the vibration nonlinearity in PPA40L actuator has been derived in the s-domain. If the PI controller and damping filters are also designed in the s-domain, they could only be implemented in hardware setup through analog controllers. For example, an analog notch filter constructed with op-amp circuits was used for vibration damping in [14]. However, the analog implementation of PI controller and filters is not a good choice in our controller development considering the hardware debugging effort and potential parameter mismatches.

Instead, a digital format of PI controller with filters is chosen to be implemented in the hardware implementation tests, which is directly tuned upon a discretized actuator control plant $G_d(z)$. A tricky thing about discretizing $G(s)$ to $G_d(z)$ is that a wrong discretization method may destabilize the system, just like what happens in Figure A.3(c) where a zero-

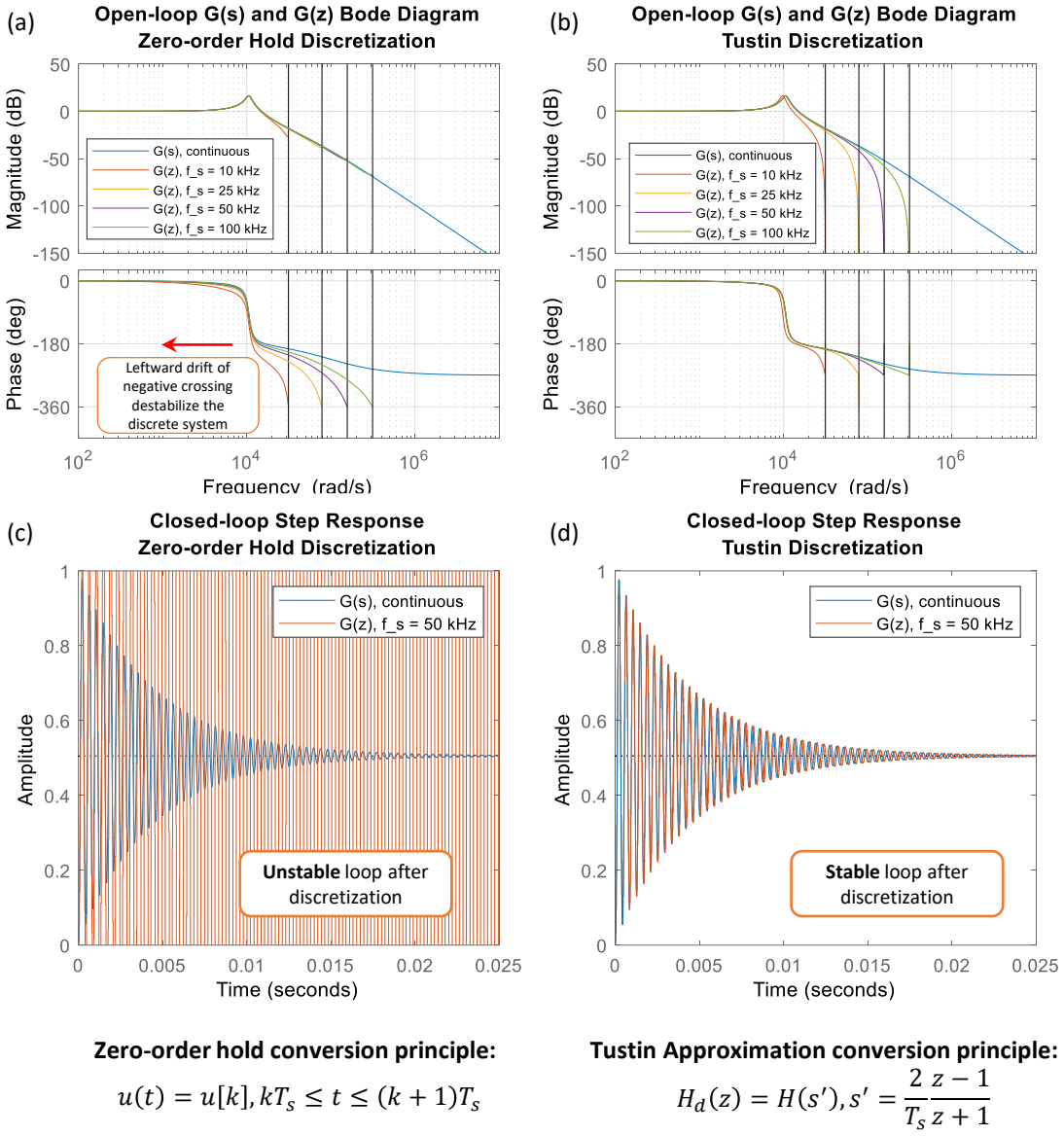

Figure A.3: Discretization stability issues in PPA40L model (415 g load mass) discretized by zero-order hold method with its (a) Bode diagram and (c) step response, and by Tustin approximation method [109] with its (a) Bode diagram and (c) step response.

Table A.1: General expressions of continuous and discrete transfer functions in the closed-loop control system for the PPA40L actuator.

Block	Continuous	Discrete
PI Controller	$C_{PI}(s) = K_{ps} + \frac{K_{is}}{s}$	$C_{PI}(z) = K_{pz} + K_{iz}\frac{T_s}{z-1}$
Filter Notch	$C_{notch}(s) = \frac{s^2+2D_z w_f s+w_F^2}{s^2+2D_p w_f s+w_F^2}$	$C_{notch}(z) = \frac{a_0 z^2+a_1 z+a_2}{b_0 z^2+b_1 z+b_2}$
Filter Lead-lag	$C_{leadlag}(s) = \frac{1+T_z s}{1+T_p s}$	$C_{leadlag}(z) = \frac{z-T_1}{z-T_2}$
PPA40L Actuator	$\frac{V_{max}}{x_{max}}G(s)$	$c2d(\frac{V_{max}}{x_{max}}G(s), f_s, 'Tustin')$

order hold discretization method is used. As explained in the Bode plot of Figure A.3(a), the zero-order hold discretization moves the phase curves leftwards, so the -180° negative crossing point falls into the positive-gain region and triggers divergence. As a contrast, the closed-loop step response of $G_d(z)$ discretized with Tustin approximation method keeps the same stability with the original continuous system $G(s)$ (Figure A.3(b)), because the discrete system Bode plots overlap with continuous system curves within the critical crossover regions in Figure A.3(d).

Following the block diagram given in Figure 4.2, the generic expressions of PI controller, notch filter and lead/lag filter are given in Table A.1. The normalized expressions of actuator plant $G(s)$ and $G_d(z)$ are also computed after multiplied by a fix gain of V_{max}/x_{max}.

Both continuous model $G(s)$ and discretized model $G_d(z)$ of PPA40L actuator encounter a large steady-state error of 0.5 after being closed by a unity feedback loop, as illustrated in Figure A.3(c)(d). An integrator is thus added to eliminate this steady-state error following classical PID control theory. Unfortunately, adding an integrator $1/(z-1)$ in series with $G_d(z)$ will destabilize the discretized system as shown in Figure A.4(b), although the original continuous system preserves its stability after an integrator is added in Figure A.4(a). The stability criterion for a continuous system is that all its closed-loop poles are in the left half of s-plane, just like the pole-zero map of a closed-loop $G(s)$ with a con-

tinuous integrator $1/s$ shown in Figure A.4(a). Correspondingly, the stability criterion of a discrete system is that all its closed-loop poles are surrounded by a unit circle in z-plane. But there is one pair of complex poles residing outside of the unit circle as shown in Figure A.4(b), meaning the closed-loop $G_d(z)$ with a discrete integrator $1/(z-1)$ constitutes an unstable system.

Therefore, a proportional gain must be added in series with the integral controller to avoid instability of the system, which constitutes a classic PI controller as defined in Table A.1.

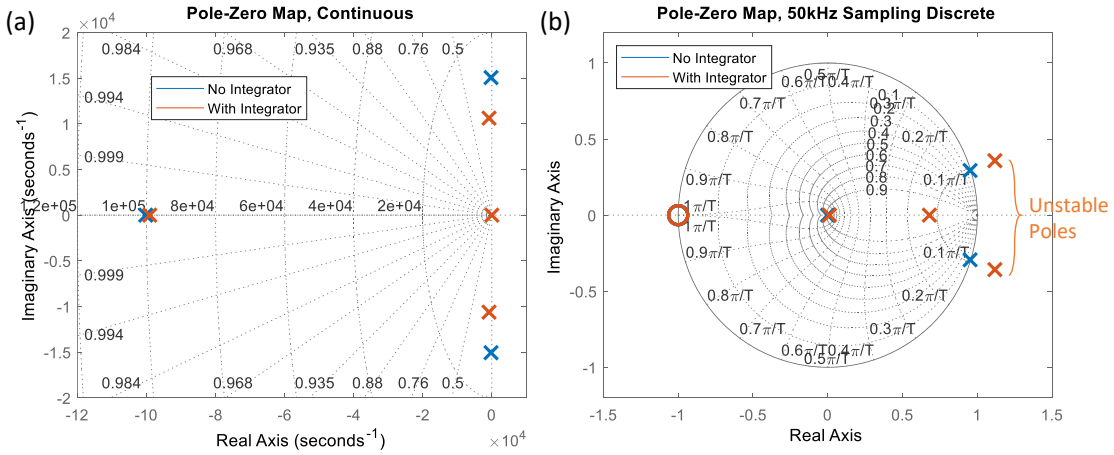

Figure A.4: Pole-zero plots of closed-loop systems (both continuous and discrete - Tustin method) after adding an integrator in series with the actuator , 415 g load mass in PPA40L actuator.

REFERENCES

[1] C. M. Franck, "Hvdc circuit breakers: A review identifying future research needs," *IEEE Transactions on Power Delivery*, vol. 26, no. 2, pp. 998–1007, 2011.

[2] C. Xu, T. Damle, and L. Graber, "A survey on mechanical switches for hybrid circuit breakers," in *IEEE Power & Energy Society General Meeting*, 2019.

[3] C. Xu, T. Damle, M. D. Bosworth, D. Soto, R. Agarwal, M. Steurer, and L. Graber, "Piezoelectrically actuated fast mechanical switch for mvdc protection," *IEEE Transactions on Power Delivery*, pp. 1–1, 2020.

[4] P. Technology, *Forces and stiffness*, https://www.piceramic.com/en/piezo-technology /properties-piezo-actuators/forces-stiffnesses/, Web Page, access: Dec 2020.

[5] M. R. K. Rachi and I. Husain, "Main breaker switching control and design optimization for a progressively switched hybrid dc circuit breaker," in *IEEE Energy Conversion Congress and Expo*, pp. 6016–6023, ISBN: 2329-3748.

[6] M. H. Hedayati and D. Jovcic, "Reducing peak current and energy dissipation in hybrid hvdc cbs using disconnector voltage control," *IEEE Transactions on Power Delivery*, vol. 33, no. 4, pp. 2030–2038, 2018.

[7] C. Peng, L. Mackey, I. Husain, A. Q. Huang, W. Yu, B. Lequesne, and R. Briggs, "Active damping of ultrafast mechanical switches for hybrid ac and dc circuit breakers," *IEEE Transactions on Industry Applications*, vol. 53, no. 6, pp. 5354–5364, 2017.

[8] X. Ba, Q. Pan, B. Ju, and Z. Feng, "Ultrafast displacement actuation of piezoelectric stacks with time-sequence," *IEEE Transactions on Industrial Electronics*, vol. 64, no. 4, pp. 2955–2961, 2017.

[9] H. Tang, J. Gao, X. Chen, K. Yu, S. To, Y. He, X. Chen, Z. Zeng, S. He, C. Chen, and Y. Li, "Development and repetitive-compensated pid control of a nanopositioning stage with large-stroke and decoupling property," *IEEE Transactions on Industrial Electronics*, vol. 65, no. 5, pp. 3995–4005, 2018.

[10] Z. Zhu, L. Chen, P. Huang, L. Schönemann, O. Riemer, J. Yao, S. To, and W. Zhu, "Design and control of a piezoelectrically actuated fast tool servo for diamond turning of microstructured surfaces," *IEEE Transactions on Industrial Electronics*, vol. 67, no. 8, pp. 6688–6697, 2020.

[11] A. J. Fleming, "Nanopositioning system with force feedback for high-performance tracking and vibration control," *IEEE/ASME Transactions on Mechatronics*, vol. 15, no. 3, pp. 433–447, 2010.

[12] X. Liao, X. Pang, L. He, and Z. Feng, "Dynamic mass isolation for improving the moving efficiency of an impact drive mechanism," *IEEE Transactions on Industrial Electronics*, vol. 67, no. 10, pp. 8526–8534, 2020.

[13] G. Gu, L. Zhu, C. Su, H. Ding, and S. Fatikow, "Modeling and control of piezo-actuated nanopositioning stages: A survey," *IEEE Transactions on Automation Science and Engineering*, vol. 13, no. 1, pp. 313–332, 2016.

[14] K. K. Leang and S. Devasia, "Feedback-linearized inverse feedforward for creep, hysteresis, and vibration compensation in afm piezoactuators," *IEEE Transactions on Control Systems Technology*, vol. 15, no. 5, pp. 927–935, 2007.

[15] A. Safa, R. Y. Abdolmalaki, and H. C. Nejad, "Precise position tracking control with an improved transient performance for a linear piezoelectric ceramic motor," *IEEE Transactions on Industrial Electronics*, vol. 66, no. 4, pp. 3008–3018, 2019.

[16] G. Gu, L. Zhu, C. Su, and H. Ding, "Motion control of piezoelectric positioning stages: Modeling, controller design, and experimental evaluation," *IEEE/ASME Transactions on Mechatronics*, vol. 18, no. 5, pp. 1459–1471, 2013.

[17] ARPA-E, *Building reliable electronics to achieve kilovolt effective ratings safely (breakers)*, U.S. Department of Energy, 2018.

[18] A. Giannakis and D. Peftitsis, "Mvdc distribution grids and potential applications: Future trends and protection challenges," in *European Conference on Power Electronics and Applications*, pp. 1–9, ISBN: null.

[19] M. Steurer, K. Frohlich, W. Holaus, and K. Kaltenegger, "A novel hybrid current-limiting circuit breaker for medium voltage: Principle and test results," *IEEE Transactions on Power Delivery*, vol. 18, no. 2, pp. 460–467, 2003.

[20] J. He, Y. Luo, M. Li, Y. Zhang, Y. Xu, Q. Zhang, and G. Luo, "A high-performance and economical multiport hybrid direct current circuit breaker," *IEEE Transactions on Industrial Electronics*, vol. 67, no. 10, pp. 8921–8930, 2020.

[21] R. Rodrigues, Y. Du, A. Antoniazzi, and P. Cairoli, "A review of solid-state circuit breakers," *IEEE Transactions on Power Electronics*, vol. 36, no. 1, pp. 364–377, 2021.

[22] L. Qi, P. Cairoli, Z. Pan, C. Tschida, Z. Wang, V. R. Ramanan, L. Raciti, and A. Antoniazzi, "Solid-state circuit breaker protection for dc shipboard power systems:

Breaker design, protection scheme, validation testing," *IEEE Transactions on Industrial Applications*, vol. 56, no. 2, pp. 952–960, 2020.

[23] C. Xu, J. Wei, L. Zheng, X. Han, M. Saeedifard, R. P. Kandula, K. Kandasamy, D. Divan, and L. Graber, "Lightning impulse protection for grid-connected solid-state transformers," in *IEEE Energy Conversion Congress and Exposition*, pp. 6057–6064, ISBN: 2329-3748.

[24] W. Wen, Y. Huang, Y. Sun, J. Wu, M. Al-Dweikat, and W. Liu, "Research on current commutation measures for hybrid dc circuit breakers," *IEEE Transactions on Power Delivery*, vol. 31, no. 4, pp. 1456–1463, 2016.

[25] V. Lenz, "Dc current breaking solutions in hvdc applications," M.S. 2015.

[26] R. Smeets, L. V. Der Sluis, M. Kapetanović, D. F. Peelo, and A. Janssen, *Switching in Electrical Transmission and Distribution Systems*. John Wiley & Sons Ltd, 2014, ISBN: 9781118381359.

[27] B. Roodenburg and B. H. Evenblij, "Design of a fast linear drive for (hybrid) circuit breakers – development and validation of a multi domain simulation environment," *Mechatronics*, vol. 18, no. 3, pp. 159–171, 2008.

[28] C. Peng, I. Husain, A. Q. Huang, B. Lequesne, and R. Briggs, "A fast mechanical switch for medium-voltage hybrid dc and ac circuit breakers," *IEEE Transactions on Industry Applications*, vol. 52, no. 4, pp. 2911–2918, 2016.

[29] Y. Song, J. Sun, M. Saeedifard, S. Ji, L. Zhu, S. Meliopoulos, and L. Graber, "Reducing the fault transient magnitudes in multi-terminal hvdc grids by sequential tripping of hybrid circuit breaker modules," *IEEE Transactions on Industrial Electronics*, pp. 1–1, 2018.

[30] B. Hátsági, "Electromagnetic modellin and testing of a thomson coil based actuator," M.S. 2017.

[31] W. Wen, Y. Huang, M. Al-Dweikat, Z. Zhang, T. Cheng, S. Gao, and W. Liu, "Research on operating mechanism for ultra-fast 40.5-kv vacuum switches," *IEEE Transactions on Power Delivery*, vol. 30, no. 6, pp. 2553–2560, 2015.

[32] C. Peng, X. Song, A. Q. Huang, and I. Husain, "A medium-voltage hybrid dc circuit breaker—part ii: Ultrafast mechanical switch," *IEEE Journal of Emerging and Selected Topics in Power Electronics*, vol. 5, no. 1, pp. 289–296, 2017.

[33] A. Bissal, J. Magnusson, and G. Engdahl, "Electric to mechanical energy conversion of linear ultrafast electromechanical actuators based on stroke requirements," *IEEE Transactions on Industry Applications*, vol. 51, no. 4, pp. 3059–3067, 2015.

[34] L. Graber, S. Smith, D. Soto, I. Nowak, J. Owens, and M. Steurer, "A new class of high speed disconnect switch based on piezoelectric actuators," in *IEEE Electric Ship Technologies Symposium*, pp. 312–317.

[35] CEDRAT, "Amplified piezo actuator apa1000xl," Catalog, 2020.

[36] C. Xu and L. Graber, "Thermosyphon bushing: Design, simulation and implementation," *Applied Thermal Engineering*, vol. 161, p. 114 180, 2019.

[37] Noliac, *Technical support - actuators- driving and control*, http://www.noliac.com/tutorials/technical-support-actuators/driving-control/, Web Page, access: Dec 2020.

[38] "Parallel pre-stressed actuators ppa120xl," CEDRAT Technologies, Report, Oct 2015.

[39] J. Wei, A. Cruz, C. Xu, F. Haque, C. Park, and L. Graber, "A review on dielectric properties of supercritical fluids," in *IEEE Electrical Insulation Conference*, pp. 107–113, ISBN: 2576-6791.

[40] J. Wei, A. Cruz, F. Haque, C. Park, and L. Graber, "Investigation of the dielectric strength of supercritical carbon dioxide–trifluoroiodomethane fluid mixtures," *Physics of Fluids*, vol. 32, no. 10, p. 103 309, 2020.

[41] S. Ito, M. Poik, J. Schlarp, and G. Schitter, "Atomic force microscopy breaking through the vertical range-bandwidth tradeoff," *IEEE Transactions on Industrial Electronics*, vol. 68, no. 1, pp. 786–795, 2021.

[42] M. Chen, Y. Yamada, S. Zen, N. Takeuchi, and K. Yasuoka, "On-state contact resistance and arc-less commutation characteristics of cu-w clad contact materials in a hybrid dc switch," *IEEE Transactions on Components, Packaging and Manufacturing Technology*, vol. 10, no. 7, pp. 1138–1147, 2020.

[43] M. Chen, K. Nakayama, S. Zen, and K. Yasuoka, "Threshold current of arc-less current commutation in a hybrid dc switch," *IEEE Transactions on Components, Packaging and Manufacturing Technology*, vol. 9, no. 6, pp. 1029–1037, 2019.

[44] K. Yasuoka, Y. Tsuboi, T. Hayakawa, and N. Takeuchi, "Arcless commutation of a hybrid dc breaker by contact voltage of molten metal bridge," *IEEE Transactions on Components, Packaging and Manufacturing Technology*, vol. 8, no. 3, pp. 350–355, 2018.

[45] C. Ou, H. Yinming, and K. Yasuoka, "New configuration of contacts for increasing the threshold current of arc-free commutation in a dc hybrid switch," *IEEE Transactions on Components, Packaging and Manufacturing Technology*, vol. 10, no. 8, pp. 1320–1327, 2020.

[46] S. J. Rupitsch, *Piezoelectric Sensors and Actuators*. Springer, 2018.

[47] IEEE, *Ieee standard on piezoelectricity*, Standard, 1988.

[48] Z. Du, T. Zhang, L. Deng, C. Zhou, Z. Cao, and S. Wang, "A charge-amplifier based self-sensing method for measurement of piezoelectric displacement," in *IEEE International Conference on Mechatronics and Automation*, pp. 1995–1999, ISBN: 2152-744X.

[49] A. P. Boresi, R. J. Schmidt, and O. M. Sidebottom, *Advanced mechanics of materials*. Wiley New York, 1985, vol. 6.

[50] Tokin, "Piezoelectric ceramics," Report, 2017.

[51] PI-Ceramic, *Electrical operation of piezo actuators*, https://www.piceramic.com/en/piezo-technology/properties-piezo-actuators/electrical-operation/, Web Page, access: Dec 2020.

[52] K. K. Leang, Q. Zou, and S. Devasia, "Feedforward control of piezoactuators in atomic force microscope systems," *IEEE Control Systems Magazine*, vol. 29, no. 1, pp. 70–82, 2009.

[53] Y. K. Yong, S. O. R. Moheimani, B. J. Kenton, and K. K. Leang, "Invited review article: High-speed flexure-guided nanopositioning: Mechanical design and control issues," *Review of Scientific Instruments*, vol. 83, no. 12, p. 121 101, 2012.

[54] L. Gao, H. Guo, S. Zhang, and C. A. Randall, "Base metal co-fired multilayer piezoelectrics," *Actuators*, vol. 5, no. 1, p. 8, 2016.

[55] CEDRAT, *Preloaded actuators by ctec*, https://www.cedrat-technologies.com/en/products/piezo-actuators.html, Web Page, access: Dec 2020.

[56] "Parallel pre-stressed actuators ppa40l," CEDRAT Technologies, Report, Feb 2019.

[57] M. Kuna, "Fracture mechanics of piezoelectric materials – where are we right now?" *Engineering Fracture Mechanics*, vol. 77, no. 2, pp. 309–326, 2010.

[58] P. Pertsch, B. Broich, R. Block, S. Richter, and E. Hennig, *Development of highly reliable piezo multilayer actuators and lifetime tests under dc and ac operating conditions*, Press Release, 2010.

[59] C. Xu, J. Wei, and L. Graber, "Compatibility analysis of piezoelectric actuators in supercritical carbon dioxide," in *IEEE Electrical Insulation Conference*, pp. 171–174, ISBN: 2576-6791.

[60] G. Schitter, K. J. Astrom, B. E. DeMartini, P. J. Thurner, K. L. Turner, and P. K. Hansma, "Design and modeling of a high-speed afm-scanner," *IEEE Transactions on Control Systems Technology*, vol. 15, no. 5, pp. 906–915, 2007.

[61] M. Goldfarb and N. Celanovic, "Modeling piezoelectric stack actuators for control of micromanipulation," *IEEE Control Systems Magazine*, vol. 17, no. 3, pp. 69–79, 1997.

[62] R. Dsouza, B. Benny, A. Sequeira, and N. Karanth, "Hysteresis modeling of amplified piezoelectric stack actuator for the control of the microgripper," *American Scientific Research Journal for Engineering, Technology, and Sciences*, vol. 15, pp. 265–281, 2016.

[63] N. Fallahinia, M. Zareinejad, H. Talebi, and H. Ghafarirad, "Robust force control of piezoelectric precision positioning actuators using self-sensing method," in *IEEE /ASME International Conference on Advanced Intelligent Mechatronics*, pp. 533–538, ISBN: 2159-6255.

[64] G. M. Clayton, S. Tien, K. K. Leang, Q. Zou, and S. Devasia, "A review of feedforward control approaches in nanopositioning for high-speed spm," *Journal of Dynamic Systems, Measurement, and Control*, vol. 131, no. 6, p. 61 101, 2009.

[65] A. Woronko, J. Huang, and Y. Altintas, "Piezoelectric tool actuator for precision machining on conventional cnc turning centers," *Precision Engineering*, vol. 27, no. 4, pp. 335–345, 2003.

[66] G. Stöppler and S. Douglas, "Adaptronic gantry machine tool with piezoelectric actuator for active error compensation of structural oscillations at the tool centre point," *Mechatronics*, vol. 18, no. 8, pp. 426–433, 2008.

[67] D. Croft and S. Devasia, "Vibration compensation for high speed scanning tunneling microscopy," *Review of Scientific Instruments*, vol. 70, no. 12, pp. 4600–4605, 1999.

[68] K. Furutani, M. Urushibata, and N. Mohri, "Displacement control of piezoelectric element by feedback of induced charge," *Nanotechnology*, vol. 9, no. 2, pp. 93–98, 1998.

[69] J. W. Li, X. B. Chen, and W. J. Zhang, "A new approach to modeling system dynamics—in the case of a piezoelectric actuator with a host system," *IEEE/ASME Transactions on Mechatronics*, vol. 15, no. 3, pp. 371–380, 2010.

[70] Y. Singh, "Experimental investigation and numerical modelling of hydrogen exposed piezoelectric actuators for fuel injector applications," M.S. 2013.

[71] C. Zhou, J. Duan, G. Deng, and J. Li, "A novel high-speed jet dispenser driven by double piezoelectric stacks," *IEEE Transactions on Industrial Electronics*, vol. 64, no. 1, pp. 412–419, 2017.

[72] D. Zhou, M. Kamlah, and D. Munz, "Effects of uniaxial prestress on the ferroelectric hysteretic response of soft pzt," *Journal of the European Ceramic Society*, vol. 25, no. 4, pp. 425–432, 2005.

[73] H. J. M. T. S. Adriaens, W. L. D. Koning, and R. Banning, "Modeling piezoelectric actuators," *IEEE/ASME Transactions on Mechatronics*, vol. 5, no. 4, pp. 331–341, 2000.

[74] C. Visone, "Hysteresis modelling and compensation for smart sensors and actuators," *Journal of Physics: Conference Series*, vol. 138, p. 012 028, 2008.

[75] H. Janocha and K. Kuhnen, "Real-time compensation of hysteresis and creep in piezoelectric actuators," *Sensors and Actuators A: Physical*, vol. 79, no. 2, pp. 83–89, 2000.

[76] Y. Gao, D. Zhang, and C. W. Yu, "Dynamic modeling of a novel workpiece table for active surface grinding control," *International Journal of Machine Tools and Manufacture*, vol. 41, no. 4, pp. 609–624, 2001.

[77] M. Quant, H. Elizalde, A. Flores, R. Ramírez, P. Orta, and G. Song, "A comprehensive model for piezoceramic actuators: Modelling, validation and application," *Smart Materials and Structures*, vol. 18, no. 12, p. 125 011, 2009.

[78] L.-S. Chen, J.-Y. Yen, J. J. H. Chen, F.-C. Kuo, M.-S. Chen, Y.-Y. Chen, and B.-I. Chung, "Precision tracking of a piezo-driven stage by charge feedback control," *Precision Engineering*, vol. 37, no. 4, pp. 793–804, 2013.

[79] J. Minase, T. F. Lu, B. Cazzolato, and S. Grainger, "A review, supported by experimental results, of voltage, charge and capacitor insertion method for driving piezoelectric actuators," *Precision Engineering*, vol. 34, no. 4, pp. 692–700, 2010.

[80] M. Bazghaleh, S. Grainger, and M. Mohammadzaheri, "A review of charge methods for driving piezoelectric actuators," *Journal of Intelligent Material Systems and Structures*, vol. 29, no. 10, pp. 2096–2104, 2017.

[81] M. Goldfarb and N. Celanovic, "A lumped parameter electromechanical model for describing the nonlinear behavior of piezoelectric actuators," *Journal of Dynamic Systems, Measurement, and Control*, vol. 119, no. 3, pp. 478–485, 1997.

[82] A. J. Fleming and S. O. R. Moheimani, "Improved current and charge amplifiers for driving piezoelectric loads, and issues in signal processing design for synthesis

of shunt damping circuits," *Journal of Intelligent Material Systems and Structures*, vol. 15, no. 2, pp. 77–92, 2004.

[83] S. Z. Mansour and R. Seethaler, "Displacement and force self-sensing technique for piezoelectric actuators using a nonlinear constitutive model," *IEEE Transactions on Industrial Electronics*, pp. 1–1, 2019.

[84] H. Kaizuka and B. Siu, "A simple way to reduce hysteresis and creep when using piezoelectric actuators," *Japanese Journal of Applied Physics*, vol. 27, no. Part 2, No. 5, pp. L773–L776, 1988.

[85] AE-Techron, *7224 - single-phase, 2u, industrial amplifier*, https://aetechron.com /IND-RESEARCH-7224.shtml, Web Page, access: Dec 2020.

[86] Lion-Precision, "Comparing capacitive and eddy-current sensors - technote lt05-0011," Report, 2009.

[87] K. Saigusa and T. Morita, "Self-sensing control of piezoelectric positioning stage by detecting permittivity," *Sensors and Actuators A: Physical*, vol. 226, pp. 76–80, 2015.

[88] L. Juhász, J. Maas, and B. Borovac, "Parameter identification and hysteresis compensation of embedded piezoelectric stack actuators," *Mechatronics*, vol. 21, no. 1, pp. 329–338, 2011.

[89] J Figura, "Modeling and control of piezoelectric microactuators," B.S. 2013.

[90] A. Kawamata, Y. Kadota, H. Hosaka, and T. Morita, "Self-sensing piezoelectric actuator using permittivity detection," *Ferroelectrics*, vol. 368, no. 1, pp. 194–201, 2008.

[91] C. Yang, N. Verbeek, F. Xia, Y. Wang, and K. Youcef-Toumi, "Modeling and control of piezoelectric hysteresis: A polynomial-based fractional order disturbance compensation approach," *IEEE Transactions on Industrial Electronics*, vol. 68, no. 4, pp. 3348–3358, 2021.

[92] S. Kapucu, G. Alici, and S. Bayseç, "Residual swing/vibration reduction using a hybrid input shaping method," *Mechanism and Machine Theory*, vol. 36, no. 3, pp. 311–326, 2001.

[93] G. F. Franklin, J. D. Powell, A. Emami-Naeini, and J. D. Powell, *Feedback control of dynamic systems*. Pearson Higher Education, 2002, vol. 4.

[94] Y. Chen, J. Qiu, J. Palacios, and E. C. Smith, "Tracking control of piezoelectric stack actuator using modified prandtl–ishlinskii model," *Journal of Intelligent Material Systems and Structures*, vol. 24, no. 6, pp. 753–760, 2012.

[95] G.-Y. Gu, M.-J. Yang, and L.-M. Zhu, "Real-time inverse hysteresis compensation of piezoelectric actuators with a modified prandtl-ishlinskii model," *Review of Scientific Instruments*, vol. 83, no. 6, p. 065 106, 2012.

[96] M. Islam, R. Seethaler, and D. Mumford, "Hysteresis independent on-line capacitance measurement for piezoelectric stack actuators," in *Canadian Conference on Electrical and Computer Engineering*, pp. 1149–1153, ISBN: 0840-7789.

[97] H. Ikeda and T. Morita, "High-precision positioning using a self-sensing piezoelectric actuator control with a differential detection method," *Sensors and Actuators A: Physical*, vol. 170, no. 1, pp. 147–155, 2011.

[98] M. N. Islam, "Position self-sensing in the presence of creep, hysteresis, and self-heating for piezoelectric actuators," Ph.D. 2013.

[99] J. B. Liseli, J. Agnus, P. Lutz, and M. Rakotondrabe, "Self-sensing method considering the dynamic impedance of piezoelectric based actuators for ultralow frequency," *IEEE Robotics and Automation Letters*, vol. 3, no. 2, pp. 1049–1055, 2018.

[100] S. Z. Mansour and R. J. Seethaler, "Simultaneous displacement and force estimation of piezoelectric stack actuators using charge and voltage measurements," *IEEE/ASME Transactions on Mechatronics*, vol. 22, no. 6, pp. 2619–2624, 2017.

[101] J. Dannehl, M. Liserre, and F. W. Fuchs, "Filter-based active damping of voltage source converters with lcl filter," *IEEE Transactions on Industrial Electronics*, vol. 58, no. 8, pp. 3623–3633, 2011.

[102] W. Yao, Y. Yang, X. Zhang, F. Blaabjerg, and P. C. Loh, "Design and analysis of robust active damping for lcl filters using digital notch filters," *IEEE Transactions on Power Electronics*, vol. 32, no. 3, pp. 2360–2375, 2017.

[103] TI, *Tms320f2837xd dual-core microcontrollers*, https://www.ti.com/lit/ds/symlink/tms320f28379d, Web Page, access: 2020.

[104] PSIM, "Tutorial - electric machine modeling," Report, 2018.

[105] K. Duke, "Bipolar +/-10v analog output from a unipolar voltage output dac," Report, 2013.

[106] Y. Wu, Y. Wu, M. Rong, F. Yang, J. Zhong, M. Li, and Y. Hu, "A new thomson coil actuator: Principle and analysis," *IEEE Transactions on Components, Packaging and Manufacturing Technology*, vol. 5, no. 11, pp. 1644–1655, 2015.

[107] PI-Ceramic, "Material data," Report.

[108] R. Peña-Alzola, M. Liserre, F. Blaabjerg, R. Sebastián, J. Dannehl, and F. W. Fuchs, "Systematic design of the lead-lag network method for active damping in lcl-filter based three phase converters," *IEEE Transactions on Industrial Informatics*, vol. 10, no. 1, pp. 43–52, 2014.

[109] MATLAB, *Continuous-discrete conversion methods*, https://www.mathworks.com/help/control/ug/continuous-discrete-conversion-methods.html, Web Page, access: April 2021.